K^+ production in heavy ion collisions at 1.5 AGeV

Dem Fachbereich Physik

der Technischen Universität Darmstadt

zur Erlangung des Grades

eines Doktors des Naturwissenschaften

(Dr. rer. nat.)

vorgelegte Dissertation von

Anne Devismes

aus Toulon / Frankreich

Darmstadt 2000

D17

Referent: Prof. Dr. P. Braun-Munzinger

Koreferent: Prof. Dr. J. Wambach

Tag der Einreichung: 6. Dezember 2000

Tag der Prüfung: 5. Februar 2001

Summary

In this work the production of K^+ mesons in central heavy ion collisions is investigated as function of the system size at a beam energy of 1.5 AGeV. The systems used for this study are Ca+Ca, Ru+Ru and Au+Au. The aim is to learn more on the modification of hadron properties in nucelar medium due to an eventual restoration of the chiral symmetry. Indeed, theoretical calculations predict an increase of K^+ mass with nuclear density which would lead to a decrease of their production probability.
Data are compared to the predictions of the RBUU und IQDM models and seem to favor the version of the calculation including in-medium effects.

Zusammenfassung

In dieser Arbeit wird die Abhängigkeit der Produktion von K^+ Mesonen in zentralen Schwerionenstößen von der Systemgröße untersucht. Dafür wurden die Massensysteme Ca+Ca, Ru+Ru und Au+Au bei einer Strahlenergie von 1.5 AGeV verwendet. Das Ziel ist zu verstehen, wie siche die Hadroneneigenschaften in heißer und dichter Kernmaterie aufgrund der möglichen Restorierung der chiralen Symmetrie verändern. Theoretische Vorhersagen zeigen nämlich, daß die K^+ Masse mit der Dichte zunimmt. Das führt dazu, daß die K^+ Produktionswahrscheinlichkeit bei hohen Dichten kleiner werden muß.
Die experimentellen Ergebnisse wurden mit den Vorhersagen von RBUU und IQMD Modellen verglichen. Es scheint, daß die Rechnung, die eine in-Medium Modifikation von Hadronen berücksichtigt, die Daten besser reproduzieren kann.

Table of contents

Chapter 1

Introduction

The strangeness degree of freedom of strongly interacting nuclear matter is of high interest to nowadays nuclear physics. The reason is found in the relatively low mass of the strange quark, that allows strangeness production at small excitation energies. Since strangeness is conserved in strong interactions, strange particles carry at least partially the information on the conditions prevailing during their formation.
Especially at small available energies, strange particles probe sensitively the environment of their production. This feature was explored 20 years ago by Aichelin and Ko [Aic 85] who suggested that K^+ production can be used to investigate the nuclear equation of state (EOS). In the meanwhile, it was found that other phenomena influence strangeness production as well. Most probably, all hadrons change their properties once embedded in a medium due to the chiral symmetry of QCD (Quantum Chromo Dynamics).
To which extent kaons probe this fundamental symmetry or whether their dynamics is rather reflecting the resonance structure of hadrons is an active field of research.

Heavy ion collisions provide the only tool to address these interesting properties of strong interaction experimentally in a systematic way. Unfortunately, the systems accessible are very limited in size and in lifetime so that one has to be very cautious before concluding from experimental observables to basic properties of QCD.
Experimentally, the situation with respect to global conditions is already well established. It is summarized in Figure 1.1 which shows the temperature as a function of the baryon chemical potential, derived from abundances of all produced particles in central heavy ion collisions [Bra 98].

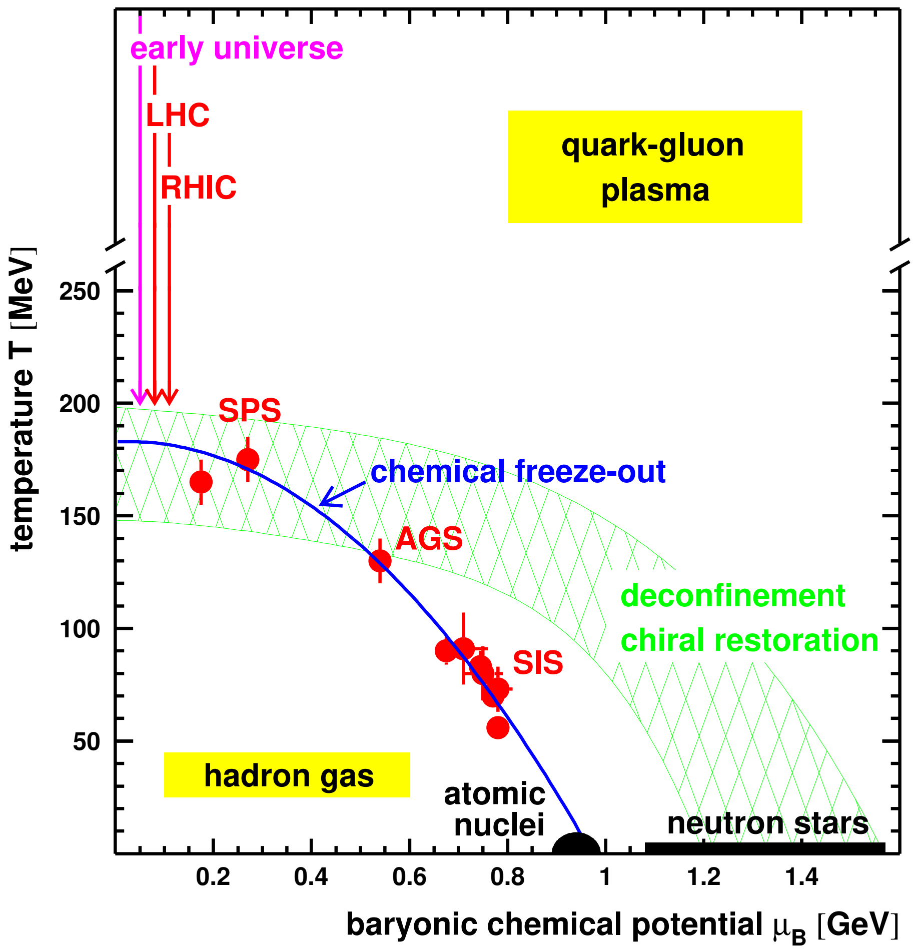

Figure 1.1: *Phase diagram of nuclear matter in terms of temperature as a function of the baryonic chemical potential.*

All available experimental data can be explained with an accuracy of about 30% by a thermodynamic equilibration model thus demonstrating over the whole incident energy range available today that the final state is close to thermal equilibrium. With reaction rates as obtained from free hadron-hadron cross sections, this is a very surprising observation, chemical equilibrium can not be obtained that way [Bra 00]. At high incident energies (higher than at SPS), the formation of a quark-gluon plasma (QGP) provides a natural explanation [Raf 82]. Within the QGP framework, strangeness production is enhanced and especially multistrange particles are produced with increasing probability.

This was experimentally observed by the WA97 collaboration. The measurement of hyperon yields (Λ, Ξ, Ω) in Pb+Pb collisions at SPS by the WA97 experiment shows a systematic increase with respect to p-A collisions [Ant 99]. This enhancement increases with strangeness content and can not be explained by hadronic models. This behavior has been predicted as a consequence of the QGP phase transition [Raf 91].
The situation at AGS is rather unclear. The measured freeze-out point is very close to the hypothetical phase boundary but QGP calculations at those net baryon densities are not yet available to allow for a quantitative interpretation.
At even lower energies, as the ones investigated in this work, the situation is even more unclear. There is certainly no QGP produced at SIS energies but, nevertheless, the system manages to freeze-out close to chemical equilibrium. This gives rise to the need of investigating modifications of strangeness production processes.
Interesting applications of the properties of strongly interacting matter are indicated in Figure 1.1. At very high temperatures and low baryon densities, a system is created with properties similar to the ones existing in the early universe. At high baryon densities and low temperatures, one probes matter similar to the one found in the interior of neutron stars (or at the maximum compression stage of a supernova of type II).

Chiral symmetry restoration and properties of hadrons in-medium

Chiral symmetry [Koc 97] is a symmetry of QCD in the limit of vanishing quark masses. If the chiral symmetry was realized, each particle would have a chiral partner and would appear with it in a doublet, which is not the case in nature. This is an indication that this symmetry is spontaneously broken.
The properties of hadrons, in particular of kaons, in nuclear matter provide information on the chiral symmetry. Indeed, several models predict that its restoration should lead to a modification of hadron properties. This scenario has already explained successfully the data on dileptons obtained at SPS by the CERES and HELIOS3 collaborations [Rap 00].

The QCD Lagrangian can be decomposed in two parts as follows:

$$L_{QCD} = L_0 + m\Psi\bar{\Psi} \tag{1.1}$$

For non-vanishing quark masses, the second term mixes right and left handed quarks and the chiral symmetry is explicitly broken. But the mass of the quarks u and d is very small (5 MeV/c^2) compared to the typical hadronic scale of 1 GeV/c^2 so this term can be treated as a small perturbation to the Lagrangian. This is also valid to some extent for the strange quark. But its higher mass (150 MeV/c^2) makes the approximation less reliable.

If one neglects the small perturbation due to the non-vanishing quark masses, the QCD Lagrangian is invariant under a transformation $SU(3)_L \otimes SU(3)_R$, but the ground state, which is the vacuum of QCD, does not show this symmetry. This means that the chiral symmetry is spontaneously broken. The Goldstone theorem tells us that a Goldstone mode appears each time a symmetry is spontaneously broken. This mode is characterized by massless Goldstone bosons. In the case of QCD with two flavors (up and down), the Goldstone bosons of the chiral symmetry are the pions. If strangeness is considered as well, kaons and eta's are the next Goldstone modes. Due to the explicit breaking of chiral symmetry, these Goldstone bosons are not massless. This is what is observed in nature.

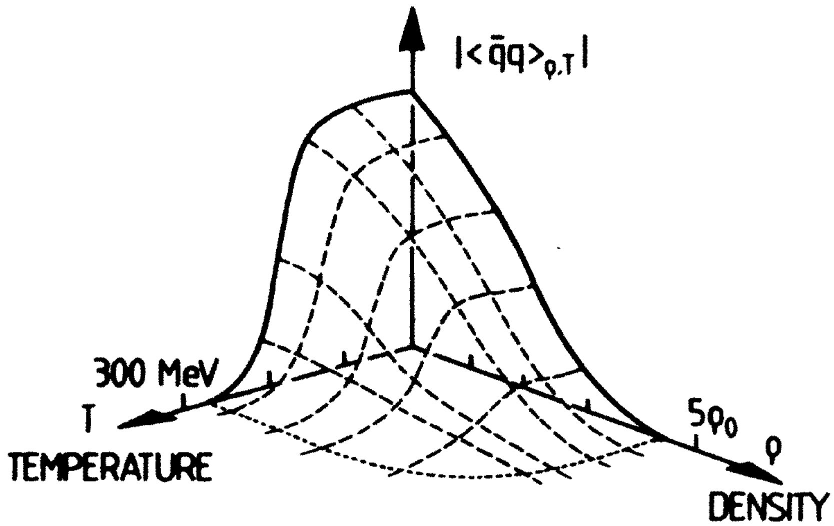

Figure 1.2: *Value of the quark condensate as a function of temperature and of density taken from [Kli 90].*

The quark condensate $< q\bar{q} >$ is an order parameter of the chiral symmetry and thus provides information on the degree of restoration of this symmetry. The value of this condensate characterizes the density of $q\bar{q}$ pairs in QCD vacuum. If the chiral symmetry was realized, the quark condensate should be equal to 0, which is not the case in QCD vacuum and at normal nuclear matter density. This reflects the fact that the chiral symmetry is broken [Wei 96, Kli 90, Lut 92].

At high temperatures and energies, a phase transition towards a restoration of chiral symmetry should be observed. This is illustrated in Figure 1.2 which shows in a qualitative way the evolution of the quark condensate as a function of the temperature and of the density. More recent calculations can be found for the evolution of the quark condensate as a function of the density for T=0 [Lut 00].
At normal nuclear matter density ρ_0, the $< q\bar{q} >$ is finite. Above few times ρ_0, the value of the quark condensate is vanishing and the symmetry should be restored. It is interesting to note that already at the normal nuclear density ρ_0, the quark condensate has a reduced value which corresponds to a 35% restored symmetry.

The restoration of chiral symmetry may modify the properties of hadrons produced in nuclear matter and especially lead to the dropping mass scenario [Ko 96]. In this approach, the hadron masses depend on the density of the fireball in which they are produced.
In the mean-field approximation to the effective $SU(3)_L \otimes SU(3)_R$ Lagrangian, a dispersion relation for kaons in a nuclear medium can be written as:

$$\omega^2_{K\pm}(k,\rho_B) = m^2_K + k^2 - \frac{\Sigma_{KN}}{f^2}\rho_S \pm \frac{3}{4}\frac{\omega}{f^2}\rho_B \tag{1.2}$$

where m_K and k are the kaon bare mass and its momentum, respectively. The additional terms include a scalar interaction (third term) and a vector interaction (fourth term) of the kaon with its surrounding medium. Their strength is fixed by the so-called kaon-nucleon sigma term Σ_{KN}, the scalar density ρ_S, the kaon decay constant f and the nuclear density ρ_B. The scalar interaction is attractive for kaons and anti-kaons whereas the vector interaction is attractive for anti-kaons and repulsive for kaons. From equation 1.2 one can write the energy of the kaons as follows:

$$\omega_{K^\pm}(k,\rho_B) = \sqrt{m^2_K + k^2 - \frac{\Sigma_{KN}}{f^2}\rho_S + (\frac{3}{8}\frac{\Sigma_{KN}}{f^2})^2} \pm \frac{3}{8}\frac{\rho_B}{f^2} \tag{1.3}$$

The effective mass $m^*_{K^\pm}$ of a kaon at rest is given by:

$$m^*_{K^\pm} = \omega_{K^\pm}(0, \rho_B) \tag{1.4}$$

and the kaon-nucleon potential U by:

$$U_{K^\pm}(k, \rho_B) = \omega_{K^\pm}(k, \rho_B) - \sqrt{m_K^2 + k^2} \tag{1.5}$$

Several models predict the dependence of the kaon effective mass on the density [Sch 97, Mao 99]. Some examples are depicted in Figure 1.3 which shows the K$^+$ and K$^-$ effective masses as a function of the density normalized to the normal nuclear density. The different lines are obtained for different set of parameters in the calculations as explained in [Sch 97] and [Mao 99]. Due to the different sign of the vector potential for kaons and anti-kaons, the dependence of their mass on the density is not the same. The K$^+$ mass slightly increases whereas the K$^-$ mass is reduced. This should lead to an enhanced K$^-$ yield (their production becoming energetically easier) and to a reduction of the K$^+$ yield (their production becoming energetically more difficult).

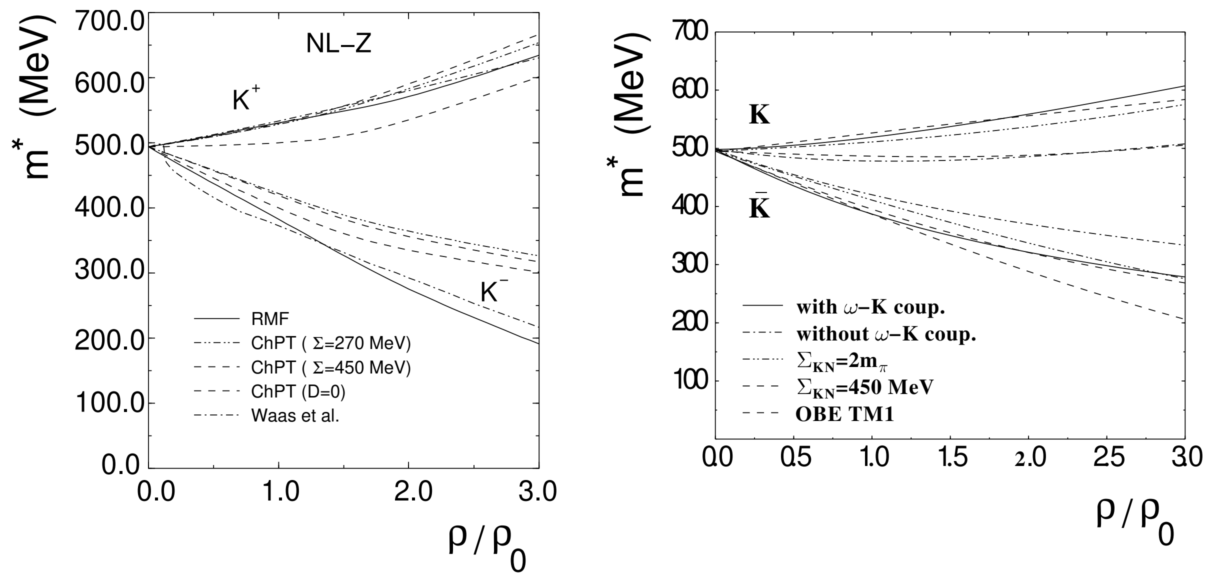

Figure 1.3: *K^+ and K^- effective mass as a function of the nuclear density normalized to the normal nuclear density taken from [Sch 97] (left panel) and [Mao 99] (right panel).*

The propagation of kaons is also influenced by the medium in which they are produced. This can be observed experimentally by investigating their phase space distribution and their flow. Since K^+ mesons feel a repulsive potential, they are pushed away from nucleons whereas K^- are attracted towards nucleons due to the attractive potential.

The study of kaon properties in hot and dense nuclear matter appears as a promising tool for the investigation of chiral symmetry restoration and its consequences on hadron properties in medium.

Neutron stars

It is still an open question why the mass of neutron stars never exceeds 1.5 solar masses. One of the most popular scenario to explain this observation is the following [Bro 94]: if the mass of K^- mesons decreases when increasing the density, for a density sufficiently high, the total K^- energy becomes smaller than the electrochemical potential. This leads to a kaon condensation which would enhance the proton to neutron ratio and thus softens the EOS. The consequence is that low-mass black holes are more likely to form than neutron stars with a mass larger than 1.5 solar masses.
Investigating kaon properties in-medium seems to be a promising way to understand the properties of neutron stars.

Heavy ion collisions at SIS energies

The SIS-energy regime is particularly well suited for the study of kaon production and the investigation of in-medium effects for several reasons.

- A change in the kaon mass translates into a change in the energy threshold for kaon production. In direct nucleon-nucleon collisions the threshold energy for K^+ production via the reaction $NN \rightarrow K^+\Lambda N$ is 1.58 GeV and 2.5 GeV for K^- production via the reaction $NN \rightarrow K^+K^-NN$. In the SIS-energy domain, kaons are produced close or even subthreshold, where the in-medium effects should be most pronounced.

- Figure 1.4 shows the evolution of the density as a function of the time for a Au+Au collision at different beam energies [Fri 98]. The high density phase at SIS energies (2 AGeV) is quite long compared to the higher energies. However, these predictions have to be taken with caution. The estimate of the density reached in the fireball are not an easy task and the values presented here may be questionable.

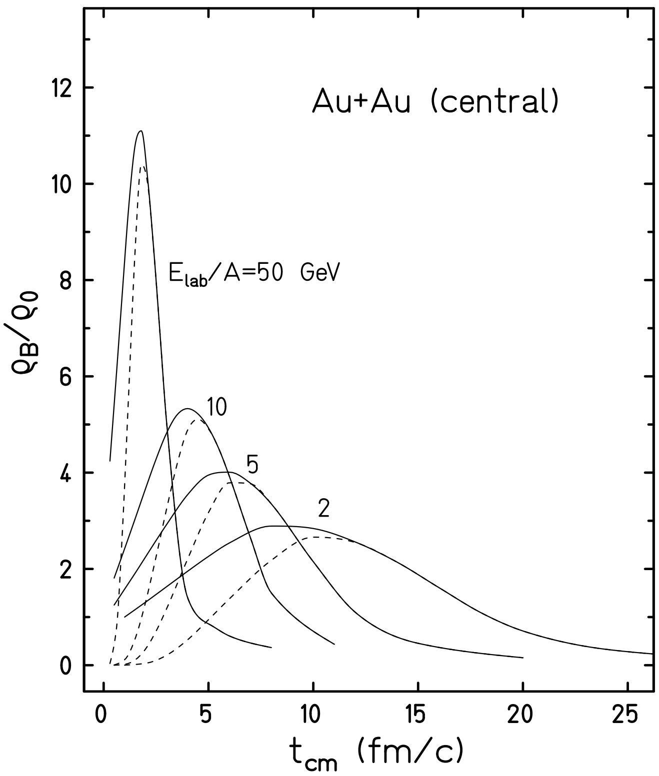

Figure 1.4: *Baryonic density normalized to the saturation density ρ_0 achieved in a Au+Au collision as a function of the time for different beam energies taken from [Fri 98]. The solid lines correspond to all baryons while the dashed lines are for the participants only.*

Characteristics of heavy ion collisions

The properties of the fireball can not be measured directly. This information has to be deduced from the measurement of particle production probability and of their phase space distributions. It is thus mandatory to understand as well as possible the dynamics of the collisions, in order to be able to extract the static properties of nuclear matter. In this respect, the theoretical models play a major role. They allow to describe the evolution of a collision and to characterize several observables relevant for the investigation of the fireball properties.

Figure 1.5 shows the collision of two Au nucleus at 2 AGeV simulated with the IQMD (Isospin Quantum Molecular Dynamics) model [Har 92].

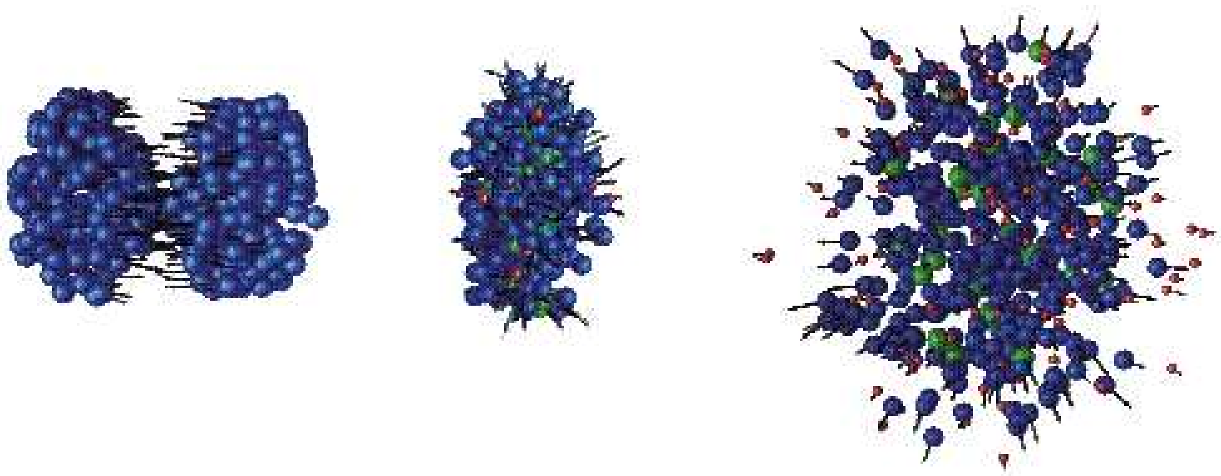

Figure 1.5: *IQMD simulation of a Au+Au collision at 2 AGeV.*

The first phase of the collision corresponds to the interpenetration of the two nucleus which form a hot and dense fireball. At SIS energies, the maximum density ($3\rho_0$) is reached after about 10 fm/c. In the second phase, the system starts to expand until the particles do not interact strongly anymore. At this point, called the freeze-out, the particles decouple from each other.

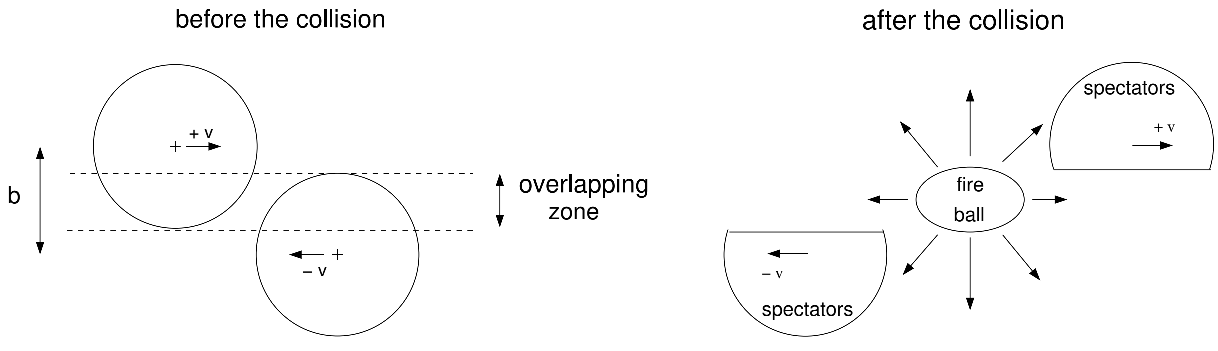

Figure 1.6: *Definition of the impact parameter and of the fireball.*

The observations deduced from the measurement of particles in the detector depend on the size of the colliding nucleus, on the beam energy and on the impact parameter, which is the distance between the center of the two nucleus as depicted in Figure 1.6.

This quantity characterizes the centrality of the collision. Ideally, only the nucleons in the overlapping zone, called fireball, participate to the collision. The other nucleons are called spectators.

K^+ measurement with the FOPI detector

The FOPI collaboration has already successfully measured kaons and anti-kaons in Ru+Ru at 1.69 AGeV and Ni+Ni at 1.93 AGeV. Results on K^+ differential flow [Cro 00] and K^-/K^+ ratio dependence on rapidity and transverse momentum [Wis 00] were obtained for these two systems. When compared to the predictions of the RBUU model [Cas 90], the data seem to favor the version of the calculation including kaon mass modification. Since the kaon production depends on the density reached in the fireball, it is interesting to measure the kaon production cross section as a function of the centrality, which is related to the density. For that purpose, one can study the kaon production as a function of the number of participants in a given system at a given energy. It is also meaningful to investigate kaon production as a function of the system size.

The KaoS collaboration has measured the number of kaons per participant as a function of the number of participating nucleons (A_{part}) in Ni+Ni and Au+Au collisions at 1 AGeV. The results are summarized in Figure 1.7.

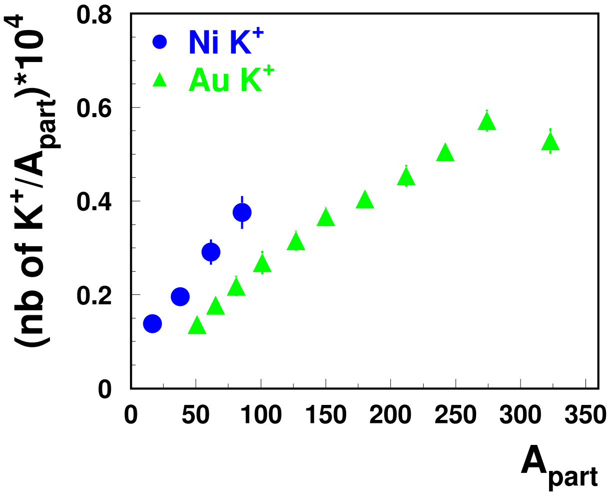

Figure 1.7: *Number of K^+ per A_{part} as a function of A_{part} for Ni+Ni (dots) taken from [Bar 97] and Au+Au (triangles) taken from [Man 97] collisions at 1 AGeV.*

The number of kaons per A_{part} increases with A_{part} in both systems. However, it seems to increase faster in light systems than in heavy systems which is a hint for system size effects.

The FOPI collaboration has recently measured Ca+Ca and Au+Au collisions at 1.49 AGeV. This measurement allows to investigate the kaon production as a function of the system size at high energy. Ru+Ru collisions at 1.52 AGeV were previously measured and these data are analysed as well. The kaon production in this system is also compared to the kaon production in Ru+Ru collisions at 1.69 GeV.
The aim is to learn more about the system size dependence of kaon production and also on kaon properties in-medium. Indeed, the production of kaons is influenced by the potential they feel in nuclear matter as explained above. Measuring production cross sections provides a valuable tool for the investigation of in-medium properties of kaons which are strongly connected to the restoration of chiral symmetry.

This work is organized as follows: the FOPI detector and the kaon identification strategy are presented in chapter 2. The method and the results concerning the tracking efficiency are summarized in chapter 3. Chapter 4 contains the physics results. Rapidity distributions for protons in Ca+Ca at 1.49 AGeV, Ru+Ru at 1.52 AGeV and 1.69 AGeV and Au+Au at 1.49 AGeV and for kaons in Ru+Ru collisions at the two energies available are presented. The number of kaons as a function of the system size is investigated for 1.5 AGeV beam energy. Those results are compared to the predictions of transport model calculations (IQMD and RBUU) in chapter 5. To improve the quality of the measurements, the FOPI collaboration has decided in 1997 to upgrade its detector. The main part of this upgrade consists in the construction of a new time of flight system, composed of PesToF spark counters. A two year R & D program was initiated and the results of these investigations are presented in chapter 6. Chapter 7 contains a summary and an outlook.

Chapter 2

FOPI detector and charged particle identification

2.1 The FOPI detector

In this section the main components of the FOPI detector are presented. For a detailed description of the apparatus see [Gob 93, Rit2 95].

The FOPI detector (Figure 2.1) installed at SIS/GSI (Darmstadt) belongs to the 4π generation of multidetectors. It allows to identify event by event light charged particles and intermediate mass fragments. Neutral hadrons can also be reconstructed from their decay into two charged particles. The large phase space coverage and the azimuthal symmetry of the detector allows for an almost complete characterization of the event.

The phase I of the detector is operational since 1991. Its main components are a wall of plastic scintillators (PLAWA) providing a charge identification of particles emitted in the angular range between 7° and 30° and a zero degree detector which covers the angular range between 1.5° and 7°.

The phase II of the FOPI detector was completed in 1994. It is designed for experiments at the highest energies delivered by the SIS accelerator. Only very light fragments survive in such collisions and the production of mesons becomes important. The central part of the detector, which has to be able to identify up to 100 charged particles in one event, is equipped with a drift chamber (CDC) and a barrel of plastic scintillators. A superconducting magnet providing a magnetic field of 0.6 T is surrounding the CDC and the BARREL. A second drift chamber (HELITRON) provides the identification of particles at the forward angles. Both drift chambers allow for a mass identification of particles.

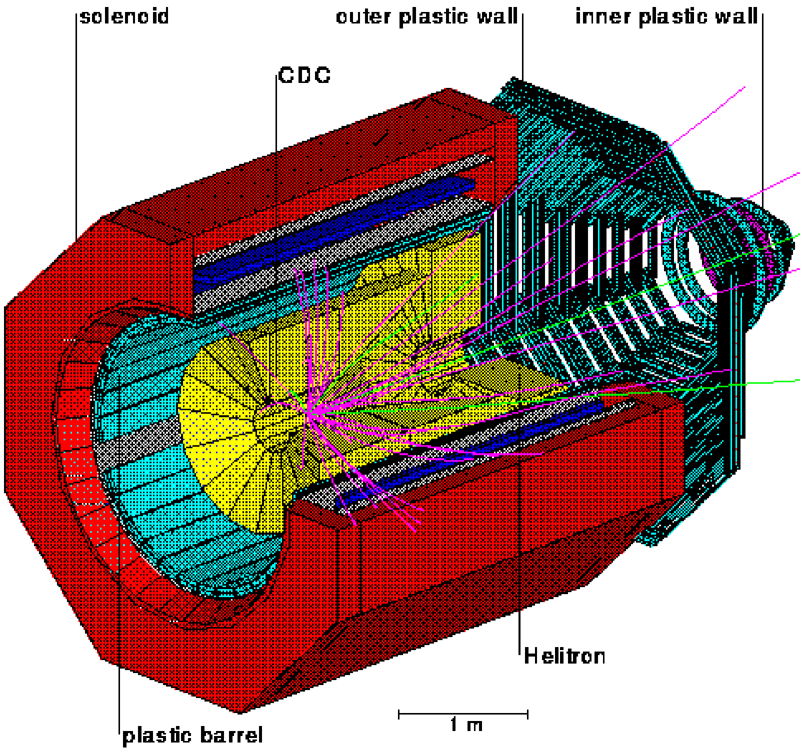

Figure 2.1: *View of the FOPI detector.*

CDC

The CDC has with an outer radius of 80 cm and a length of 2 m and covers the polar angular range between 33° and 150° in the laboratory reference frame. The chamber is divided into 16 sectors, each of them composed of 60 sense wires and 61 potential wires running parallel to the beam axis. The chamber works at atmospheric pressure with a mixture of 88% of Argon, 10% of Isobutane and 2% of Methane.

A particle crossing the gas volume deposits energy by ionization. The electrons drift towards the wires where the signals are collected at both ends.

Figure 2.2 shows the projection in the transverse plane of a Ru+Ru event at 1.69 AGeV. Each point corresponds to a hit produced by a charged particle. A tracking algorithm performs the track reconstruction by fitting the measured hits with a circle in the xy-plane and with a straight line in the z-direction. Then, a matching algorithm tries to associate each track measured in the CDC to a hit in the BARREL as will be described in section 2.2.3. Because of the magnetic field, the trajectories of charged particles are curved and the momenta are deduced from the track curvature. The simultaneous measurement of the energy loss allows for a mass identification using the Bethe-Bloch formula.

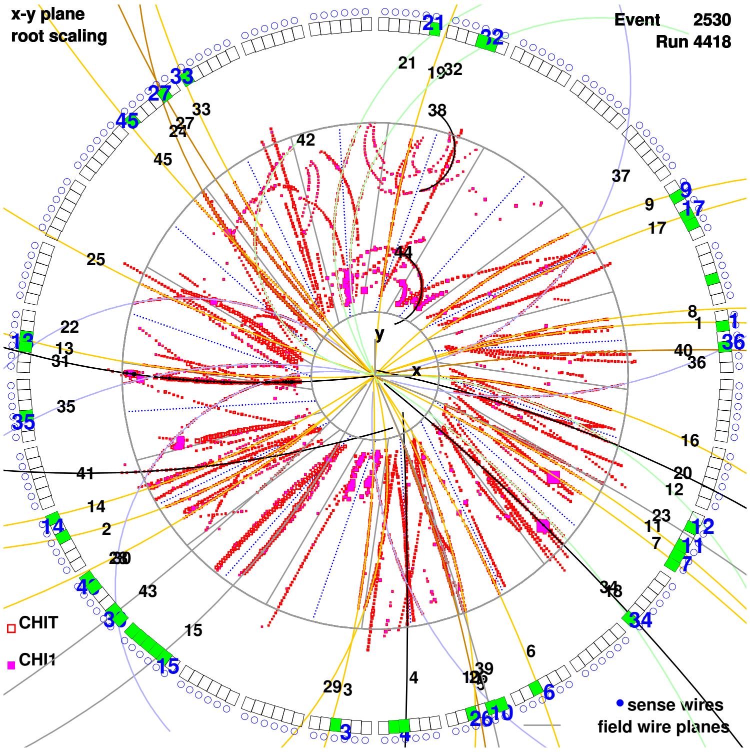

Figure 2.2: *Projection of a Ru+Ru at 1.69 AGeV event in the transverse plane. The thin circles correspond to the inner and outer radius of the CDC. The BARREL surrounding the CDC is represented by the squares and the outer most circle shows Cerenkov detectors (not used in this analysis). Each point corresponds to a hit produced by a charged particle on the wire. The tracks reconstructed by the tracking algorithm are marked by solid curves and are ordered from 1 to tmul, where tmul is the track multiplicity in the event. Positively (resp. negatively) charged particles are curved to the right (resp., left).*

The position resolution in the transverse plane is around 200 μm and the longitudinal resolution, given by the charge division on the wires, is of the order of 10 cm for minimum ionizing particles (MIP). The resolution for the specific ionization is 20 - 30 %.

To distinguish between a track and its mirror track, the sectors of the CDC are tilted by 8° with respect to the target as shown in Figure 2.3. For each hit measured on the sense wires, electrons can *a priori* originate from both sides of the wire plane. Both tracks are extrapolated to the target and the minimal distance to the primary vertex is calculated in the transverse plane (d_0) and in the longitudinal direction (z_0). Due to the inclination of the sectors, only the real tracks point back to the target. The criterium to select the real track is $\mid d_0 \mid < 0.5$ cm and $\mid z_0 \mid < 15$ cm. In addition, due to the Lorentz angle, the most outer hits would correspond to an ionization happening outside the CDC for the mirror track. Furthermore, the sense wires of the CDC are staggered by 200 μm. This provides a second criterium to disentangle the real track and the mirror track as is explained in more details below for the HELITRON.

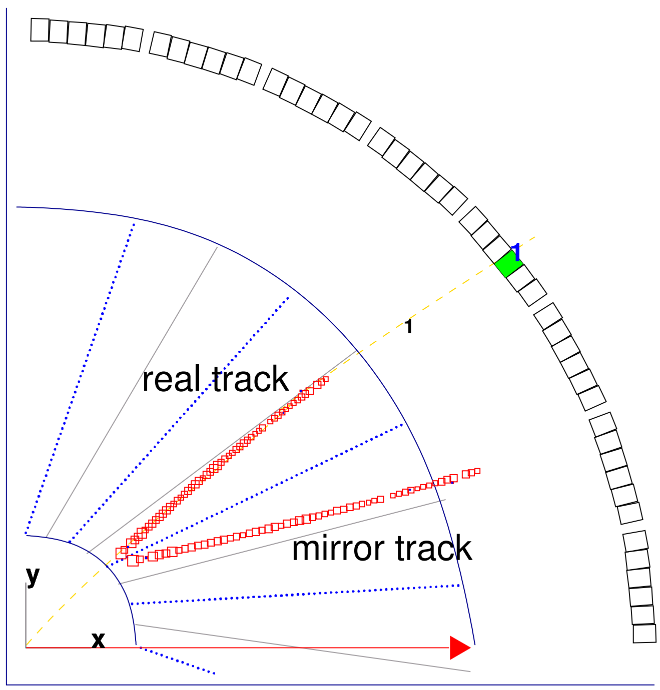

Figure 2.3: *Section of the xy-plane in the CDC showing the tilted sectors and an example of a track with its mirror track.*

BARREL

The barrel of plastic scintillators surrounding the CDC is composed of 180 slats running parallel to the beam axis that are readout at both ends by photo-multiplier tubes. The BARREL covers the angular range between 40° and 130° in the laboratory reference frame. The time response of this time of flight system is well described by a gaussian function with a resolution σ of 300 ps. Together with the information provided by the CDC, the time of flight measurement allows to improve the particle identification as explained in section 2.2.

HELITRON

The particles emitted in the forward hemisphere ($7° < \Theta_{\rm lab} < 30°$) are identified in the second drift chamber, the HELITRON. This chamber is divided into 24 sectors, composed of 54 sense wires and 53 potential wires perpendicular to the beam axis.
The particle identification is realized in the same way as in the CDC by the measurement of the energy loss and of the momentum (deduced from the curvature of the track). At the position of the HELITRON, the magnetic field is not homogeneous anymore. It has been measured and is known with an accuracy of 0.5 %. This allows to take into account the necessary corrections when data are analysed.

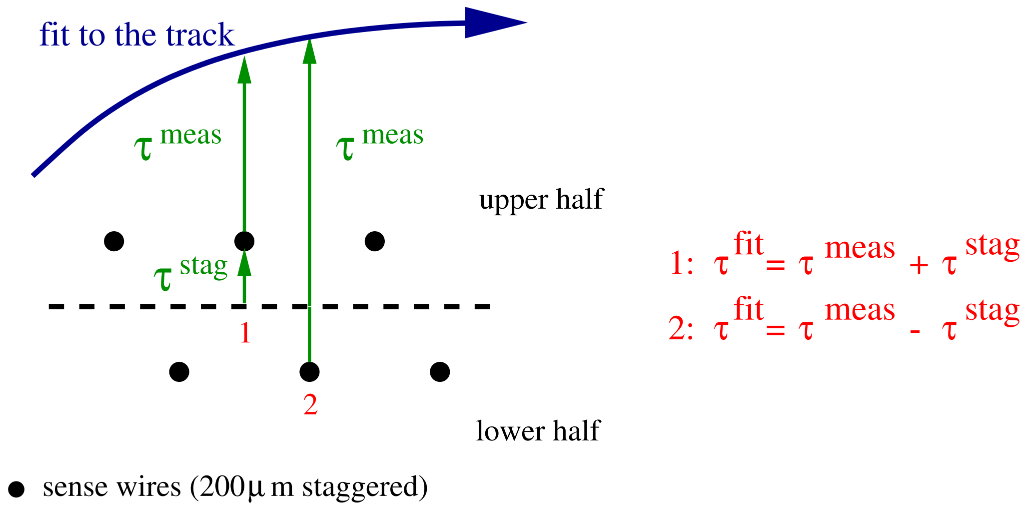

Figure 2.4: *Staggered sense wires in the HELITRON.*

The sense wires are staggered by 200 μm on each side of the wire planes. This allows to distinguish between a track and its mirror track. A polynomial function is fitted to the data in the drift time coordinate. The sign of the difference between the measured drift time and the time extracted from the fit for each hit tells on which side of the sector the particle was crossing the HELITRON as explained in Figure 2.4. This time difference can be related to the difference between the position of the measured track and the fitted track. This quantity, called staggering, provides some information on the quality of the reconstructed tracks: for good tracks, the extracted value for the staggering has to be close to the nominal value of 200 μm.

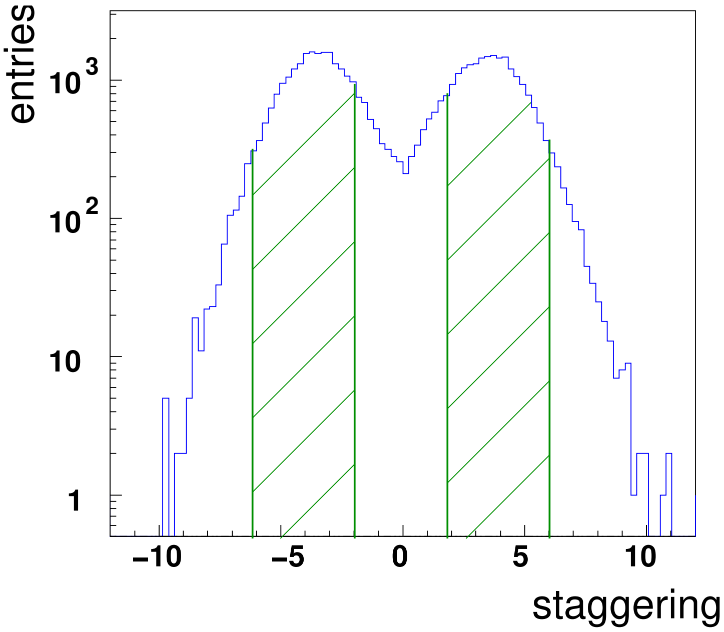

Figure 2.5: *Staggering distribution*

The staggering distribution (depicted in Figure 2.5 in arbitrary units) shows two peaks which are spread around the nominal value due to the detector resolution. The good tracks are selected by cutting out the tails of the two peaks and selecting the dashed areas as shown in Figure 2.5. However, the rejection of mirror tracks in the HELITRON is not as good as in the CDC, since the staggering of the wires is the only criterium. Furthermore, the particle trajectories in the forward hemisphere are almost straight lines due to the configuration of the detector. The determination of the curvature is thus more difficult and the extrapolation to the primary vertex is less reliable.

PLAWA

The forward time of flight system (PLAWA) is composed of 512 plastic scintillators grouped into 8 sectors of 64 modules which are readout by photo-tubes on both sides. It provides the measurement of the particle velocities between 7° and 30° in the laboratory reference frame. The time difference between the two photo-tubes gives the position of the hit on the slat. The time response of the PLAWA is also well described by a gaussian function with a resolution σ varying between 80 and 120 ps which translates into 1.2 - 2 cm position resolution. In this analysis, this sub-detector is used to provide a centrality selection by measuring the charged particle multiplicity in the forward part of the FOPI detector. It also allows to improve the particle identification realized in the HELITRON as described in section 2.3.

2.2 Charged particle identification in the central part

The main results of this work were obtained by analysing the data measured in the central part of the FOPI detector. In this section the kaon identification in the CDC/BARREL subsystem is described as well as the efficiency corrections and the background determination.

2.2.1 Event selection

The selection of the events is based on the one hand on the information delivered by the start counter which provides a time and an energy signal and on the other hand on the vertex reconstructed from the tracks measured in the CDC.

The selection of good vertices allows to reduce the contribution of events originating from the interaction of the beam with the material upstream to the target. Figure 2.6 shows the x- and y-coordinate distributions in Ru+Ru collisions at 1.52 AGeV for four centrality bins (the centrality selection is done by cutting on the charged particle multiplicity in the PLAWA as explained in the next section). For very central collisions, the number of particles is higher. This makes the reconstruction of the vertex easier. For this reason, the vertex distributions become narrower for the most central collisions (e.g.

for the largest track multiplicity). For all multiplicities, the selection of good vertices is realized with $| v_x |< 0.5$ cm and $| v_y |< 0.5$. The z-coordinate is fixed to 0.

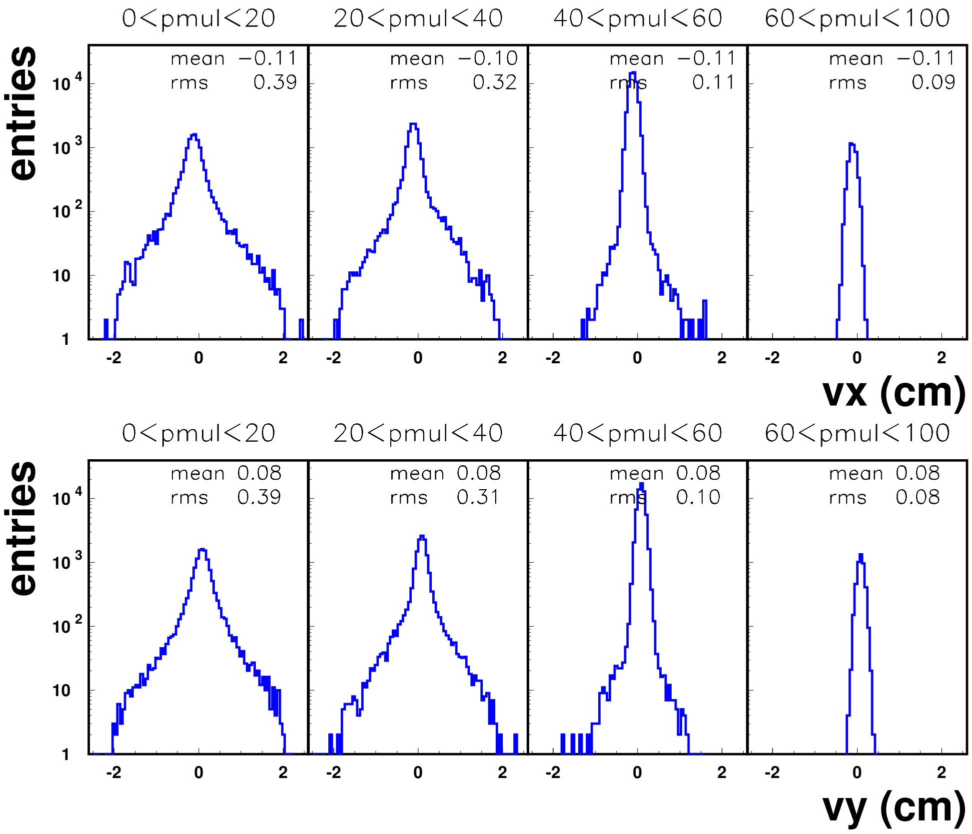

Figure 2.6: *Distributions for the x- and y-coordinates of the primary vertex in Ru+Ru collisions at 1.52 AGeV for four centrality bins.*

2.2.2 Centrality selection

The centrality of events is determined by the measurement of the charged particle multiplicity in the PLAWA, shown in Figure 2.7 for the minimum-bias (full histograms) and the central (dashed histograms) triggers in Ca+Ca and Au+Au collisions at 1.49 AGeV and in Ru+Ru collisions at 1.52 and 1.69 AGeV .

The most central events correspond to high multiplicities in the forward plastic wall. Part of the events may originate from the interaction of the beam with the surrounding material and gas. These background events contaminate the sample of good events especially in the region of low multiplicities. According to [Kut 00], this contamination is less than 1% for multiplicities higher than 50 in Ru+Ru collisions at 1.69 AGeV, which correspond to central collisions. Since only central events are selected for kaon identification as explained in section 4.1, the background events do not affect the analysis presented in the following.

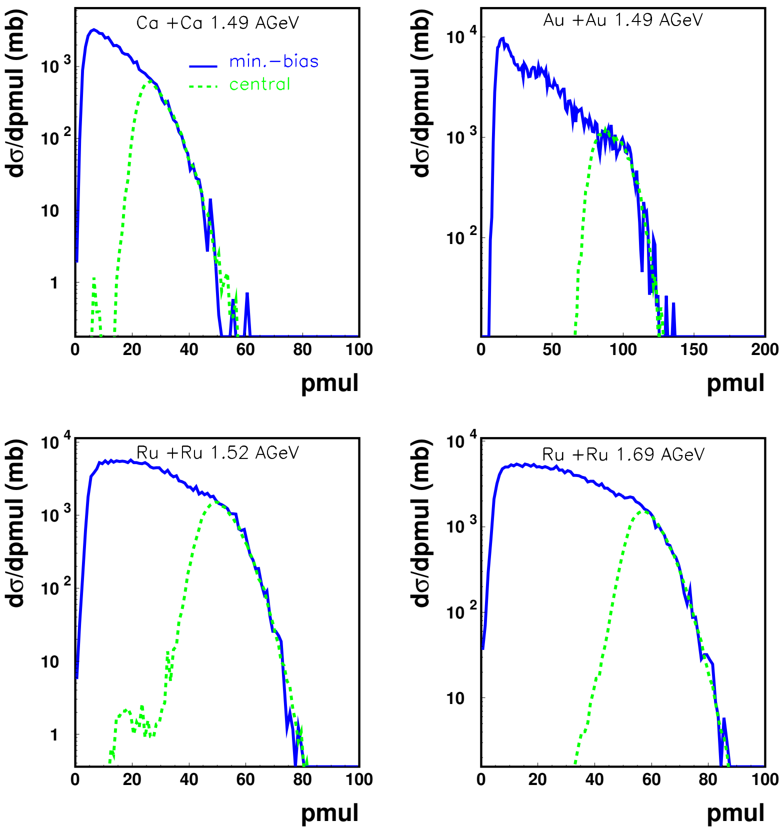

Figure 2.7: *Charged particle multiplicity in the PLAWA for Ca+Ca at 1.49 AGeV, Au+Au at 1.49 AGeV, Ru+Ru at 1.52 AgeV and 1.69 AgeV. The full (dashed) histograms correspond the the minimum-bias (central) trigger.*

2.2.3 K^+ identification

The system Ru+Ru at 1.52 AGeV is used in this section to illustrate the method for kaon identification. The same method is used for the other systems with some small differences in the cuts to optimize the quality of the identification.

The CDC alone allows to identify charged particles by means of the Bethe-Bloch relation between the energy loss in the gas volume of the chamber and the momentum, deduced from the curvature of the track in the magnetic field. The performance of the CDC is

good enough to identify pions, protons, deuterons and heavier particles. However the resolution does not allow to identify rare particles, e.g kaons, in a clean way. For that purpose, the information of the time of flight system is needed. Since the flight distance can be calculated from the measurement of the momentum and of the azimuthal and polar angles in the CDC, the time of flight measurement is equivalent to a velocity measurement and using the relation $p = m\gamma\beta$, a second mass identification is obtained. The redundancy of the mass measurement improves the kaon identification. The drawback of using the BARREL is that the acceptance is reduced since this sub-detector covers only the polar angular range between 40° and 130°.
The procedure to combine the information delivered by the CDC and the BARREL is the following: when possible, each track in the CDC is associated to a hit in the BARREL in a given window in the azimuthal angle $\mathrm{d}\phi = \phi_{\mathrm{BAR}} - \phi_{\mathrm{CDC}}$ and in the longitudinal direction $\mathrm{dz} = \mathrm{z_{BAR}} - \mathrm{z_{CDC}}$. The values for ϕ_{CDC} and $\mathrm{z_{CDC}}$ are obtained by extrapolating the track measured in the CDC to the time of flight system and estimating its coordinates at the extrapolated intersection with the BARREL. The distributions of dz and dϕ as well as the correlation between these two observables are represented in Figure 2.8.

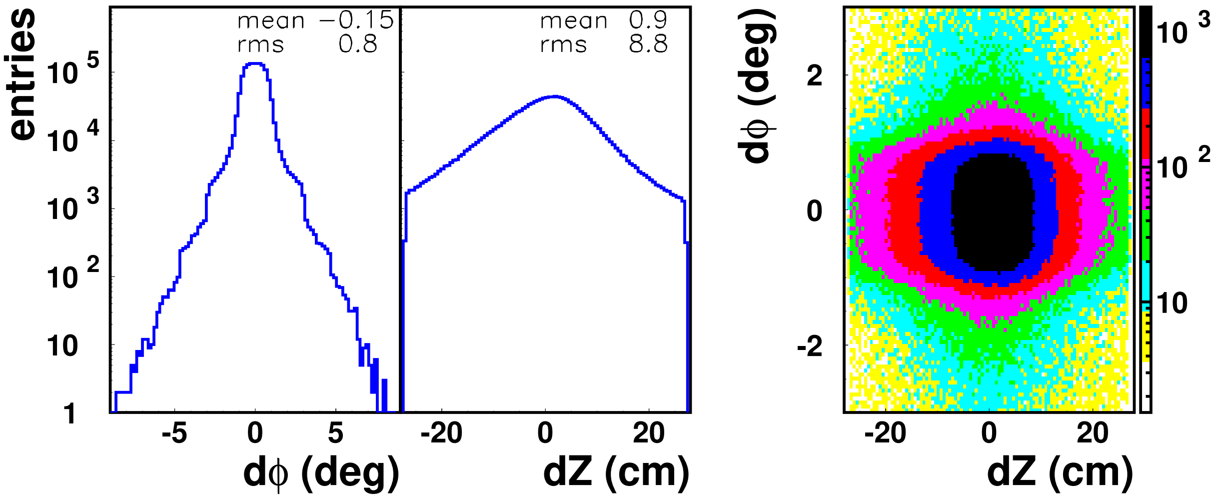

Figure 2.8: *Matching observables for Ru+Ru collisions at 1.52 AGeV: matching window in the transverse plane dϕ and matching window in the z-direction dz (left panel) and dϕ as a function of dz (right panel).*

The quality of the matching is defined by the following parameter:

$$\chi^2 = \left(\frac{\mathrm{dz}}{\sigma_\mathrm{z}}\right)^2 + \left(\frac{\mathrm{d}\phi}{\sigma_\phi}\right)^2 \tag{2.1}$$

where σ_z and σ_ϕ are the width of the distributions plotted in Figure 2.8 and are equal to 8.8 cm and 0.8°, respectively.

The mass distributions for different cuts on this quantity are plotted in Figure 2.9 for Ru+Ru collisions at 1.52 AGeV, the mass being defined below. A momentum cut of p < 0.5 GeV/c has been applied. Three cases are presented: no cut on χ^2 (dashed histogram), $\chi^2 < 5$ (full histogram) and $\chi^2 < 1$ (dotted-dashed histogram). The separation between pions, kaons and protons is improved when applying a cut on χ^2. However, a too strong cut reduces significantly the signal, not only for kaons but also for protons and pions. A compromise has to be done between the quality of the kaon peak in the mass distribution and the magnitude of the signal. The value chosen for the analysis is $\chi^2 < 5$; it allows for a reduction of the background between the pion, kaon and proton peaks in the mass distribution without losing too much signal.

The correlation between the energy loss and the momentum measured in the CDC provides a first identification of charged particles. The mass determined with these observables is called CDC-mass (cm). A second mass identification can be obtained by correlating the momentum measured in the CDC and the velocity measured in the BARREL. This mass is called BARREL-mass (bm). These two correlations are depicted in Figure 2.10 for Ru+Ru collisions at 1.52 AGeV. The lines correspond to the expected values for each particle specie, deduced from the Bethe-Bloch formula. In both cases, the kaon branch appears in a clear way. With this representation, it also becomes clear that an identification of kaons above a momentum of 0.5 GeV/c is very difficult because of the contamination from pions and protons. In Au+Au collisions, kaon identification is possible only up to p=0.4 GeV/c.

After selecting the good matched tracks and the low momenta, the final kaon selection is realized by a two-dimensional cut on the correlation between cm and bm as shown in Figure 2.11 by the dark curve which corresponds to the following ellipse:

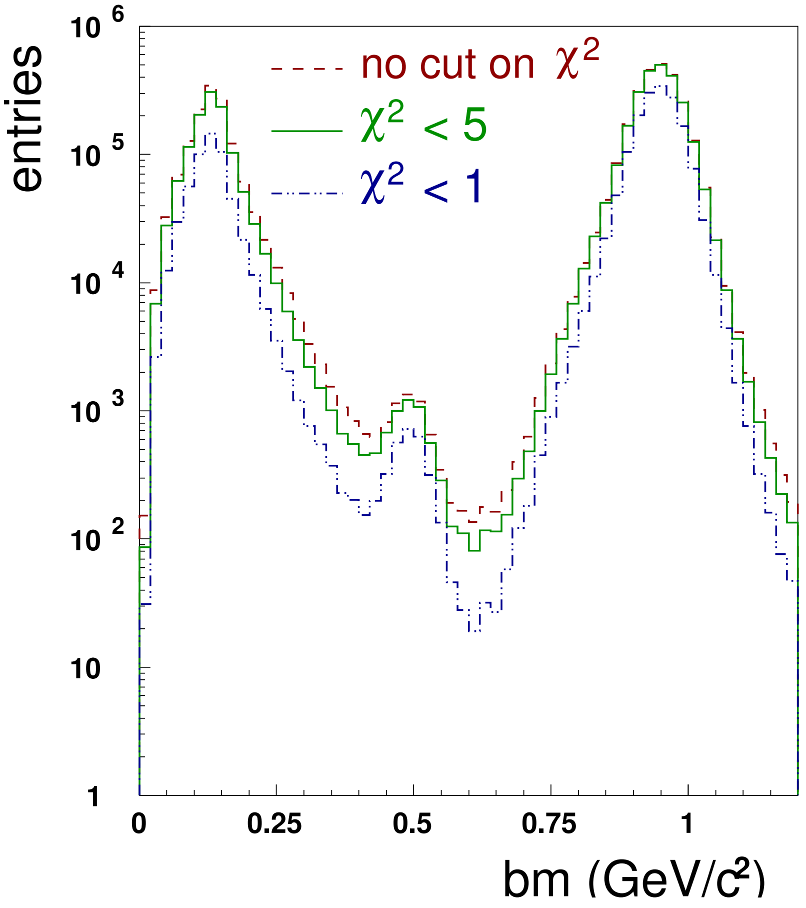

Figure 2.9: *Mass distribution in Ru+Ru at 1.52 AGeV for different cuts on* χ^2 *(dotted-dashed histogram:* $\chi^2 < 1$*, full histogram:* $\chi^2 < 5$ *and dashed histogram: no cut on* χ^2*). A momentum cut of* $p < 0.5$ *GeV/c has been applied in each case.*

$$\sqrt{\left(\frac{\mathrm{bm}-\mathrm{m_K}}{\sigma_{\mathrm{bm}}}\right)^2+\left(\frac{\mathrm{cm}-\mathrm{m_K}}{\sigma_{\mathrm{cm}}}\right)^2}$$

where $\mathrm{m_K}$ is the kaon nominal mass and σ_{bm} and σ_{cm} are the resolution of bm and of cm, respectively, the first one being 50 MeV/c^2 and the second one being 90 MeV/c^2.

In what follows, the mass distributions correspond to the BARREL mass bm, defined by the correlation between the momentum measured in the CDC and the velocity measured in the BARREL. Using the strategy described above allows to identify kaons in all the systems under investigation. The mass distributions showing the kaon peaks are presented in Figure 2.12 with an upper momentum cut of 0.5 GeV/c for Ca+Ca

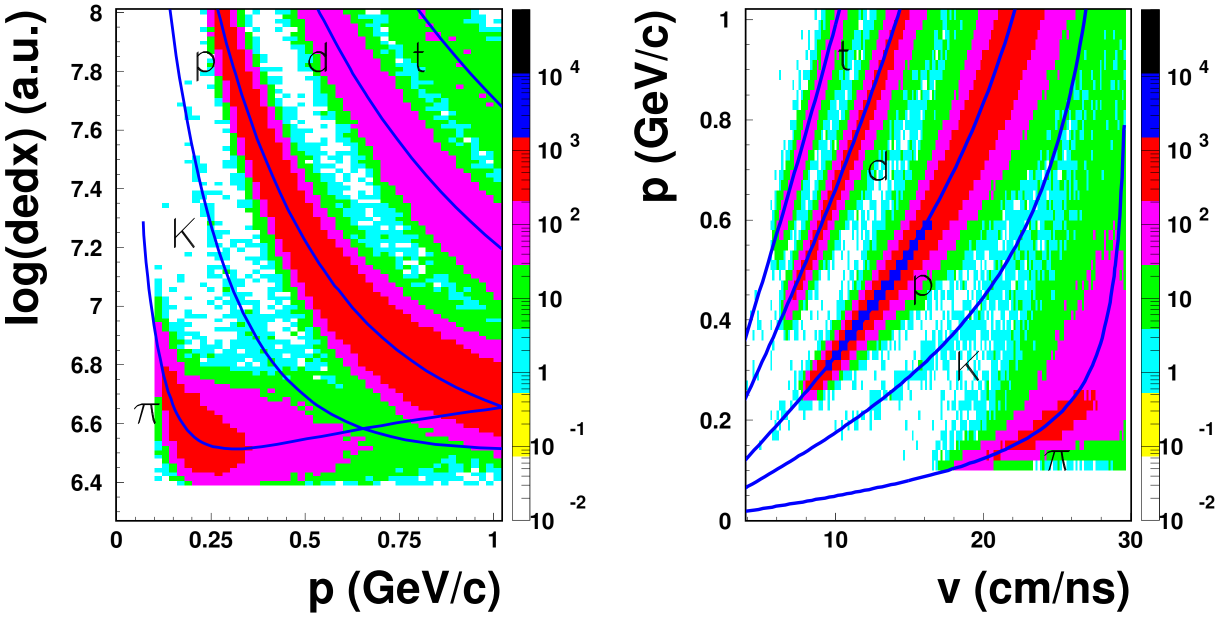

Figure 2.10: *Two dimensional identification of kaons in Ru+Ru collisions at 1.52 AGeV with* $\chi^2 < 5$*: energy loss as a function of the momentum (left panel), momentum as a function of the velocity (right panel). The lines correspond to the expected values for each particle specie using the Bethe-Bloch formula (left panel) and* $p = m\gamma\beta$ *(right panel).*

at 1.49 AGeV, Ru+Ru at 1.52 and 1.69 AGeV and of 0.4 GeV/c for Au+Au at 1.49 AGeV.

The number of identified kaons in the CDC/BARREL acceptance for the most central reactions is summarized in Table 2.2 for each system. These numbers are obtained with the cuts described above.

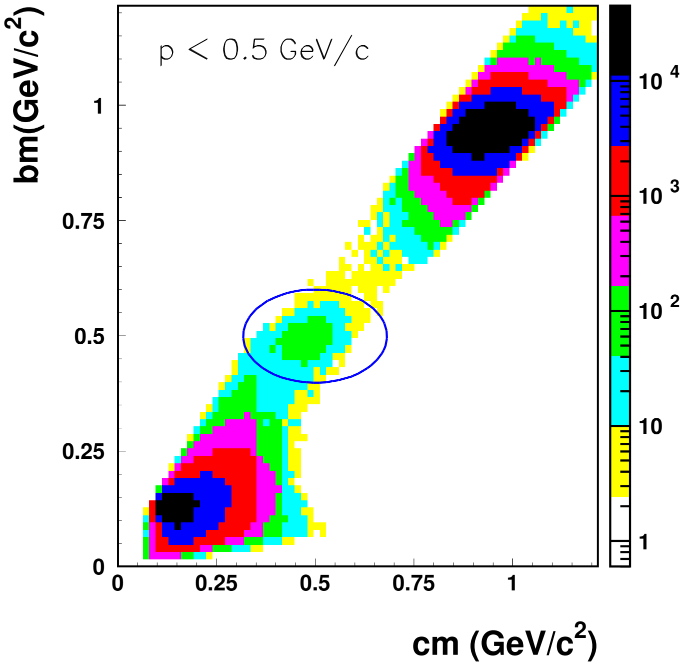

Figure 2.11: *BARREL-mass versus CDC-mass in Ru+Ru collisions at 1.52 AGeV. The curve describes the ellipsoidal cut mentioned in the text.*

	Ca 1.49 AGeV	Au 1.49 AGeV	Ru 1.52 AGeV	Ru 1.69 AGeV
nb of events	$6.9 \cdot 10^3$	$3.6 \cdot 10^5$	$1.5 \cdot 10^6$	$3.3 \cdot 10^6$
nb of K^+	43	727	2131	7884

Table 2.1: *Number of recorded central events and number of kaons identified in the four systems under investigation.*

2.2.4 Estimate of the background for K^+

Because of the resolution of the detector which translates into a broadening of the peaks in the mass distribution, kaons can not be separated from pions and protons in a background-free way. For high momenta, the kaon sample is contaminated by tails from pions and protons. As can be seen from the two-dimensional plots of Figure 2.10, the separation of kaons from pions and protons depends on momentum. Therefore, it is mandatory to investigate the background as a function of the momentum.

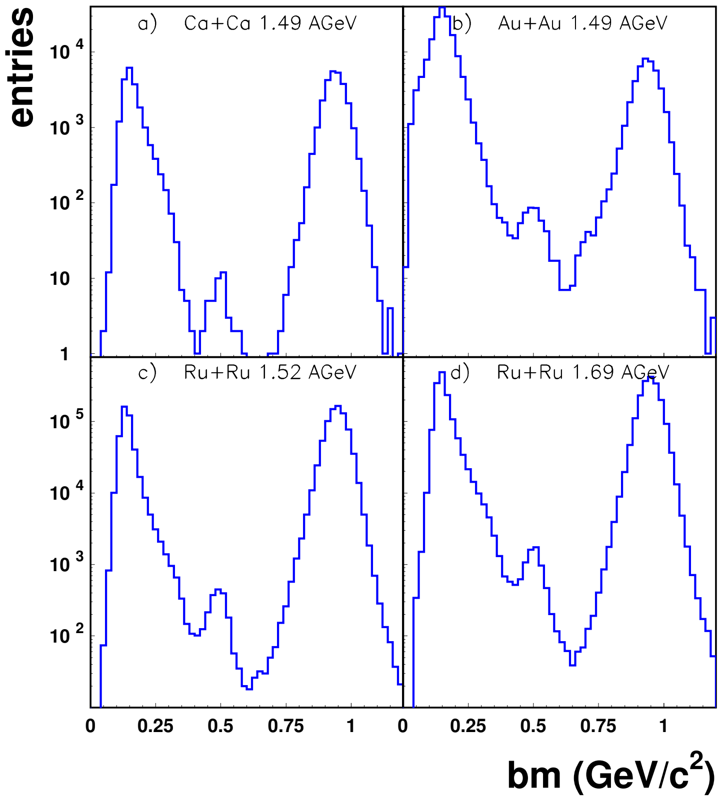

Figure 2.12: *BARREL mass distribution for: a) Ca+Ca at 1.49 AGeV with $p <$ 0.5 GeV/c, b) Au+Au at 1.49 AGeV with $p <$ 0.4 GeV/c, c) Ru+Ru at 1.52 AGeV with $p <$ 0.5 GeV/c, d) Ru+Ru at 1.69 AGeV with $p <$ 0.5 GeV/c with the cuts described in the text.*

For that purpose, the momentum range between 0.1 GeV/c and 0.5 GeV/c where kaons can be identified, has been divided in four bins. The mass distribution is plotted for each of these bins for Ru+Ru at 1.52 AGeV and 1.69 AGeV and Au+Au at 1.49 AGeV in Figure 2.13 using the cuts previously described.

With the low statistics in the Ca system, a small bining in momentum is not possible. But as can be seen from Figure 2.12, the kaon peak in this system with an upper momentum cut of 0.5 GeV/c is background free. For the other systems, it is also possible to identify kaons in a background-free way for the first bin in momentum. The estimate of the background in the other bins is not an easy task since the shape of the pion and proton tails is not well known.

In this analysis, the background has been estimated by fitting a gaussian function with $\sigma = 0.03$ GeV/c^2 to the kaon peak between 0.45 GeV/c^2 and 0.55 GeV/c^2 for eight momentum bins (each of the four previous bins has been divided in two bins to allow for a better representation of the dependence of the background on momentum). The integral of the gaussian function (S_{gauss}) is then subtracted from the number of entries between 0.4 GeV/c^2 and 0.6 GeV/c^2 (S_{tot}). The percentage of background as a function of the momentum $f_B(p)$ is given by:

$$\mathrm{f_B(p)} = \frac{\mathrm{S_{tot} - S_{gauss}}}{\mathrm{S_{tot}}} \tag{2.2}$$

The method is illustrated in Figure 2.13 for the four momentum bins considered in this case. The vertical lines correspond to the mass region considered for the background estimate (0.4 GeV/c^2 $<$ m $<$ 0.6 GeV/c^2). The dashed curve shows the gaussian function fitted to the kaon peak and which determines the signal.

The amount of background as a function of momentum is represented in Figure 2.14. This dependence is fitted with a straight line and gives a correction factor which is used in the analysis to subtract the background.

2.2.5 Matching and cut efficiency

With the cuts described above, the background is reduced but one also loses some signal. This has to be corrected for. The tracking and matching efficiency have to be taken into account as well.

For the tracking efficiency in the CDC, simulations were done using the GEANT package. The method and the results are presented in chapter 3.

The matching efficiency is defined as the ratio between the number of tracks found in the CDC within the acceptance of the BARREL and the number of tracks which have been matched to a hit in the BARREL. This efficiency is in average 90% for Ca+Ca at 1.5 AGeV, 78% for Ru+Ru at 1.5 AGeV, 83% for Ru+Ru at 1.69 AGeV and 75% for Au+Au at 1.5 AGeV. This method can not be applied directly to kaons because, as mentioned before, kaons can not be identified without the BARREL. However, one can assume that for a given momentum, the matching efficiency for protons and kaons is the same. This assumption is reasonable since the matching efficiency for protons and pions at a given momentum differs only by 6% which gives confidence that the matching efficiency for kaons is close to the value obtained for protons and pions. The small difference measured between pions and protons is taken into account in the systematic error when the efficiency correction is applied. The results are presented in Figure 2.15 (left panel) where the matching efficiency for pions (full histogram), protons (dashed histogram,) and deuterons (dotted histogram) is plotted as a function of the momentum for Ru+Ru collisions at 1.52 AGeV.

The cut efficiency is also determined for protons. The method is to compare the number of protons selected with the cuts used for the kaon identification as described above to the number of protons selected only with a cut on bm which is enough to identify protons properly. Figure 2.15 (right panel) shows the matching and cut efficiencies combined together as a function of the transverse mass ($m_t = \sqrt{p_t^2 + m_p^2}$) for the rapidity bin $-1.1 < Y^0 < -1.0$ where Y^0 is the rapidity in the center of mass normalized to the beam rapidity in the center of mass (with this normalization, 0 corresponds to mid-rapidity, -1 to the target rapidity and +1 to the projectile rapidity). The distribution is fitted by a straight line and this function is used to correct for the loss of particles due to the matching and selection cuts for kaons. Similar spectra are obtained for the other rapidity bins.

2.2.6 Decay correction

Charged kaons have a decay length $c\tau$ of 3.713 m. This implies that a fraction of them decay before reaching the BARREL.
The decay probability law for particles is given by:

$$\mathrm{P(x_0)} = \exp\left(\frac{-\mathrm{Mx_0}\Gamma}{\mathrm{p}}\right) \tag{2.3}$$

where $\Gamma = \frac{1}{c\tau}$, M is the mass of the particle, p its momentum and $\mathrm{x_0}$ the flight distance. This probability is plotted as a function of the transverse momentum in Figure 2.16. This function allows to correct for the loss of kaons due to their decay.

The minimum transverse momentum required for the particles to reach the BARREL is 0.1 GeV/c. According to Figure 2.16, most of the low energetic kaons decay before reaching the time of flight system and the correction factor is large, whereas only 35 % of the more energetic kaons are lost.

2.2.7 Estimate of systematic errors

The different contributions to the overall systematic error on kaon identification are reviewed.

The first contribution to the systematic errors comes from the identification procedure. The set of cuts implemented in the analysis to select kaons is described in section 2.2.3. The number of identified kaons with these cuts can be compared to the number of identified kaons with weaker and stronger cuts, taking into account the proper efficiency corrections. The difference between the standard cuts and both of the other cut sets is in the order of 10 %.

The second systematic uncertainty is due to the tracking and matching efficiencies which are known within 5 %.

The systematic error on the background contribution can be studied using different methods to estimate the background. Besides the method described in this work, another one has been investigated. It consists in fitting the tail of the proton and pion mass distributions with an exponential function which is extrapolated to the kaon mass region. The kaon peak is fitted with a gaussian function and the contribution of the tail in the pion and proton mass distributions is subtracted from the integral of the gaussian. This method leads to similar results as the ones presented in this work. Therefore the uncertainty on the background can be estimated to be less than 5 %.

2.2.8 Detector acceptance for K^+ and protons in the central part

The acceptance for protons and kaons in the central part of the FOPI detector is shown in Figure 2.17 in terms of the normalized transverse momentum as a function of the normalized rapidity for protons (left panel) and kaons (right panel) in Ru+Ru at 1.52 AGeV collisions. The normalized momentum is given by:

$$\left(\frac{\mathrm{p_t}}{\mathrm{m}}\right)^0 = \left(\frac{\mathrm{p_t}}{\mathrm{m}}\right) / \left(\frac{\mathrm{p_B^{cm}}}{\mathrm{M_p}}\right) \tag{2.4}$$

where m is the nominal mass of the considered particle, M_P is the nucleon mass and p_B^{cm} the beam momentum in the center of mass system.
The acceptance is limited by different boundaries. The first one is the angular coverage of the CDC/BARREL subsystem which is shown by the lines $\Theta_{lab} = 40°$ and $\Theta_{lab} = 130°$ in Figure 2.17. Furthermore a minimum transverse momentum of 0.1 GeV/c is necessary for the particles to reach the time of flight system. For kaons, an upper momentum cut is needed for a clean identification which reduces the acceptance of the FOPI detector.

2.3 Kaon identification in the forward part

As mentioned in the introduction, the kaon production probability is strongly correlated with the density reached in the fireball. The highest densities, where the in-medium effects are most pronounced, correspond to the region around mid-rapidity. For this reason it is extremely interesting to measure kaons at mid-rapidity.

Figure 2.18 shows the CDC/BARREL and HELITRON/PLAWA acceptance for Ru+Ru collisions at 1.69 AGeV for protons (left panel) and kaons (right panel). In the case of kaons, an upper momentum cut of 0.5 GeV/c has been applied for the CDC data and the momentum range between 0.4 GeV/c and 0.7 GeV/c has been selected for the HELITRON data. The choice of this cut is explained in section 2.3.2.

Since the acceptance of the HELITRON covers part of the mid-rapidity region for kaons, there is a strong interest to investigate to which extent the identification of kaons is feasible in the forward part of the FOPI detector. The ultimate goal is to measure the kaon production in the full phase space by combining data measured in the backward hemisphere with the CDC and the BARREL to data measured in the forward part with the HELITRON and the PLAWA. The Ru+Ru system at 1.69 AGeV offers the largest statistics and was chosen for this study.

A first attempt to identify kaons in the HELITRON has been done in the past and the results can be found in [Ple 99]. The present analysis confirms the possibility to identify kaons in this drift chamber. However some worrysome features in the kaon identification procedure have been demonstrated and could not be explained up to now. This makes the use of the combination of CDC and HELITRON data very delicate for the moment. No conclusive and reliable results could be obtained. The problems described in the following sections are still under investigation.

2.3.1 Mass identification

The HELITRON alone allows for a mass identification of particles by combining the measurement of the energy loss in the chamber and the determination of the momentum from the curvature of the track. This correlation is depicted in Figure 2.19 (left panel). The information provided by the HELITRON alone is not enough to identify clearly the kaons. To improve the quality of the particle identification in the forward part of the FOPI detector, the PLAWA can be used. For that purpose the tracks reconstructed in the drift chamber are matched to a hit measured in the plastic scintillators of the PLAWA as described in the next section. This allows to identify particles by using the correlation between their momentum measured in the HELITRON and their velocity measured in the PLAWA as shown in Figure 2.19 (right panel).

As in the CDC/BARREL sub-detector system, the redundancy of the mass measurement improves the particle identification. In what follows the mass refers to the quantity determined by the correlation between the momentum measured in the HELITRON and the velocity measured in the PLAWA.

2.3.2 HELITRON - PLAWA matching

Good matches between a track in the HELITRON and a hit in the PLAWA are selected with a window in $\mathrm{d}\phi$ and $\mathrm{d}\theta$ where $\mathrm{d}\theta = \theta_{\mathrm{HEL}} - \theta_{\mathrm{PLAWA}}$ and $\mathrm{d}\phi = \phi_{\mathrm{HEL}} - \phi_{\mathrm{PLAWA}}$. The resolution of $\mathrm{d}\theta$ is around 1° and the resolution in $\mathrm{d}\phi$ is around 0.8°. A pre-selection is realized using a window of $\pm 3^\circ$ for $\mathrm{d}\theta$ and $\mathrm{d}\phi$. In principle the same χ^2 variable (cf eq. 2.1) as in the case of the CDC/BARREL subsystem could be used to select the good matches

but a more careful study of dθ and dϕ dependences on other observables revealed some structures which have to be taken into account to obtain the best particle identification possible.
Figure 2.20 (left panel) shows $< d\phi >$ and $< d\theta >$ as a function of the mass reconstructed with the HELITRON momentum and the PLAWA velocity for a momentum range between 0.4 GeV/c and 0.6 GeV/c (the choice of this cut is explained in section 2.3.3).

The mean value $< d\phi >$ is around $-0.5°$ for π^+ and $-0.4°$ for protons whereas it is around 1° for π^-. The difference in $d\phi$ between positively and negatively charged particles is not yet understood but since pions and protons are reasonably well identified, one expects the same $< d\phi >$ for kaons.
As can be seen in Figure 2.20, $< d\phi >= -0.1°$ in the mass region of kaons. No reason could be found why the value of $< d\phi >$ should be different for kaons than for other particles. This shift is attributed to the presence of a background, showing different properties than the real tracks. The origin of this background could not be identified up to now. But under the assumption that good tracks for positively charged particles must have a $< d\phi >$ around $-0.5°$, cutting on this observable provides a way to eliminate the background to a certain extent. This effect is shown in Figure 2.20 (right panel). The mass distribution is plotted for $d\phi < 0$ and $d\theta < 0$ (full histogram) and $d\phi > 0$ and $d\theta > 0$ (dashed histogram) for momenta between 0.4 and 0.6 GeV/c. The full histogram shows a clear kaon peak whereas the bump observed in the kaon mass region in the dashed histogram can not be interpreted as a kaon peak.
Selecting the negative part of $d\phi$ and $d\theta$ has the drawback of reducing the statistics by a factor of two. It is, however, necessary to suppress the background as much as possible for a kaon identification in the forward hemisphere.

2.3.3 Influence of the staggering on K^+ identification

The staggering is described in section 2.1. A detailed study of the patterns of this observable revealed some dependencies which are not completely understood yet. However, this observable allows to improve the kaon identification in the forward part of the detector.

The main observation is seen in Figure 2.21 (left panel) which shows the mass reconstructed from the HELITRON momentum and the PLAWA velocity as a function of the staggering. The background between protons and deuterons is larger on the positive side than on the negative side of the staggering. For this reason, the larger number of entries between pions and protons on the positive side of the staggering can not be interpreted as a larger amount of kaons but rather as a larger background. One can also notice that for the negatively charged particles, the background is higher on the negative side of the staggering. The consequence of this background is to deteriorate the mass resolution which makes the separation between pions, kaons and protons more difficult.

Figure 2.21 (right panel) shows the mass distribution plotted for both sides of the staggering separately. For the positively charged particles, the distribution obtained for the negative staggering (full histogram) shows better separation between the peaks and a higher efficiency than for the positive side (dashed histogram). In a general way, one can say that the negative (resp. positive) side of the staggering provides a better track quality for the positively (resp. negatively) charged particles.

This investigation shows that there is a clear correlation between the staggering and the quality of the mass identification, both in terms of background contamination and of efficiency. It is necessary to reject the bad side of the staggering, to improve the particle identification. It is in particular very important for the kaon identification. But in this case as well, the statistics is reduced by a factor of two.

2.3.4 Momentum range for K^+ identification

The momentum range accessible in the HELITRON/PLAWA subsystem has been divided in bins of 0.1 GeV/c between p = 0.2 GeV/c and p = 0.8 GeV/c to investigate the possibility of identifying kaons depending on the momentum. The mass distribution for each of these bins is represented in Figure 2.22.

The negative side of the staggering has been selected and the matching has been done with the conditions $d\phi < 0$ and $d\theta < 0$. For momenta below 0.4 GeV/c and above

0.7 GeV/c it is not possible to identify kaons in the HELITRON/PLAWA sub-detector. The bump in the kaon mass region is most probably due to background. Only in the intermediate momentum range, which corresponds to the mid-rapidity region, a clear signal appears.

2.3.5 Summary on kaon identification in the HELITRON

Taking into account the cuts on the matching observables and on the staggering previously described, it was possible to identify kaons in the forward part of the FOPI detector (HELITRON + PLAWA) for the system Ru+Ru at 1.69 AGeV as can be seen in Figure 2.23. The mass distribution is plotted for the negative side of the staggering, with $d\phi < 0$ and $d\theta < 0$ as was explained in the previous sections, for the momentum range between 0.4 GeV/c and 0.7 GeV/c. A clear peak appears in the kaon mass region although the statistics is strongly reduced by the cuts needed to identify kaons.

The goal of this investigation was to combine the spectra measured in the CDC/BARREL subsystem with the ones measured in the forward part of the FOPI detector, to cover a phase space as large as possible. Unfortunately, there is a discrepancy at high energy between the number of protons measured in the CDC (backward hemisphere) and in the HELITRON (forward hemisphere). For symmetric systems, one expects the same yields in two rapidity windows which are symmetric around mid-rapidity. This is not the case in the data when one compares the number of protons measured in the CDC and in the HELITRON, although the corresponding efficiencies are taken into account. Furthermore, if one selects a rapidity window in the backward hemisphere and the same rapidity window in the forward hemisphere (symmetric around mid-rapidity), the slope of m_t-spectra measured forwards differs from the one measured backwards, which is not expected. These two features are illustrated in Figure 2.24. The m_t spectra are plotted for protons in the CDC (full dots) and in the HELITRON (open dots) in two rapidity windows symmetric around mid-rapidity.

These discrepancies could not be understood up to now and require further work. It makes the combination of CDC and HELITRON data very delicate and uncertain at this stage of the work.

A first step towards a better understanding of the difference between the two sides of the staggering has been made recently. The effect would come from the momentum determination. The usual procedure to determine the momentum is to fit the hits measured in the HELITRON, taking into account the target position. The curvature of the reconstructed track gives the particle momentum. If the matching to the PLAWA hits is performed as described above, a second iteration of the fit procedure can be realized, including in addition the corresponding hit in the PLAWA, which constrains the fit. This allows to improve the momentum resolution. First tests show that using the momentum determined after matching cancels the difference between negative and positive staggering. The next steps would be to perform detailed simulations of the HELITRON response, using GEANT. This would allow to better understand the performances of this drift chamber.

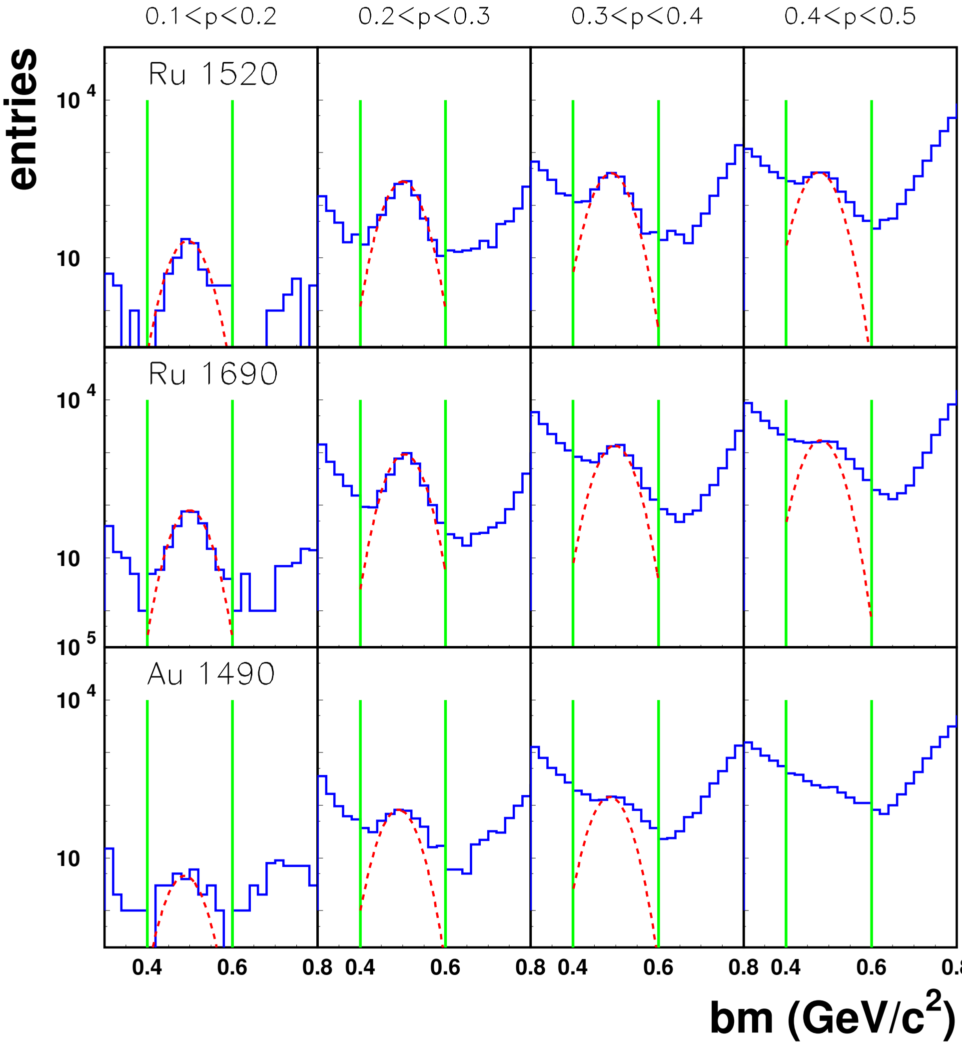

Figure 2.13: *Mass distribution for Ru+Ru at 1.52 AGeV, Ru+Ru at 1.69 AGeV and Au+Au at 1.49 AGeV with the cuts previously described for four bins in momentum:* $0.1 < p < 0.2, 0.2 < p < 0.3, 0.3 < p < 0.4$ *and* $0.4 < p < 0.5$ *GeV/c. The vertical lines show the mass region considered for the background determination. The dashed curves show the gaussian function with* $\sigma = 0.03 GeV/c^2$ *used to estimate the signal.*

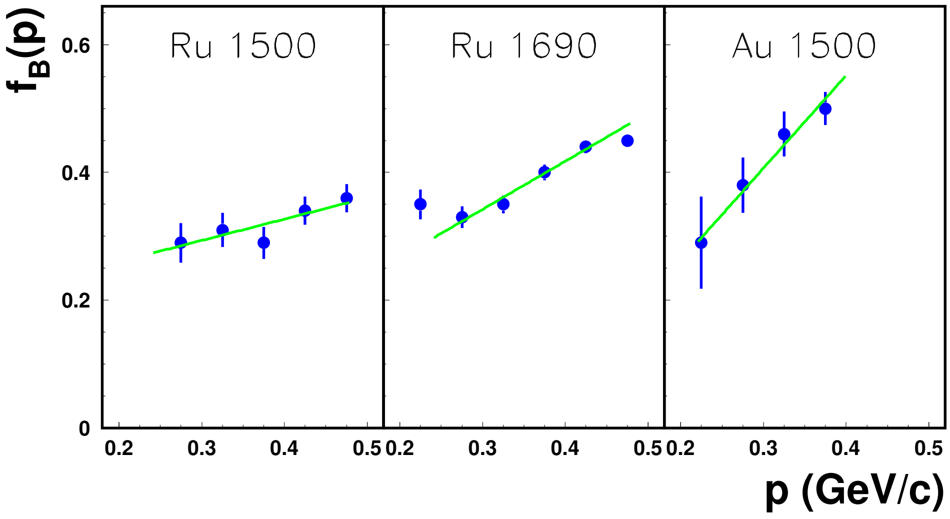

Figure 2.14: *Contribution of the background for kaons as a function of the momentum for Ru+Ru at 1.52 AGeV, Ru+Ru at 1.69 AGeV and Au+Au at 1.49 AGeV.*

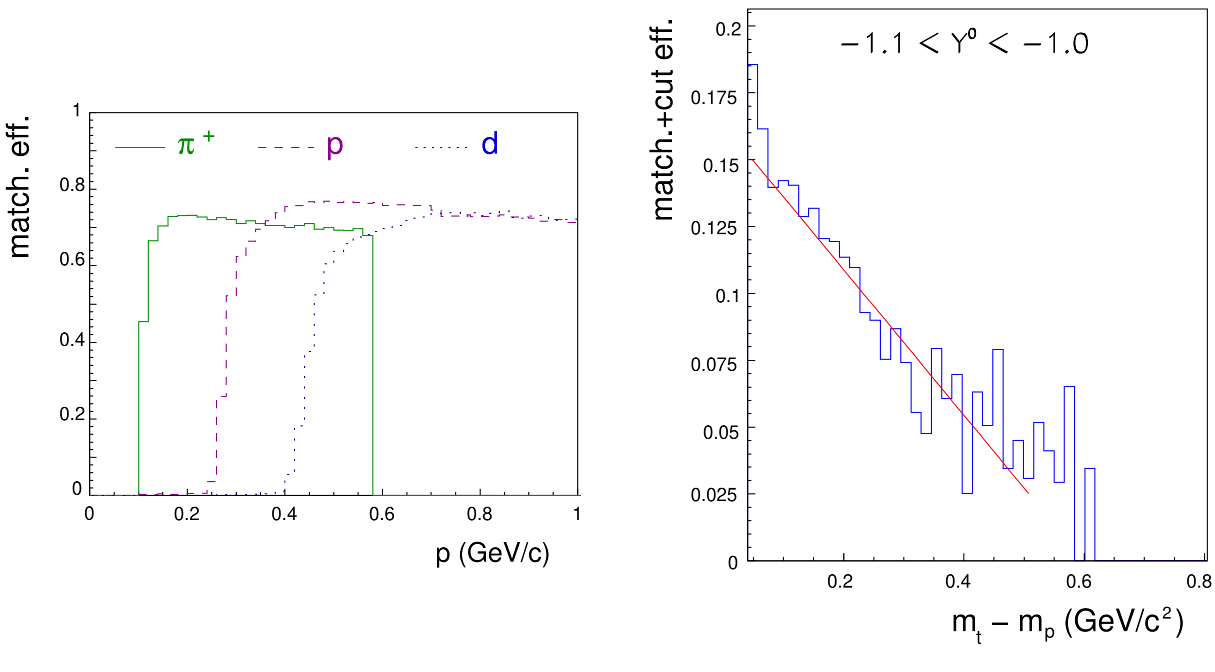

Figure 2.15: *Matching efficiency between the BARREL and the CDC for π^+ (full histogram), p (dashed histogram) and d (dotted histogram) as function of the momentum (left panel) and matching and cut efficiencies combined together for protons as a function of the transverse mass for $-1.1 < Y^0 < -1.0$ in Ru+Ru at 1.52 AGeV.*

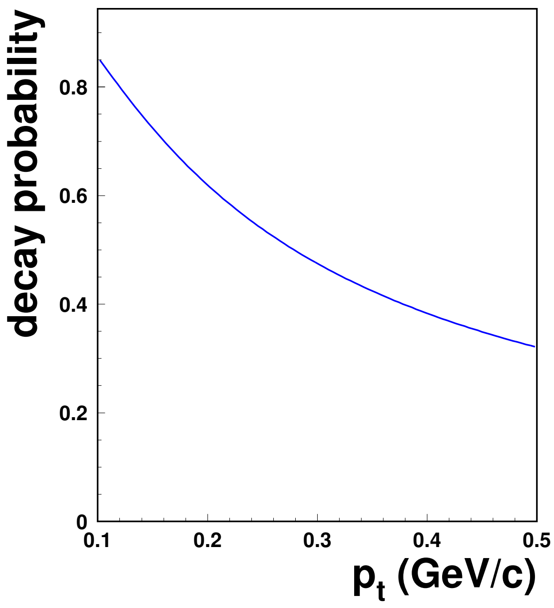

Figure 2.16: *Decay probability of charged kaons as a function of their transverse momentum for the flight distance between the target and the BARREL.*

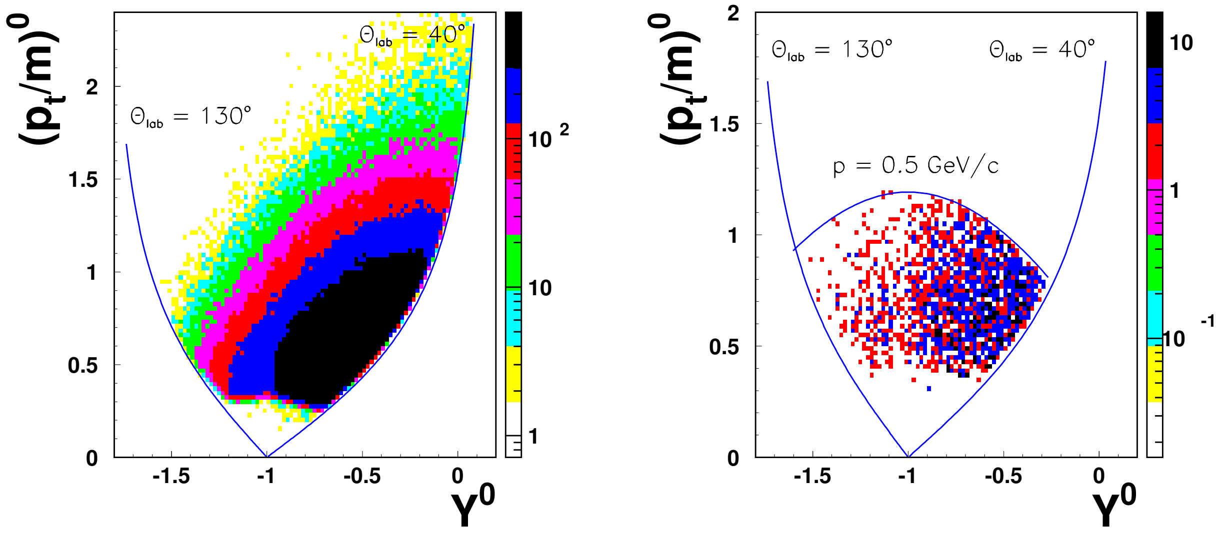

Figure 2.17: *Detector acceptance in the central part of the FOPI detector for protons (left panel) and charged kaons (right panel) in Ru+Ru at 1.52 AGeV.*

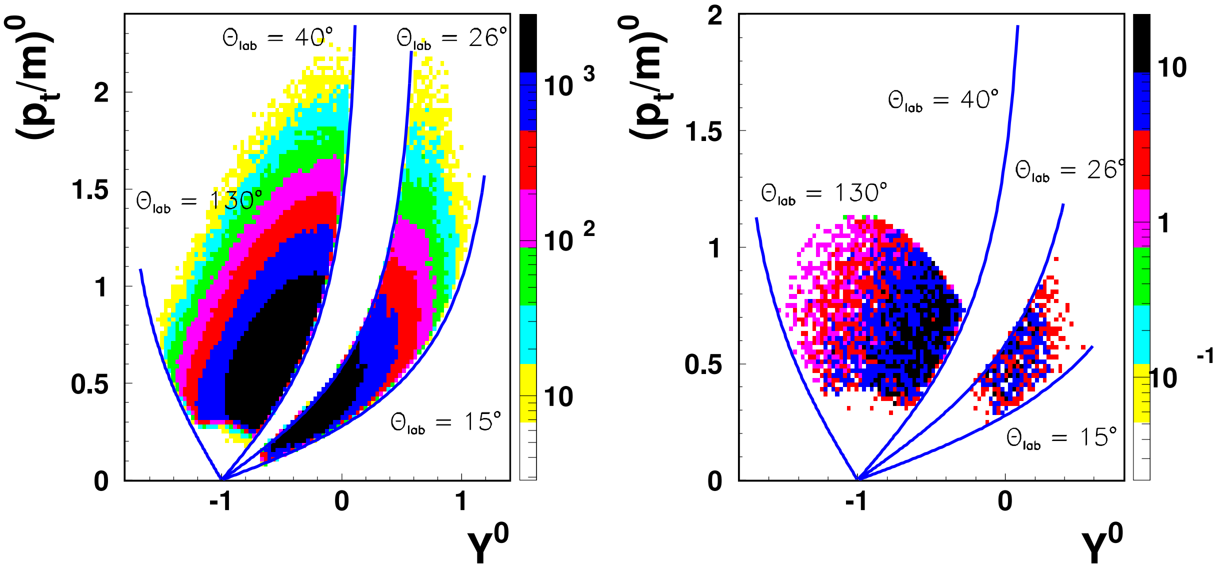

Figure 2.18: *Acceptance of the FOPI detector for protons (left panel) and kaons (right panel) in Ru+Ru collisions at 1.69 AGeV. The lines correspond to the polar angle coverage of the CDC/BARREL subsystem (*$40° < \theta_{lab} < 130°$*) and of the HELITRON/PLAWA subsystem (*$15° < \theta_{lab} < 26°$*).*

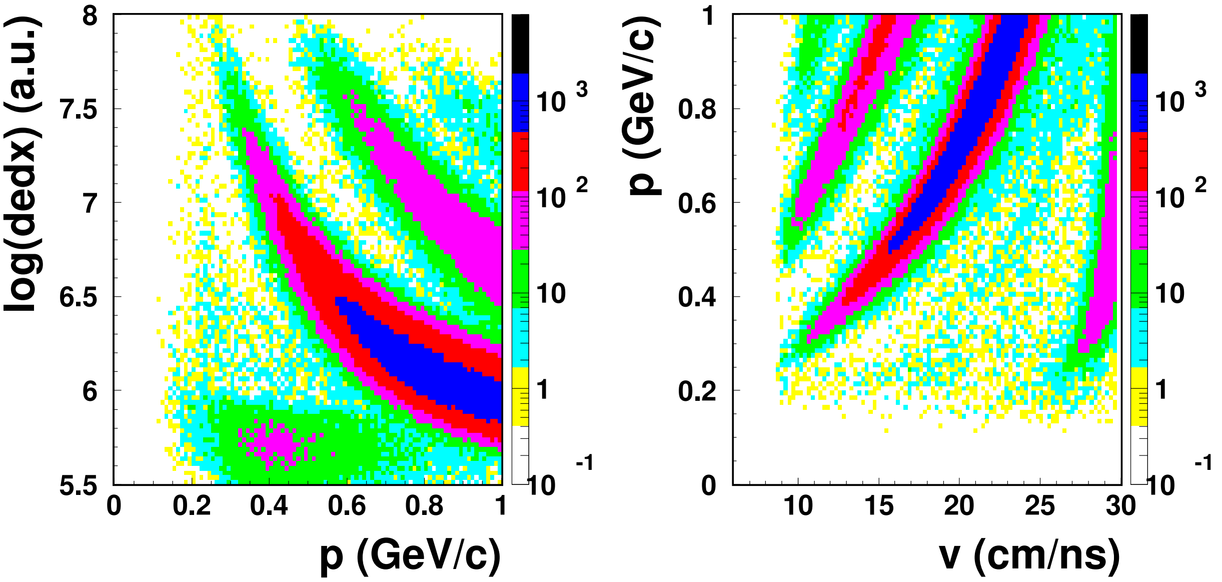

Figure 2.19: *Energy loss in the HELITRON as a function of the momentum (left panel) and momentum as a function of the velocity measured in the PLAWA (right panel).*

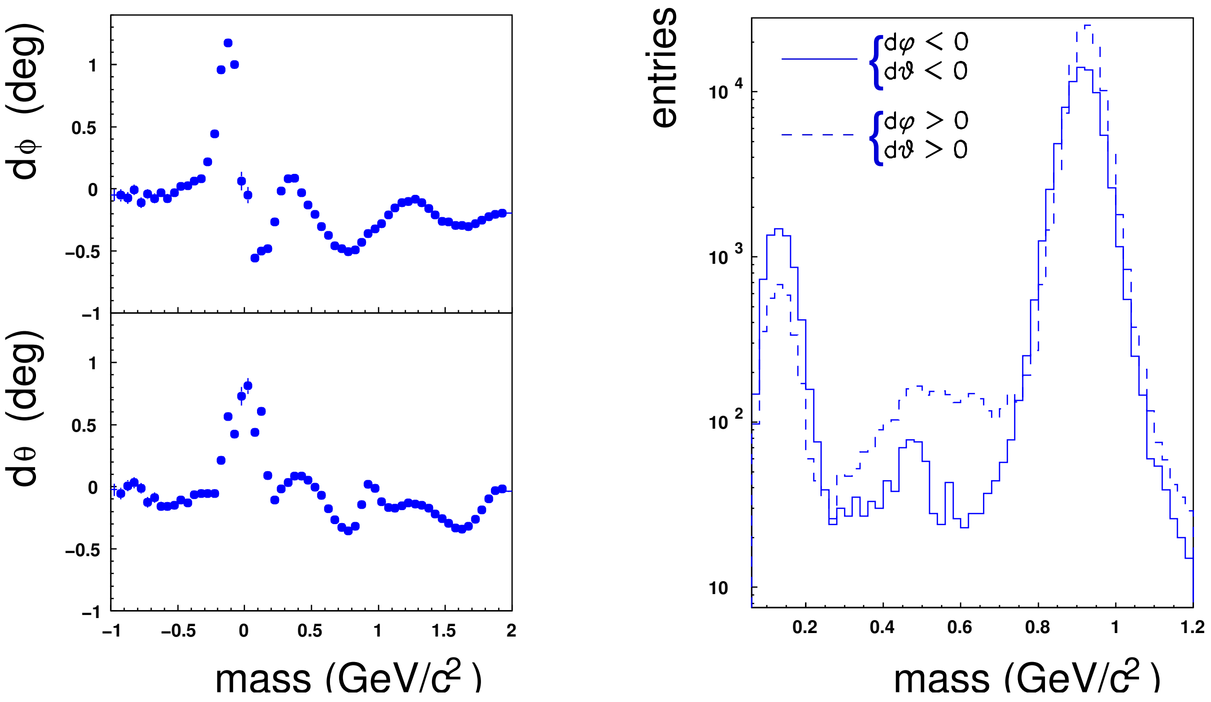

Figure 2.20: *$d\phi$ and $d\theta$ as a function of the mass for Ru+Ru at 1.69 AGeV (left panel) and mass distribution for Ru+Ru at 1.69 AGeV collisions with $d\phi < 0$ and $d\theta < 0$ (full histogram) and $d\phi > 0$ and $d\theta > 0$ (dashed histogram) (right panel).*

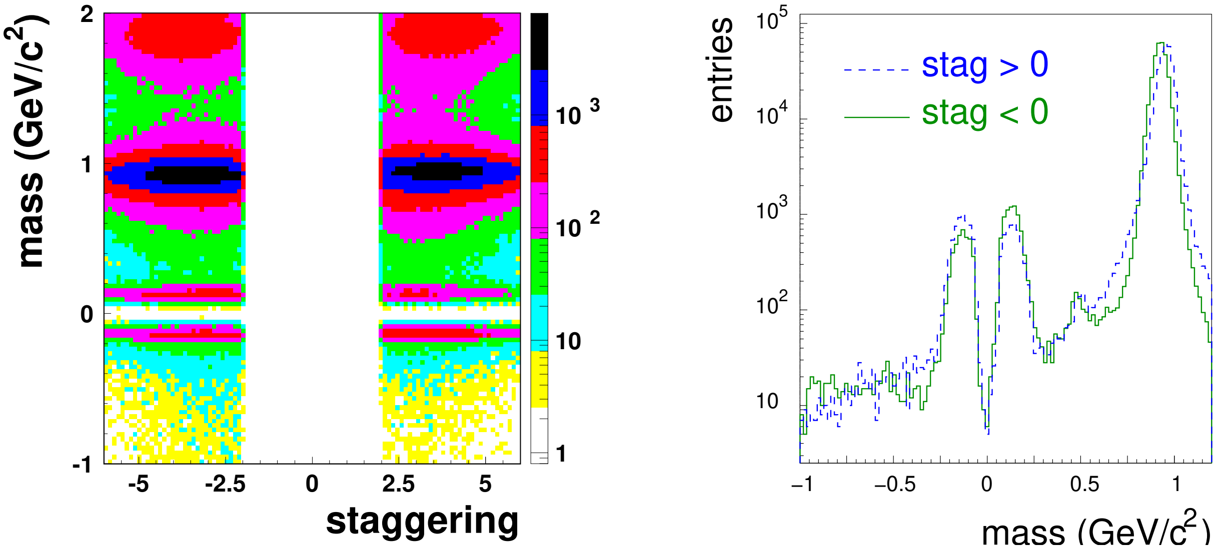

Figure 2.21: *Mass determined with the momentum measured in the HELITRON and the velocity measured in the PLAWA as a function of the staggering for Ru+Ru at 1.69 AGeV (left panel) and mass distribution for stag > 0 (dashed histogram) and stag < 0 (full histogram).*

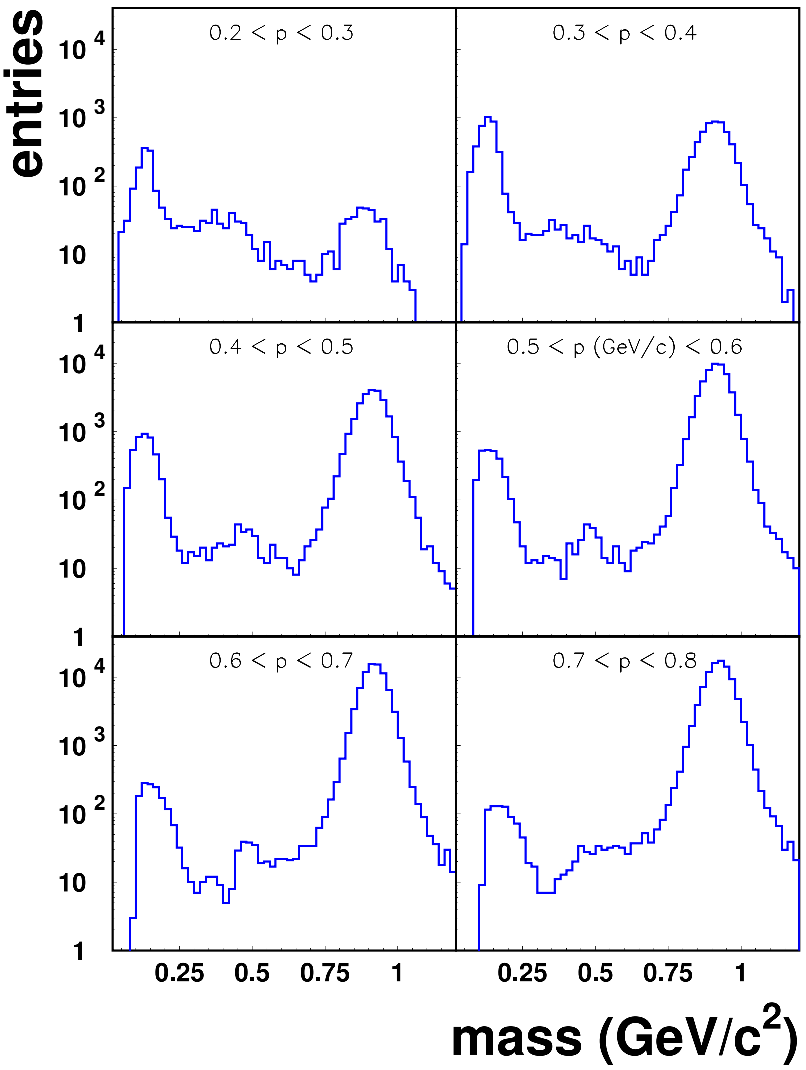

Figure 2.22: *Mass distribution for Ru+Ru at 1.69 AGeV for 6 momentum bins between 0.2 GeV/c and 0.8 GeV/c for the negative side of the staggering and with* $d\phi < 0$ *and* $d\theta < 0$.

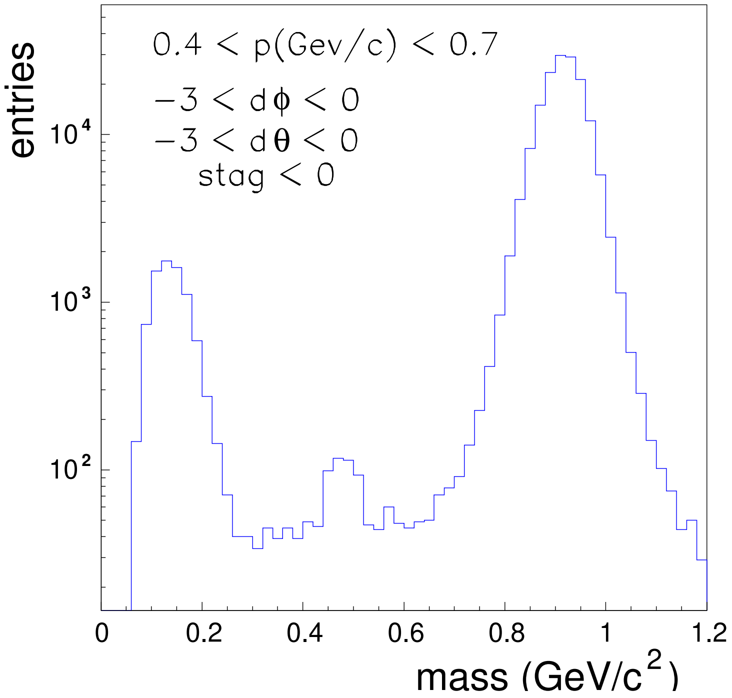

Figure 2.23: *Mass distribution for Ru+Ru at 1.69 AGeV collisions for* $0.4 < p < 0.7$ *GeV/c and* $-3 < d\phi < 0$, $-3 < d\theta < 0$ *and stag* < 0 *in the HELITRON/PLAWA subsystem.*

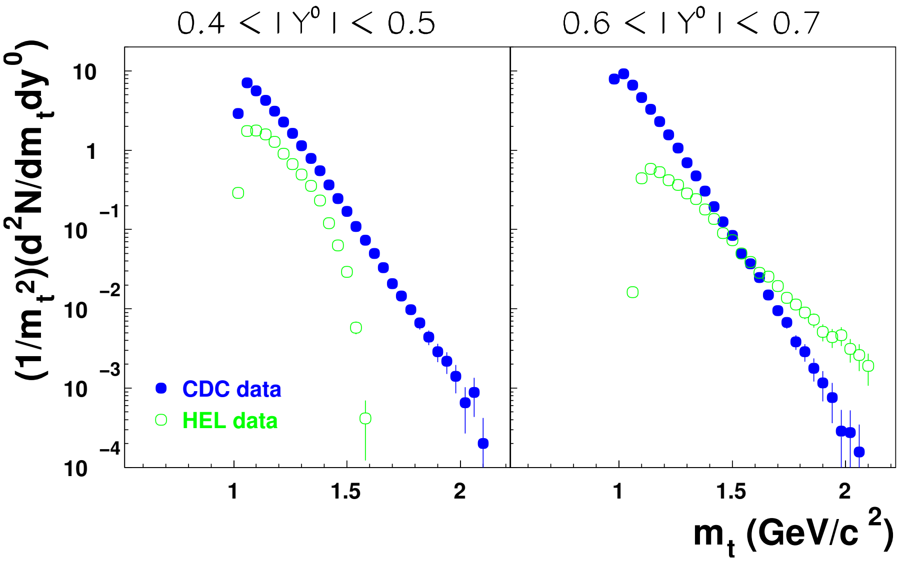

Figure 2.24: *m_t-spectra for protons in the CDC (full circles) and in the HELITRON (open circles) in Ru+Ru collisions at 1.69 AGeV. Two rapidity windows have been selected:* $-0.5 < Y^0 < -0.4$ *for the CDC data and* $0.4 < Y^0 < 0.5$ *for the HELITRON data (left panel) and* $-0.7 < Y^0 < -0.6$ *for the CDC data and* $0.6 < Y^0 < 0.7$ *for the HELITRON data (right panel)*

Chapter 3

Geant simulation

Investigating the production probability of particles requires to have a good handle on the efficiency of the apparatus. Matching and cut efficiencies can be determined from the experimental data directly as explained in the previous chapter. This is not possible for the tracking efficiency. For that purpose, simulations using the GEANT package [Bru 78] have been done. The FOPI detector response has been parametrized, taking into account the hit recognition in the drift chamber and the front end electronic response. IQMD events are then used as input to GEANT and analysed in the very same way as the experimental data, using the same tracking algorithm. This method provides realistic results since the track multiplicity in the IQMD events is comparable to the one measured with the FOPI detector. It is also interesting to investigate the performances of the tracker depending on the system under consideration. Indeed, the particle multiplicities in a heavy system as Au+Au for instance is rather high and makes the track finding more complicated.
In this chapter, results on tracking efficiency for Ca, Ru and Au systems are presented.

3.1 Method to determine the tracking efficiency

The simulation environment offers the possibility to compare the initial number of tracks in an event to the number of tracks found by the tracking algorithm. Only particles with Z=1 are selected. The method to obtain the tracking efficiency is to build the ratio between the momentum distribution of all particles found by the tracking algorithm and the initial momentum distribution. This is done in the CDC acceptance, defined by the polar angular range between 40° and 130°.

Only tracks with a number of hits (nh) larger than 20 are selected. Indeed, fake tracks may be created by the tracker when a particle crosses two sectors of the CDC. If the junction between the two parts of the track at the sector border is not properly done, the tracker may identify two tracks instead of one. Requiring a minimum number of hits of 20 allows to reject most of these fake tracks. This may introduce a little bias since the number of hits per track is not the same for each particle specie. However, the mean value of nh is 34 for pions and 43 for protons. This values are well above the cut of 20 used in this analysis which means that the effect of this cut on the result is limited.
This cut is not necessary for kaon identification in the experimental data because the cut on the matching observables already reduces the background. When applying the selection criteria described in chapter 2, a cut on the number of hits per track does not bring any further improvement.

3.2 Results for the tracking efficiency

The IQMD events have been produced for the four systems under investigation in this work and a tracking efficiency has been estimated in each case, using the method described above. The results are presented in Figure 3.1 which shows the tracking efficiency as a function of the momentum for Z=1 particles in Ca+Ca and Au+Au at 1.49 AGeV and Ru+Ru at 1.52 and 1.69 AGeV.

The decrease of the efficiency observed at very low momenta does not reflect a feature of the tracker. It is due to the fact that low momenta particles can not be identified in the CDC since the low momenta region corresponds to the target rapidity domain as can be seen in Figure 3.2 which shows the CDC acceptance for proton tracks. Before tracking, protons are selected by their identification number in GEANT. The left panel of Figure 3.2 corresponds to the initial distribution whereas the right panel is obtained after the tracking algorithm. The missing low momenta particles in the CDC have been absorbed in the target.

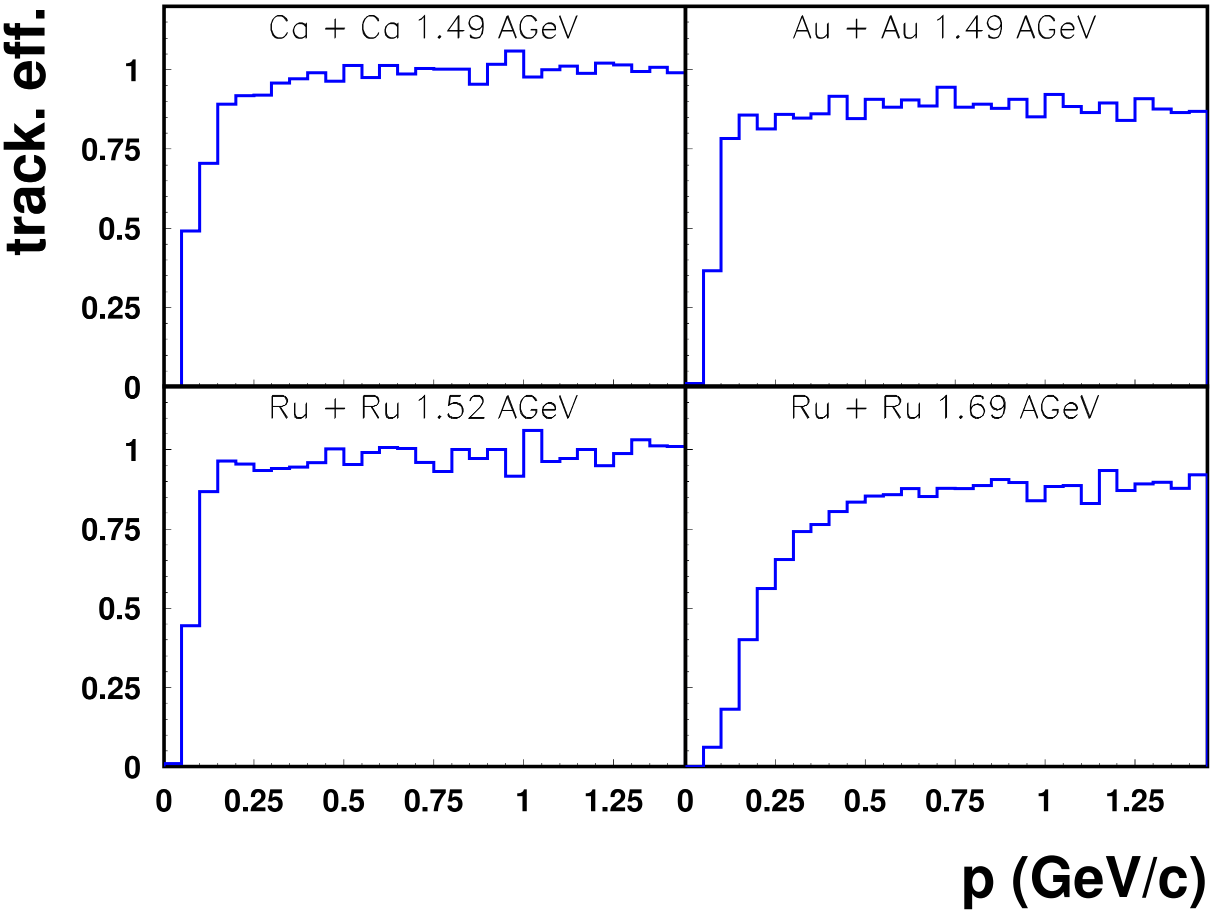

Figure 3.1: *Tracking efficiency as a function of the momentum for Z=1 particles in Ca+Ca and Au+Au collisions at 1.49 AGeV and Ru+Ru collisions at 1.52 AGeV and 1.69 AGeV in the CDC acceptance.*

The effect of the target can be checked by looking at the tracking efficiency as a function of the transverse momentum for two rapidity windows, one around target rapidity ($-1.1 < Y^0 < -0.9$) and one at smaller rapidities, where the particle identification is not affected by the presence of the target ($-0.7 < Y^0 < -0.5$). This has been done for protons in Ca+Ca collisions at 1.49 AGeV. The results are presented in Figure 3.3. In the first rapidity bin (left panel), the efficiency decreases quickly at low transverse momenta whereas in the other rapidity bin (right panel), a plateau appears down to low momenta. The region of low momenta particles is not representative of the tracking efficiency since these particles can not be measured properly in the CDC

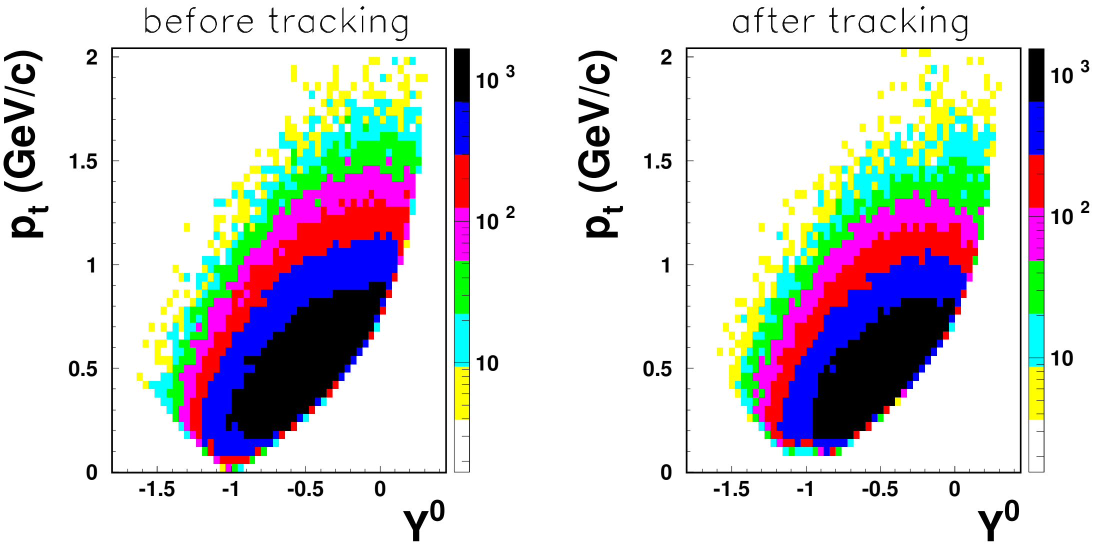

Figure 3.2: *CDC acceptance for protons in Ca+Ca collisions at 1.49 AGeV before (left panel) and after (right panel) the tracking algorithm.*

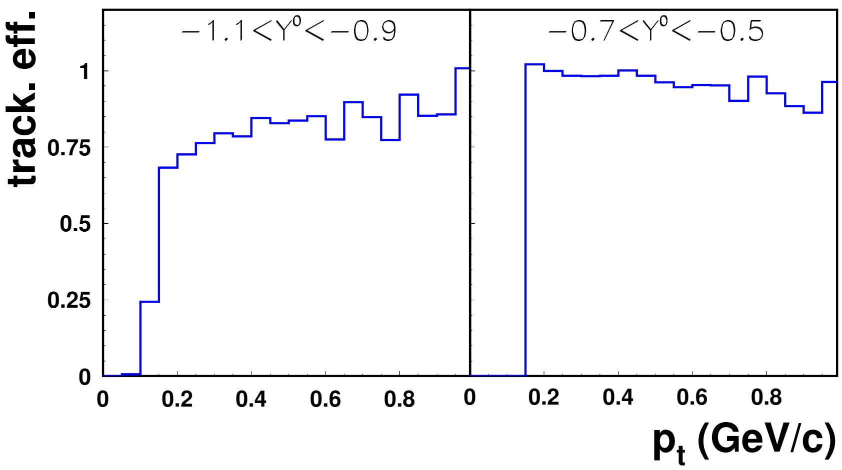

Figure 3.3: *Tracking efficiency for protons in Ca+Ca collisions at 1.49 AGeV for two rapidity windows,* $-1.1 < Y^0 < -0.9$ *and* $-0.7 < Y^0 < -0.5$

Since the results at very low momenta are biased by the presence of the target, this region can not be used to determine the tracking efficiency. The distributions in Figure 3.1 show a clear plateau which gives the tracking efficiency for each system. The values are summarized in Table 3.1.

Ca 1.49 AGeV	Au 1.49 AGeV	Ru 1.52 AGeV	Ru 1.69 AGeV
0.99	0.87	0.97	0.89

Table 3.1: *Tracking efficiency for protons in Ca+Ca at 1.49 AGeV, Au+Au at 1.49 AGeV and Ru+Ru at 1.52 and 1.69 AGeV.*

As expected, the tracking efficiency is lower in heavy systems for which the particle multiplicity is higher than in light systems. However, the difference between the Ca system and the Au system is only in the order of 10 % which accounts for the good performances of the tracking algorithm, even in a large multiplicity environment.
The systematic error made on the tracking efficiency is around 5%. It influences the yield of particles but does not play a significant role in the systematic of kaon production.
The data presented in chapter 4 have been corrected for the tracking efficiency using the values of Table 3.1

Chapter 4

Experimental results

In this chapter, experimental results are discussed. Results on K^+ production are presented . The rapidity distributions are determined in Ru+Ru at 1.52 and 1.69 AGeV only. This kind of analysis could not be performed for the Ca and Au systems due to the low available statistics. However, the K^+ multiplicity is measured in the CDC/BARREL acceptance for all the systems and the number of kaons per participant is investigated as a function of the number of participants for Ca+Ca, Ru+Ru and Au+Au at 1.5 AGeV. This allows to study the dependence of kaon production on centrality and on system size.

The protons have been measured as well in Ca+Ca and Au+Au reactions at an incident energy of 1.49 AGeV and in Ru+Ru reactions at incident energies of 1.52 and 1.69 AGeV. Their apparent temperature and their rapidity distributions are compared to the distribution obtained under the assumption of an isotropically expanding source.

4.1 Centrality selection

As explained in section 2.2.2, the centrality of a collision is determined by the measurement of the charged particle multiplicity pmul in the PLAWA. Figure 4.1 shows the multiplicity distributions for the four systems under investigation. The dashed histograms correspond to the minimum-bias trigger and the dotted histograms to the central trigger. The integral of these distributions, which are obtained with open cuts on the vertex, corresponds to the measured cross section in mb. The full histrogram shows the multiplicity distributions for events containing a K^+ candidate, using the criteria for kaon identification described in chapter 2.

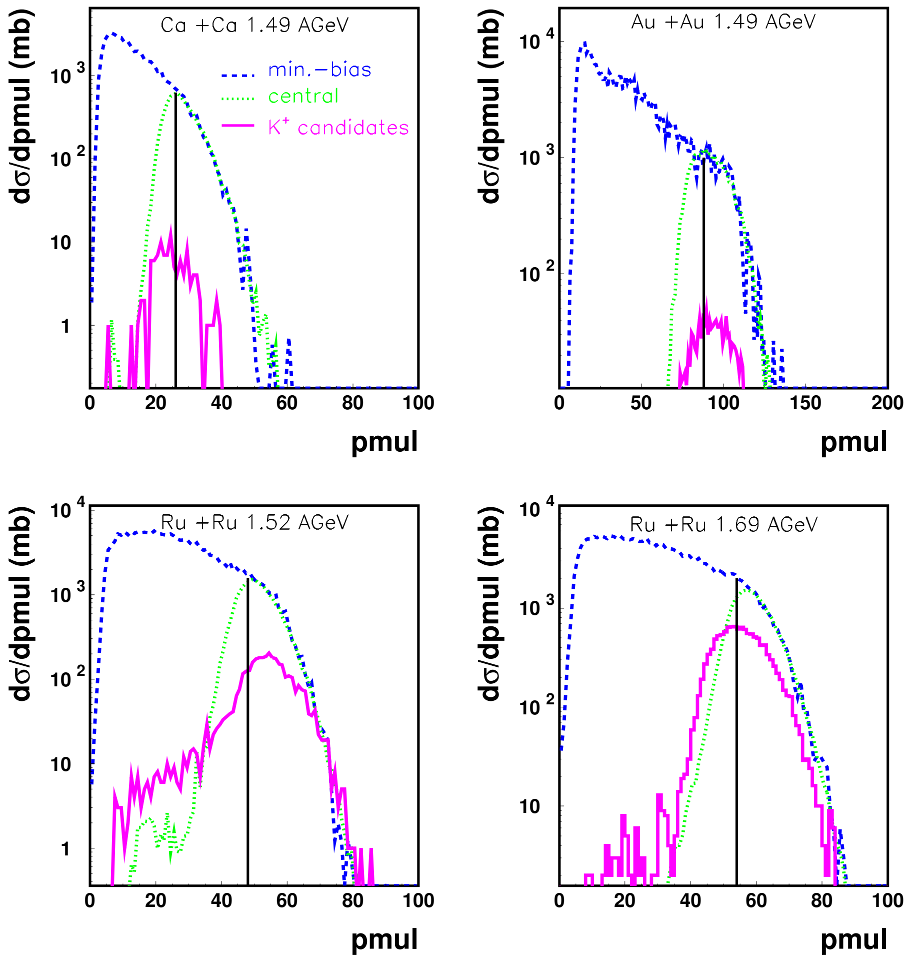

Figure 4.1: *Charged particle multiplicity in the PLAWA for the systems Ca+Ca at 1.49 AGeV, Au+Au at 1.49 AGeV and Ru+Ru at 1.52 AGeV and 1.69 AGeV. The dashed histograms correspond to the minimum-bias trigger and the dotted histogram to the central trigger. The full histograms are the multiplicity distributions for the events containing a* K^+ *candidate. The vertical lines show the cut imposed on pmul to select 10% of the geometrical cross section.*

The K^+ candidates are found preferentially in central collisions. The event selection has to be done in such a way that the collisions are sufficiently central without losing too much statistics for the investigation of kaon properties. Selecting 10% of the geometrical cross section was found to be a good compromise between the centrality and the statistics.

The geometrical cross section for an impact parameter range between 0 and b_{max} is given by:

$$\sigma_{geo} = 10\pi b_{max}^2 \tag{4.1}$$

with b_{max} in fm and σ_{geo} in mb. For the case of a symmetric system, involving two nucleus with A nucleons, b_{max} is deduced from the nuclei radius by $b_{max} = 2R_A$ with $R_A = 1.2A^{1/3}$.

A normalization factor is used for each trigger selection to convert the measured multiplicities into cross sections. Ideally, the integral of the distributions should give the geometrical cross section in mb. But due to experimental limitations, the total measured cross section does not correspond to the geometrical cross section. The low multiplicity region, corresponding to very peripheral collisions is missing. However, the selection of central events is not affected since they correspond to the high multiplicity part of the distributions which does not show experimental bias.

As mentioned above, the central events selected in this analysis correspond to 10% of the geometrical cross section. Using the measured multiplicity distributions which provide a good estimate of the geometrical cross section for high multiplicities, a cut in pmul is defined for each system. This cut is shown by the vertical lines in Figure 4.1.

4.2 Determination of the number of participants

As mentioned in the introduction, only the nucleons which are in the overlapping zone of the two colliding nuclei participate to the reaction. Within a spherical model, the number of participants to the reaction can be related to the impact parameter, which is deduced from the cross section according to equation 4.1. Figure 4.2 shows the average number of participants A_{part} for an impact parameter range between 0 and b_{max} as a function of b_{max}. The quantity b_{max} is calculated in the following way:

$$b_{max} = \sqrt{\frac{\sigma}{10\pi}} \tag{4.2}$$

with b_{max} in fm and σ corresponding to the cross section of the considered event class in mb.

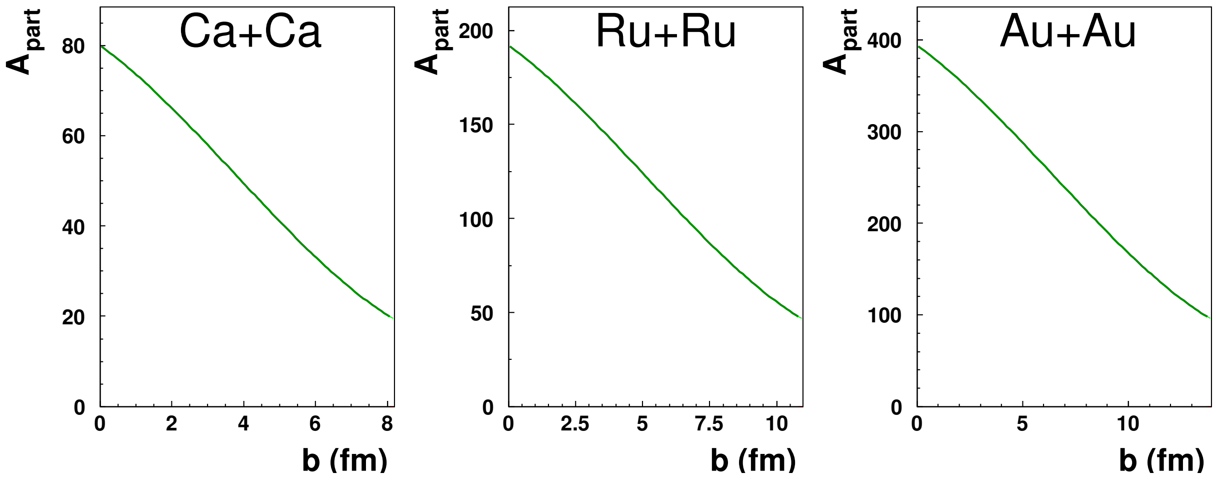

Figure 4.2: *Average number of participants for an impact parameter range between 0 and b_{max} in Ca+Ca, Ru+Ru and Au+Au collisions.*

For each system, the cross section for the selected central events has been estimated as well as the corresponding maximum impact parameter. The values for the maximum impact parameter, the total cross section, the minimum pmul and the impact parameter corresponding to 10% of the geometrical cross section σ_{geo} and the number of participants are summarized in Table 4.1

system	A	$b_{\max}$ (fm)	σ_{tot} (mb)	pmul	b (fm)	A_{part}
Ca 1.49 AGeV	40	4.10	2111	26	2.6	61
Ru 1.52 AGeV	96	10.98	3790	48	3.4	148
Ru 1.69 AGeV	96	10.98	3790	54	3.4	148
Au 1.49 AGeV	197	13.94	6100	88	4.4	302

Table 4.1: *Characteristics for each system: maximum geometrical impact parameter b_{max} (in fm), geometrical cross section σ_{geo} (in mb) given by equation 4.1, cut on the multiplicity of charged particles measured in the PLAWA pmul and corresponding impact parameter b for a selection of 10% of the geometrical cross section σ_{tot} and number of participating nucleons.*

4.3 $\mathrm{m_t}$-spectra and rapidity distributions

The determination of a production cross section is achieved by the measurement of particle yields, which can be deduced from rapidity distributions for instance. This provides in addition valuable information on the particle phase space distribution in the longitudinal direction.

4.3.1 Description of the method

The method to obtain yields is based on the measurement of transverse mass spectra. The transverse mass is defined by $\mathrm{m_t} = \sqrt{\mathrm{p_t^2 + m_0^2}}$, with $\mathrm{p_t}$ the transverse momentum of the particle and m_0 its nominal mass at rest. For a thermalised system, the spectra can be parametrized with a Boltzmann-type function in a narrow rapidity window as shown by the equation 4.3.

$$\frac{1}{\mathrm{m_t^2}}\frac{\mathrm{d^2N}}{\mathrm{dm_t dY^0}} = \mathrm{A(Y^0)} \cdot \exp\left(\frac{-\mathrm{m_t}}{\mathrm{T_B(Y^0)}}\right) \tag{4.3}$$

The fit parameters A and $\mathrm{T_B}$ are the normalization and the inverse slope parameter respectively, the later being interpreted as the apparent temperature of the emission source at the freeze-out. Both parameters depend on the rapidity and have to be estimated for each rapidity window. In a logarithmic representation and if the system is thermalised, the spectra appear as a straight line. This is valid if there is no flow. In the presence of flow, the spectra will show a shoulder-arm behavior at low transverse momenta. This effect is discussed below in more details for protons.

The data are measured in the CDC/BARREL sub-detector which corresponds to the backward hemisphere ($\mathrm{Y^0} < 0$). The acceptance of the central part of the FOPI detector for protons is quite large and it is possible to identify protons very close to mid-rapidity for high transverse momenta as can be seen in Figure 2.17. This is not the case for kaons, the acceptance being limited by the upper momentum cut p < 0.5 GeV/c.

Figure 4.3 shows the $\mathrm{m_t}$-spectra for protons in central Ru+Ru collisions at 1.52 AGeV, the centrality being selected as described in section 4.1. Protons are identified as kaons in the CDC/BARREL sub-detector. The spectra are corrected for tracking and matching efficiencies. The m_t-spectra are plotted for narrow rapidity bins from target rapidity, at the lowest part of Figure 4.3, to mid-rapidity, at the upper part. For plotting purpose, each spectra has been multiplied by 10^n with n varying between 0 and 11. The lines correspond to the fit using the formula 4.3. Similar spectra were obtained for protons identified in the other systems.

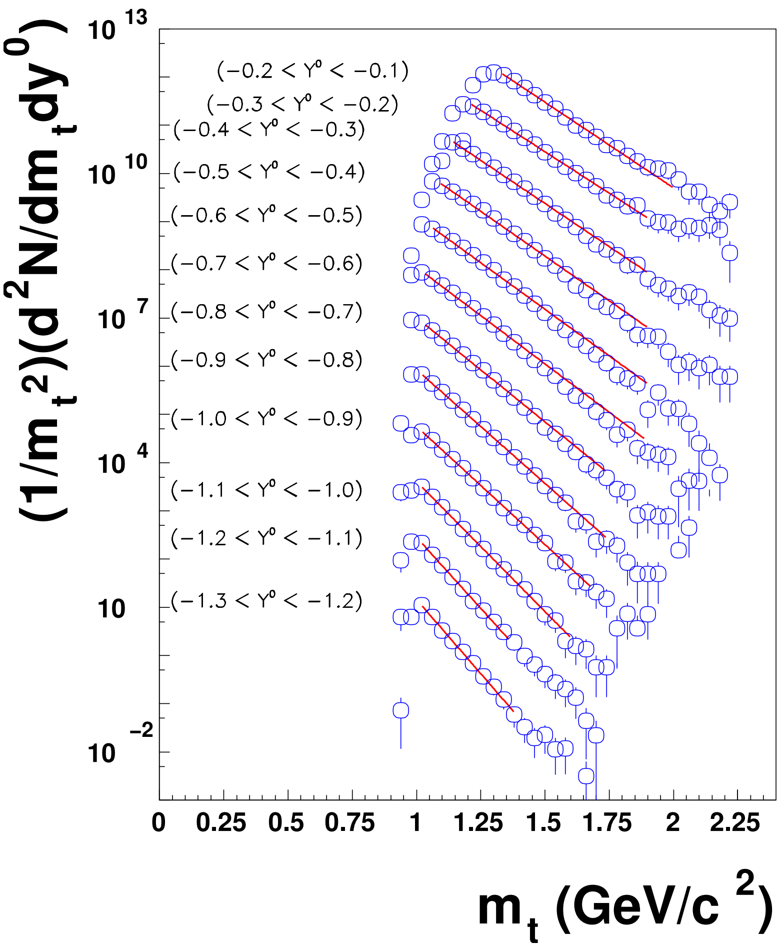

Figure 4.3: m_t*-spectra for protons in central Ru+Ru at 1.52 AGeV collisions for different rapidity bins between -1.3 and -0.1. The lines correspond to the fit with a Boltzmann-type function.*

The loss of very low transverse momentum particles, especially visible close to mid-rapidity, is due to the angular acceptance of the CDC. The presence of flow translates into a shoulder-arm behavior at low transverse momenta as already mentioned above.

This can not be measured with the CDC/BARREL sub-detector. For the extrapolation of the data to low momenta, the assumption is made that the spectra can be fitted with a single exponential function. Neglecting the flow component introduces a systematic error in the estimate of the yield. It has been checked that this error is small using RBUU events. This study is described in section 4.3.3.

The inverse slope parameter is directly extracted from the fit and can be plotted as a function of the rapidity. For a thermally-equilibrated system, the slope is expected to rise toward mid-rapidity. The multiplicity density $\frac{\mathrm{dN}}{\mathrm{dY}^0}$ is then obtained by extrapolating and integrating the exponential fit to the double differential yields from m_0 to ∞. This integral can be expressed in the following closed form:

$$\frac{\mathrm{dN}}{\mathrm{dY}^0} = \mathrm{AT_B^3 exp}\left(\frac{-\mathrm{m}_0}{\mathrm{T_B}}\right)\left(\frac{\mathrm{m}_0^2}{\mathrm{T_B^2}} + 2\frac{\mathrm{m}_0}{\mathrm{T_B}} + 2\right) \tag{4.4}$$

where A and $\mathrm{T_B}$ are the previously mentioned fit parameters and m_0 the nominal mass of the particle under consideration.

The behavior of K^+ $\mathrm{m_t}$-spectra as a function of the rapidity has been investigated in Ru+Ru collisions at 1.52 and 1.69 AGeV. Figure 4.4 shows the results for four rapidity bins between -1.3 and -0.5. For a better readability, the spectra have been multiplied by 10^{n} with n=0 for the first rapidity bin and n=3 for the last one. The spectra have been corrected for particle loss due to their decay in flight, tracking, matching and cut efficiencies. The background has been subtracted using the method described in section 2.2.4. The error bars represent statistical error. The result of the fit using the function 4.3 is shown by the straight lines.

It seems that the slope of K^+ $\mathrm{m_t}$-spectra depends on the beam energy. It is indeed slightly higher for the highest energy. This feature, discussed in more detail in the following section, is already present in the data before efficiency corrections. This rules out an eventual artifact of the corrections.

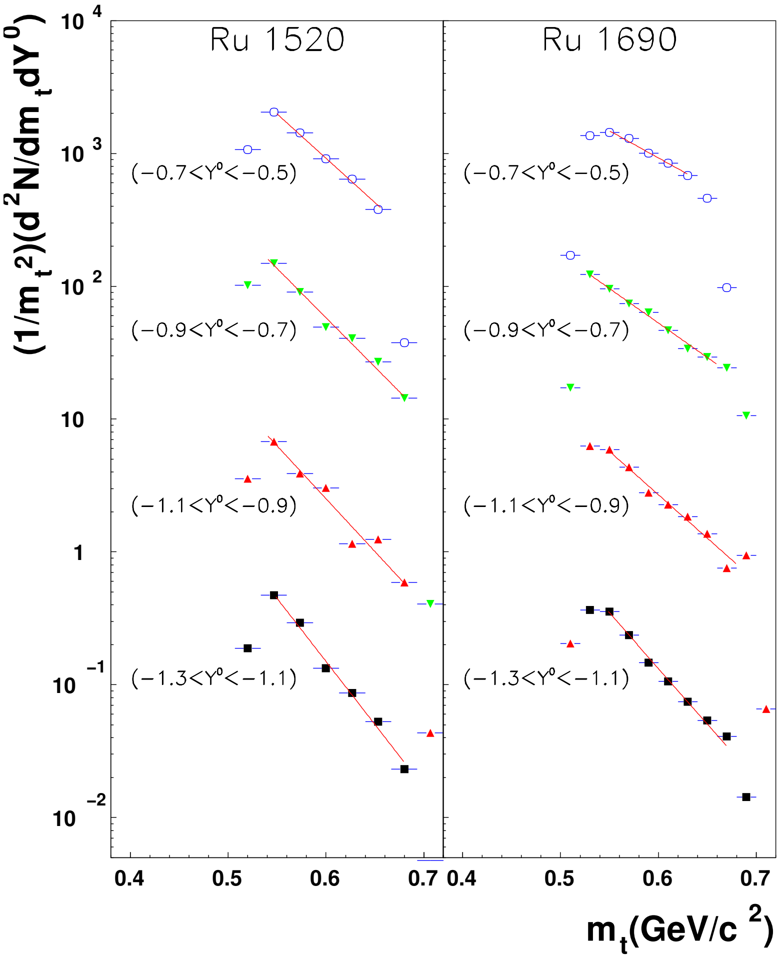

Figure 4.4: m_t*-spectra for kaons in central Ru+Ru collisions at 1.52 and 1.69 AGeV for four rapidity bins between -1.3 and -0.5. The lines correspond to the fit with a Boltzmann-type function.*

4.3.2 Apparent temperatures

The results of the fit using the Boltzmann function are plotted in Figure 4.5 for K^+ and in Figure 4.6 for protons. The inverse slope parameter is plotted as a function of the normalized rapidity on the left panel of Figure 4.5 for K^+ in the Ru system at 1.52 AGeV and 1.69 AGeV and of Figure 4.6 for protons in Ca+Ca at 1.49 AGeV, Ru+Ru at 1.52 AGeV and 1.69 AGeV and Au+Au at 1.49 AGeV. Since the four systems under investigation are symmetric, it is possible to reflect the data points measured in the backward hemisphere around mid-rapidity. The error bars correspond to the statistical and systematic errors. The lines correspond to the results of the isotropic expansion model and are discussed in section 4.3.4.

For protons, the inverse slope parameter is the same for all systems under investigation. For kaons, the inverse slope parameter is larger for the higher energy, as already seen on the m_t-spectra.

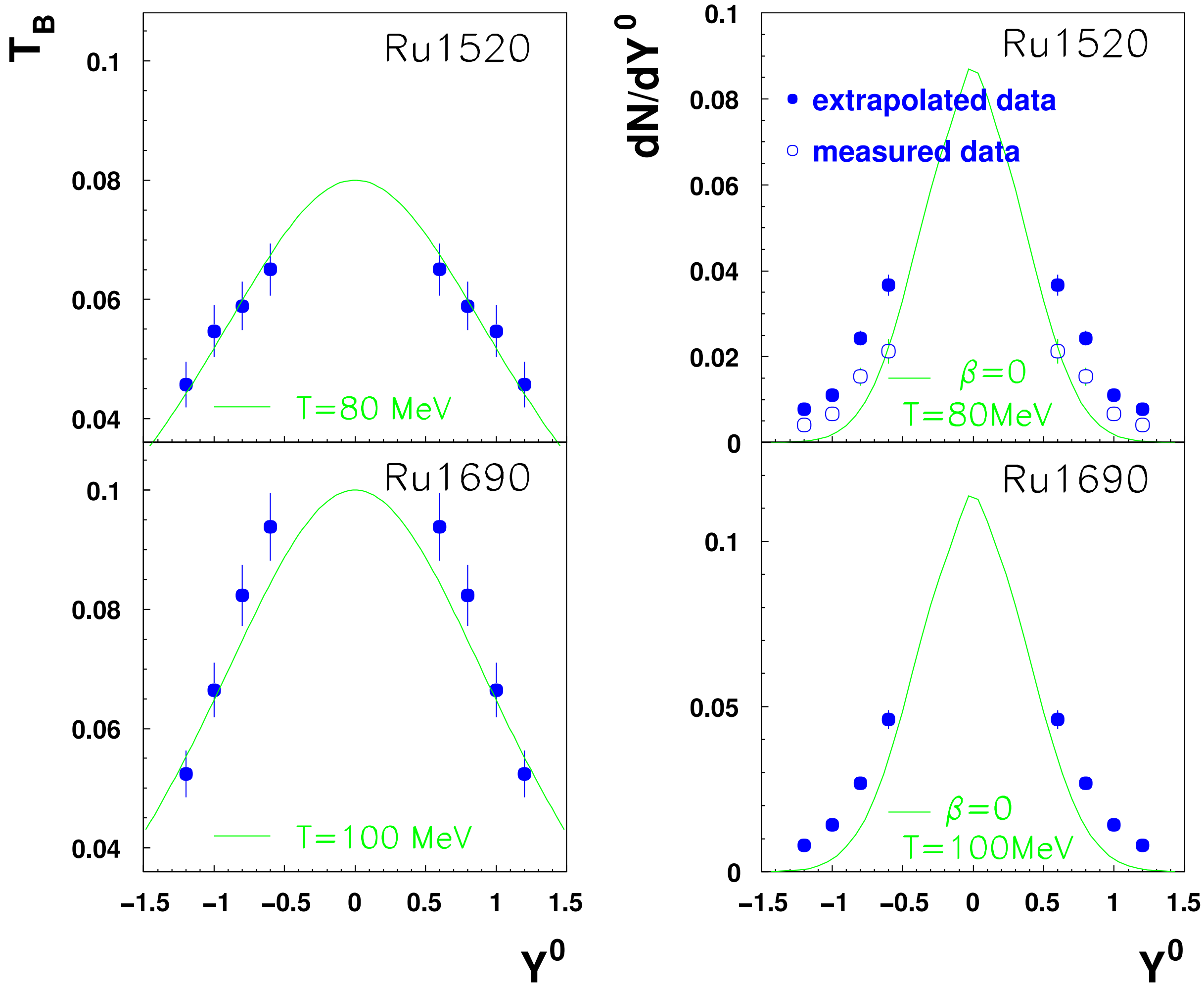

Figure 4.5: *Inverse slope parameter as a function of the normalized rapidity (left panel) and rapidity distributions (right panel) for kaons in Ru+Ru at 1.52 AGeV and 1.69 AGeV. The full dots are the results obtained from the extrapolation of m_t-spectra from m_0 to ∞ and the open dots correspond to the data measured in the CDC/BARREL acceptance without extrapolation. The lines are the results of the isotropic expansion model for a temperature of 80 (100) MeV in Ru+Ru collisions at 1.52 (1.69) AGeV and with β = 0.*

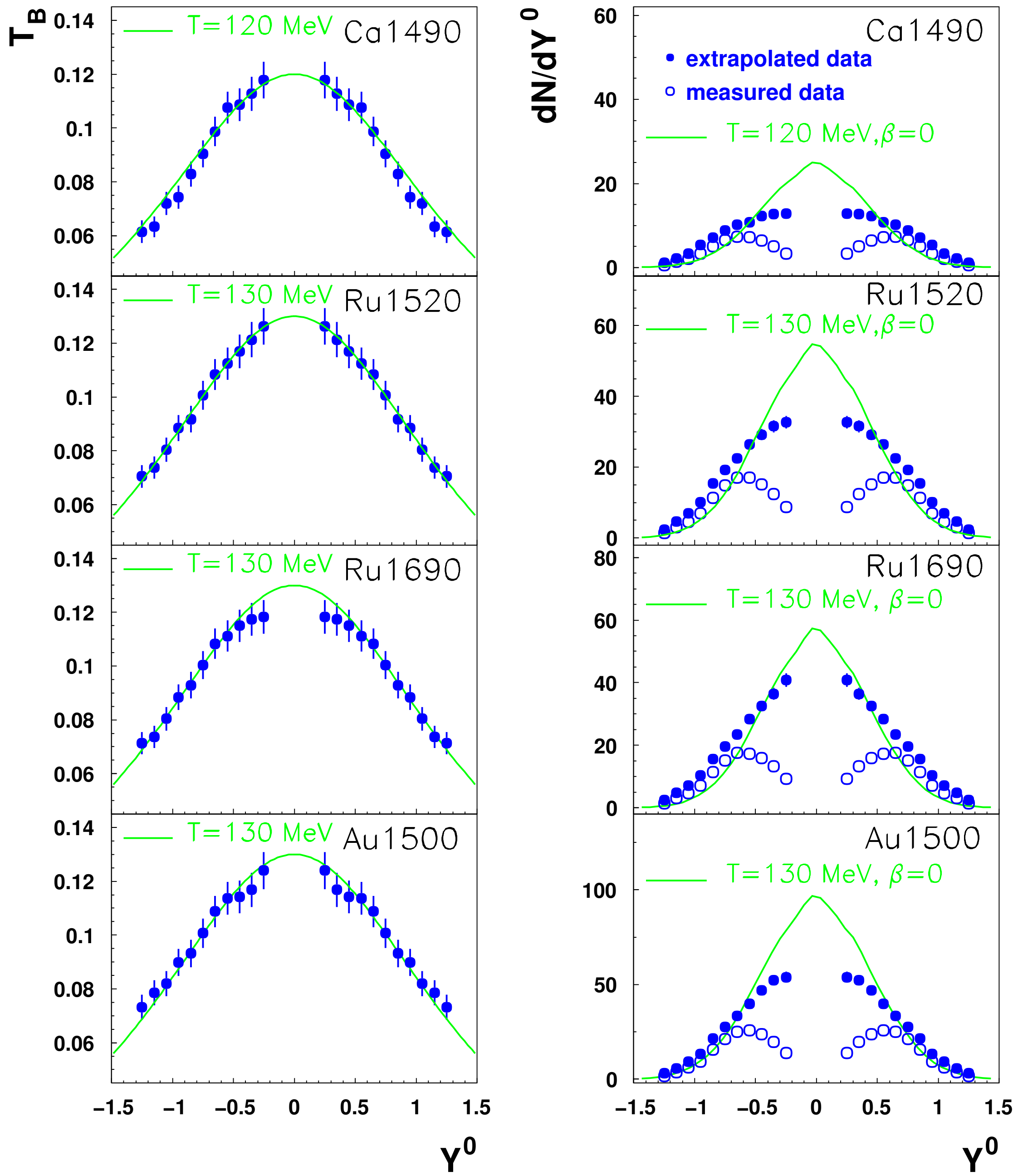

Figure 4.6: *Inverse slope parameter as a function of the normalized rapidity (left panel) and rapidity distributions (right panel) for protons in Ca+Ca at 1.49 AGeV, Ru+Ru at 1.52 AGeV, Ru+Ru at 1.69 AGeV and Au+Au at 1.49 AGeV. The full dots are the results obtained from the extrapolation of* m_t*-spectra from* m_0 *to* ∞ *and the open dots correspond to the data measured in the CDC/BARREL acceptance without extrapolation. The lines are the results of the isotropic expansion model for a temperature of 120 MeV for the Ca system and of 130 MeV for the other systems, with* $\beta = 0$*.*

4.3.3 Rapidity distributions

The rapidity distributions are presented in the right panels of Figure 4.5 for kaons in Ru+Ru collisions and of Figure 4.6 for protons in the four systems. The lines are discussed in section 4.3.4. The full dots show the results obtained after extrapolation of the m_t-spectra from m_0 to ∞ whereas the open dots show the results measured in the CDC/BARREL acceptance. In the target rapidity region, only a small part of the spectrum has to be extrapolated. Closer to mid-rapidity, the acceptance is limited by the angular range covered by the central part of the FOPI detector which makes the measurement of low momentum particles at small rapidity impossible. For this reason, the extrapolation of the spectra becomes important.

The validity of this extrapolation has been checked using a sample of events generated with the RBUU model. The simulated rapidity distributions are compared to the rapidity distributions obtained after using a filter which describes to the CDC/BARREL acceptance. The filtered data are then analysed in the same way as the experimental data, by extrapolating the spectra to the low momentum region.

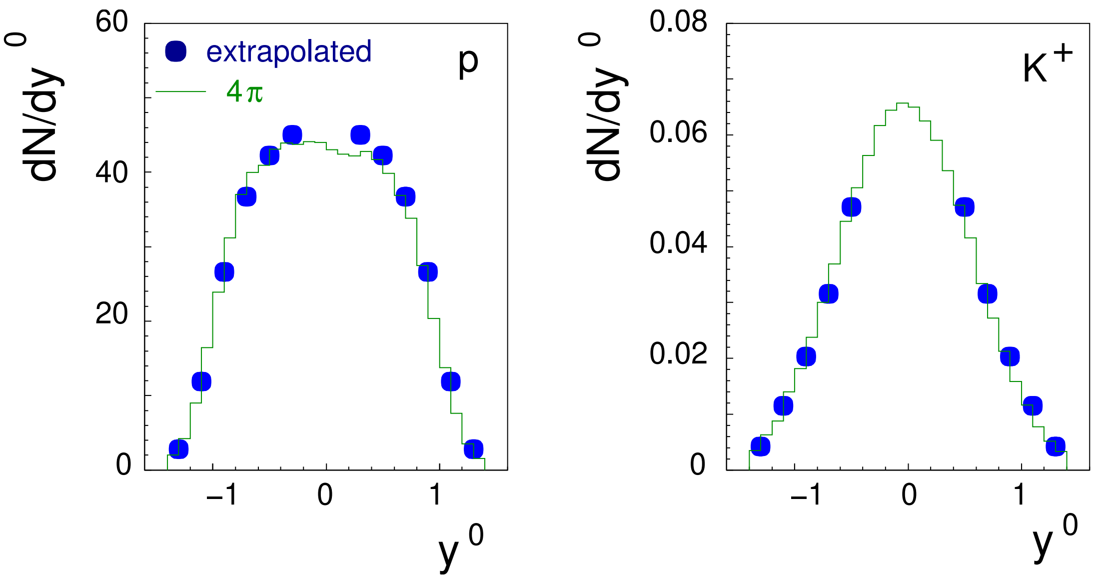

Figure 4.7: *Rapidity distributions for protons (left panel) and kaons (right panel) in Ru+Ru collisions at 1.52 AGeV as predicted by RBUU transport code. The full line corresponds to the initial distribution and the dots to the extrapolated data after the filter for the CDC/BARREL acceptance.*

The results are presented in Figure 4.7 for protons (left panel) and kaons (right panel) in Ru+Ru collisions at 1.52 AeV. The 4π distribution is shown by the full line and the dots correspond to the filtered and extrapolated data. The agreement between the original and the extrapolated distributions is very good. Under the assumption that the RBUU model is correctly describing real data, this means that the systematic error due to the extrapolation with a single exponential function (without any flow component) is not significant.

As can be seen from Figure 4.5, the inverse slope parameter for K^+ identified at 1.52 AGeV is lower than for the K^+ identified at 1.69 AGeV, whereas the yields are very similar for the two energies. The intuitive expectations would rather suggest that the kinematics should be the same since the difference in beam energy is only around 200 MeV but that the yields should differ with respect to the free NN-threshold. Indeed, at 1.52 AGeV beam energy, K^+ are produced subthreshold whereas they are produced above threshold for a beam energy of 1.69 AGeV, although the difference should not be very large.
Although the results obtained for protons in these two systems are similar, the difference observed in the kaons could however be attributed to the calibration of the data or to detector bias. The measurement of kaon production in Ru+Ru collisions at 1.3 and 1.9 AGeV for instance would allow to investigate the excitation function for Ru+Ru collisions and to answer the question whether or not the difference observed in the present data is due to the physics or to a systematic inconsistency in the experiment.

4.3.4 Thermally equilibrated expanding source

As explained in section 4.2.1, the inverse slope parameter T_B is obtained by fitting a Boltzmann-function to the m_t-spectra in narrow rapidity windows. If the system is thermally equilibrated, the Boltzmann temperature T_B is expected to vary with rapidity in the following way:

$$T_B(Y) = \frac{T}{\cosh(Y)} \tag{4.5}$$

The solid lines in Figure 4.5 and Figure 4.6 are the results of the Boltzmann temperature dependence on the rapidity as described by equation 4.5. The protons are well described with a temperature of 120 MeV for the Ca system and of 130 MeV for the other systems. The inverse slope parameter of K^+ in Ru+Ru collisions at 1.52 AGeV can be described with a temperature of 80 MeV whereas a temperature of 100 MeV is needed to reproduce the K^+ inverse slope parameter at 1.69 AGeV. This reflects the fact that the K^+ m_t-spectra are steeper at 1.52 AGeV than at 1.69 AGeV as already mentioned. It is not clear for the moment why the temperature at 1.69 AGeV is higher than at 1.52 AGeV while the yields remain the same.

For the rapidity distributions, the results are presented for an expanding source without collective radial flow and with the temperatures mentioned above. Both for protons and kaons, the measured rapidity distributions are broader than what is expected for a thermally expanding system. This is an indication that the expansion is not isotropic. The kaon anisotropy may be due to primary processes at the origin of kaon production. However, since the protons are measured simultaneously and also show this anisotropy, the conclusion can be drawn that the whole system is elongated and kaon anisotropy may originate from collective effects.

4.4 Dependence of the kaon production on the system size

The production of kaons is connected to the properties of the medium in which they are produced and strongly depends on the density reached in the fireball, as explained in the introduction. It is possible to investigate the kaon production as a function of the density by varying the system size for a given beam energy. The number of K^+ per participant is investigated as a function of the number of participants in the reactions Ca+Ca at 1.49 AGeV, Ru+Ru at 1.52 AGeV and Au+Au at 1.49 AGeV.

4.4.1 Number of K^+ as a function of A_{part}

The number of kaons identified in Ca+Ca and Au+Au reactions is too small to allow for an extrapolation of the m_t-spectra. For this reason, the dependence of kaon production on the system size has to be investigated in the CDC/BARREL acceptance only. Since an upper momentum cut of 0.4 GeV/c has to be used for the kaon identification in

the Au system, this cut is also applied in the other systems. This allows to select the same acceptance in each case. Since the beam energy is not exactly the same for each system, it is necessary to correct for this difference and all the results have been scaled to 1.5 AGeV using the following procedure.
The KaoS collaboration has measured the excitation function of K^+ production for C and Au systems [Stu 00]. It has been shown that the kaon production scales with the beam energy as E^α. The value of α is 4.4 in C+C collisions and 6 in Au+Au collisions. An excitation function for kaon production in Ni+Ni collisions is also available in [Bes 97] and the value of α is 5.3 for this system. An intermediate value of 5.5 is taken for Ru+Ru collisions. The relation between the kaon production and the beam energy allows to scale the data and compare each system at the same energy.

The number of K^+ per participant as a function of the number of participants is plotted in Figure 4.8 for a beam energy of 1.5 AGeV. These results are compared to theoretical predictions in the next chapter.

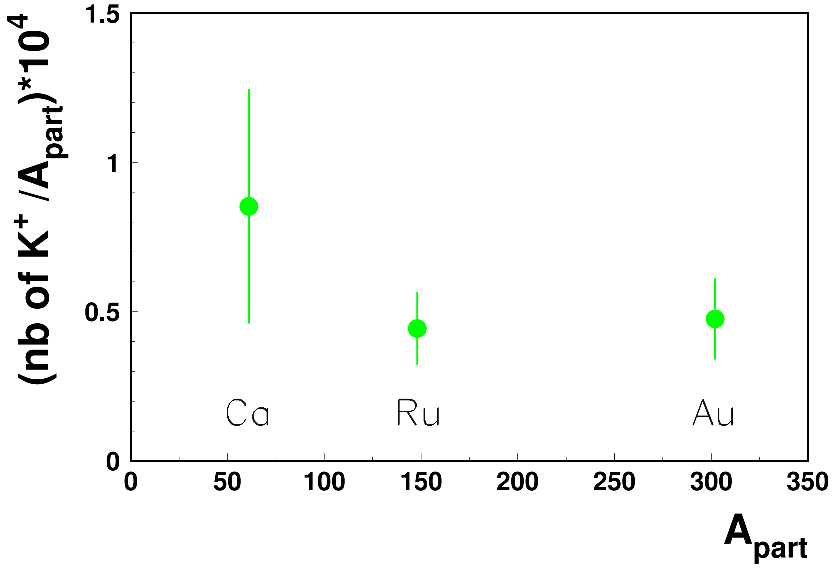

Figure 4.8: *Number of* K^+ *per participant as a function of the average number of participants in Ca+Ca, Ru+Ru and Au+Au collisions at 1.5 AGeV beam energy. The kaons have been identified in the CDC/BARREL acceptance with an upper momentum cut of 0.4 GeV/c. The values are corrected for efficiencies and background contamination. The error bars correspond to the statistical and systematic errors.*

The values for the number of produced kaons are corrected for the tracking, matching and cut efficiencies, for the loss due to the decay in flight and for the background contribution. The error bars include the statistical and systematic errors. The large error bar for the Ca point is due to the very low statistics. Only 20 K$^+$ are identified in this system for the selected centrality and under the chosen momentum cut. It makes it difficult to include this point in the systematic in a reliable way. The difference between the Ru and the Au systems is very small. Within error bars, it is compatible with the idea that there is no system size effects. This result is discussed and compared to the KaoS measurements in the next section.

Two aspects which could influence the kaon production are described.
As can be seen from the rapidity distributions, the emission of K$^+$ is not isotropic. For this reason, it is important to check that the trend seen in the data is not biased by the acceptance of the FOPI detector for kaon identification.

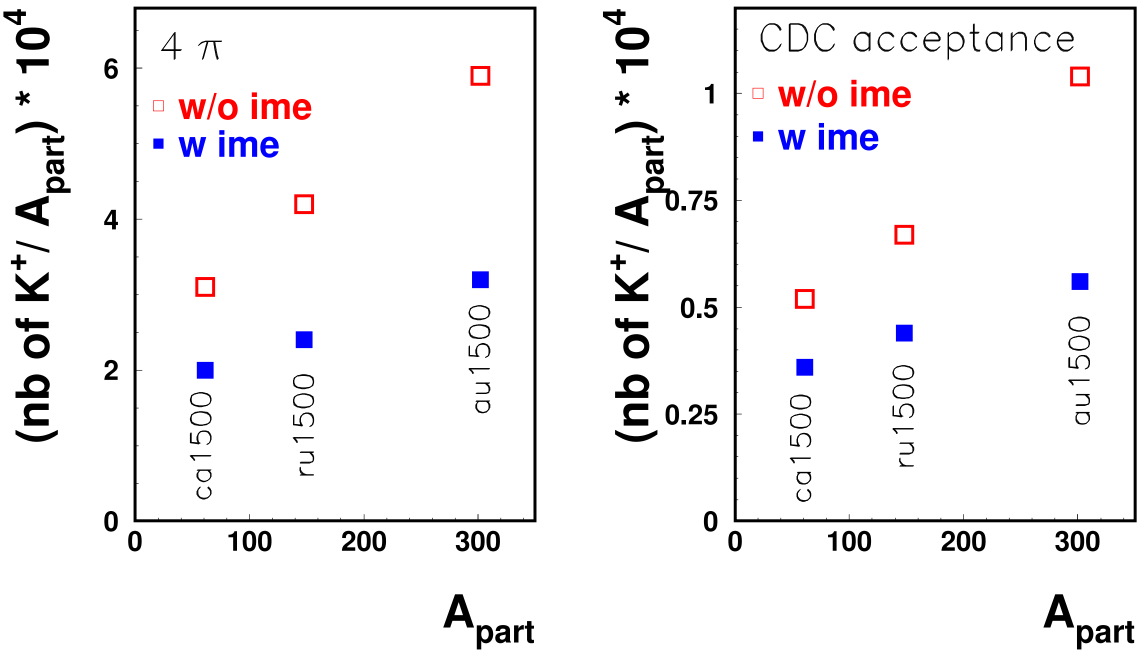

Figure 4.9: *K^+ production probability as a function of the number of participants as predicted by RBUU calculations in the full phase space (left panel) and in the CDC/BARREL acceptance (right panel). The open (full) symbols correspond to the version of the calculation without (with) in-medium modification of the kaon mass.*

For that purpose, the predictions of RBUU transport code are used [Cas 99]. The number of K^+ per participant as a function of the number of participants has been extracted in Ca+Ca, Ru+Ru and Au+Au reactions at 1.5 AGeV in the full solid angle and in the CDC/BARREL acceptance.
The results are presented in Figure 4.9. The left panel shows the dependence of the kaon production on the system size in 4π and the right panel corresponds to the CDC/BARREL acceptance. The trend of the data remains the same when going from the full phase space to the CDC/BARREL acceptance. This is a hint that the acceptance of the FOPI detector for kaon identification does not influence the message conveyed by the data, provided the RBUU model describes the experimental data in a reasonable way.

The influence of the isospin on the kaon production is not well known. The number of neutrons in a Au nucleus is larger than the number of protons. Thus, the production of K^0, involving neutrons, should be favored compared to the production of K^+ [Aic 00]. This is not the case in the Ca system since a ^{40}Ca nucleus contains as many protons as neutrons. However, the magnitude of this effect is most probably very small and should not be responsible for the apparently reduced kaon production in Au+Au collisions as compared to Ru+Ru collisions.

Comparison to KaoS data

It is interesting to compare the results measured with the FOPI detector to the results obtained by the KaoS collaboration. The K^+ production in Au+Au collisions at 1.46 AGeV [Stu 00] has been investigated. The comparison is not straight forward because the acceptance of both detectors is not the same. Furthermore, the KaoS results are measured for inclusive reactions whereas the FOPI kaons are identified in central events. However an attempt has been made for the results obtained in Au+Au collisions at 1.5 AGeV.

To be able to compare FOPI and KaoS results, it is necessary to extrapolate the data to the full phase space. The KaoS data are extrapolated to 4π taking into account the anisotropy measured by the KaoS collaboration. Unfortunately, the anisotropy has not

been measured for central Au+Au collisions yet. The KaoS collaboration has shown that the anisotropy for central Ni+Ni collisions is smaller than for inclusive Ni+Ni collisions and that the anisotropy in inclusive Au+Au collisions is smaller than in inclusive Ni+Ni collisions. These observations lead to the conclusion that the anisotropy in central Au+Au collisions is probably rather small. Thus the FOPI data are extrapolated isotropically to the full solid angle. The uncertainty introduced by this method is estimated to be around 30% and is taken into account in the error bars.
The portion of phase space covered by the CDC has been estimated using RBUU events. The number of kaons produced in 4π has been compared to the number of kaons identified in the CDC/BARREL acceptance when a filter is applied to the RBUU data. It has been found that the CDC/BARREL subsystem covers 13% of the full solid angle. This method should give a reasonable approximation of the CDC acceptance since the calculations can reproduce the shape and the magnitude of the K^+ rapidity distributions.

Since the Au+Au data from KaoS at 1.46 AGeV are inclusive, they have to be normalized to the number of participants. For that purpose, the Au+Au collisions at 1.0 AGeV are used. At this energy, the KaoS collaboration has measured not only inclusive cross sections but also the dependence on centrality. The ratio between the central and the inclusive K^+ multiplicities is 4, the central collisions corresponding to $< A_{part} >= 275$. This value is used to estimate the kaon multiplicity in central Au+Au collisions at 1.46 AGeV from the measured inclusive multiplicity at this energy.

In this work, the K^+ multiplicity has been estimated in Au+Au collisions at 1.49 AGeV for a centrality selection corresponding to $< A_{part} >= 302$. After scaling the energies to 1.5 AGeV in both cases, the K^+ production probability extracted from the FOPI data is 0.12 ± 0.06 K^+ and the value extracted from the KaoS data is 0.189 ± 0.022 K^+. The errors take into account the approximation for the anisotropy and for the estimate of $< A_{part} >$.
This comparison is based on several assumptions on the extrapolation to the full phase space for the FOPI data and for the estimate of the number of participants. Within error bars, the FOPI results for Au+Au collisions at 1.5 AGeV do not contradict the results obtained by the KaoS collaboration. Taking into account the experimental difficulties

this result is encouraging. However the trend observed when comparing different systems is not the same for both experiments. The KaoS collaboration has evidenced a strong increase of the kaon production probability with the system size whereas the difference between Ru+Ru and Au+Au collisions at 1.5 AGeV measured by the FOPI collaboration is rather small. This needs further investigation.

4.4.2 Systematics of strange particle production

The FOPI measurements can also be included in the systematics of strange particle production proposed by V. Metag [Met 93]. This aims at comparing the production probability normalized to the number of participants in different systems as a function of the incident energy above the Coulomb barrier normalized to the threshold energy necessary to produce a certain particle in a NN-collision. This representation allows to compare data from several experiments, measured within different acceptances, for different centrality classes and at different beam energies.

For a meaningful comparison, the data have to be extrapolated to the full solid angle. This was done using the method described above. The systematics of strange particle production is shown in Figure 4.10 with the FOPI points obtained in this analysis. The Ru+Ru systems are represented by the open circles, the Au+Au system by the open square and the Ca+Ca system by the full circle. The other data are taken from [Her 96] and references therein. Within error bars, the results of the present analysis fit nicely into the systematics.

The extrapolation to 4π is made under the assumption that the emission of strange particles is isotropic. Furthermore, in order to be able to compare data measured with different centrality selection, the assumption has to be made that the dependence of strange particle production on the number of participants $A_{\rm part}$ increases linearly with $A_{\rm part}$, otherwise it is not possible to compare data measured for different number of participants. This last assumption is questionable. For this reason this systematic comparison of particle production has to be taken with caution.

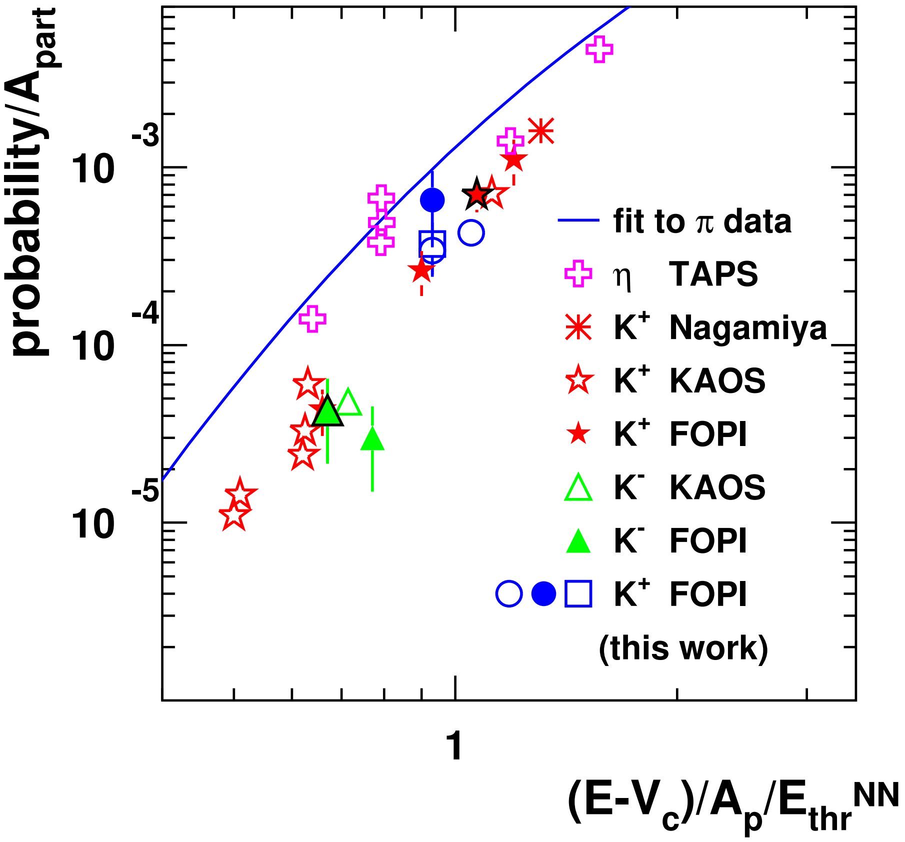

Figure 4.10: *Production probability of strange particles as a function of the incident energy above the Coulomb barrier normalized to the threshold energy necessary to produce a certain particle in NN-collisions. The data are extrapolated to the full solid angle. The FOPI measurements presented in this work are shown by the open circles for Ru+Ru collisions, by the open square for Au+Au collisions and by the full circle for Ca+Ca collisions.*

4.5 Summary

In this chapter, results on kaon production have been presented. The K^+ rapidity distributions have been measured in Ru+Ru collisions at 1.52 and 1.69 AGeV. Although the yields are very similar for both energies, the inverse slope parameter is larger for the higher energy. This feature is difficult to understand within the actual knowledge on kaon production. Furthermore, it can not be excluded that the experimental data are influenced by any detector bias, although the results on protons do not show any systematic deviation at the two considered energies.

The number of K^+ per participant has been measured as a function of the system size. It appears that the difference between Ru+Ru and Au+Au collisions is very small. The kaon multiplicity measured in central Au+Au collisions by the FOPI collaboration is in agreement with the result obtained by the KaoS collaboration.

Chapter 5

Comparison of the experimental results to the theoretical predictions

In parallel to the experimental effort to understand the properties of nuclear matter, theoretical models are being developed to bring new insights and a deeper understanding on the complex physics of heavy ion collisions. Among the many models available to describe heavy ion collisions, two transport calculations are selected to compare the results of this analysis to theoretical predictions: the Boltzmann-Uehling-Uhlenbeck (BUU) type and the Quantum Molecular Dynamics (QMD) type.

5.1 Description of the models

5.1.1 BUU model

In the models of type BUU [Ber 88, Cas 90, Cas 99], the reaction mechanisms are dominated by the mean field approximation at low energy and by the nucleon-nucleon interaction at higher energy. Each nucleon is considered as a point-like particle and is represented by test particles which are propagated through the phase space. This model does not produce composite particles.

The main kaon production channels considered in this model are the following:

$$\mathrm{NN} \rightarrow \mathrm{NK^+Y}, \qquad \Delta\mathrm{N} \rightarrow \mathrm{NK^+Y}, \qquad \mathrm{NN} \rightarrow \mathrm{NNK^+K^-}$$

$$\Delta\Delta \to \mathrm{NK^+Y}$$

$$\pi\mathrm{N} \to \mathrm{K^+Y}, \qquad \pi\mathrm{N} \to \mathrm{NK^-K^{+,0}}, \qquad \pi\mathrm{Y} \to \mathrm{NK^-}$$

where Y stands for Λ or Σ hyperons.

The dependence of the production cross section on the energy above threshold is parametrized using the experimental data on elementary processes. The energy above threshold is defined by $\sqrt{s} - \sqrt{s_0}$ where $\sqrt{s}$ is the energy in the center of momentum reference frame of the colliding particles and $\sqrt{s_0}$ is the threshold energy for a given process. The kaon production is treated perturbatively [Cas 97, Cas 99].

The calculations are available in two versions. The first one does not include any in-medium modification of the kaon mass. The bare mass is used for all the densities. The other version takes into account the dependence of the kaon mass on density as described in the introduction in Figure 1.3. In this case, the K^+ mass increases with the density whereas the K^- mass decreases.
The calculations used in this work were performed by E.Bratkovskaya and W. Cassing [Cas 00].

5.1.2 QMD model

QMD-type models [Stö 86, Pei 89, Aic 91, Har 92] are a powerful tool to describe most of the processes in heavy ion collisions. The nucleons are represented by gaussian wave-packets. Classical equations of motion are used to propagate their centroids in an interaction potential. This potential contains a Coulomb term, a Yukawa term, a local term and a term which takes into account the momentum dependence of the interaction. The local term is parametrized with a potential depending on the density. This allows a direct connection to the equation of state of nuclear matter.
The reactions are treated as binary collisions between nucleons, taking into account the Pauli exclusion principle. The fragments are produced by coalescence. The calculations are done event by event.
Several versions of the model have been developed. The IQMD version (Isospin Quantum Molecular Dynamics) is used in this work. It distinguishes neutrons and protons and

treats the production, the propagation and the absorption of π via Δ resonances.
This model also provides calculations including in-medium effects and calculations with the kaon bare mass. Furthermore, two parameterization for the equation of state are used corresponding to a soft EOS (k=200 MeV) and to a hard EOS (k=380 MeV).
The results reported in this work were provided by Ch. Hartnack and J. Aichelin [Aic 00].

5.2 Comparison of the data to the predictions of the RBUU model

5.2.1 Proton and kaon yields: rapidity distributions

In this section, the predictions of the RBUU model for proton and kaon production are presented. In order to compare the model prediction to the experimental data, a filter is used to describe the CDC/BARREL acceptance. Once the filter has been applied, the RBUU data are analysed in the very same way as the experimental data. The transverse mass spectra are fitted with a Boltzmann function and extrapolated to low momenta. The fit parameters allow to extract the rapidity distributions for protons and kaons in all the systems under consideration in this work.

Figures 5.2 and 5.3 summarize the results for kaons and protons, respectively. The experimental inverse slope parameters and rapidity distributions are compared to the model predictions. The dots correspond to the data and the curves to the results of the calculation. For K^+, the dashed line shows the prediction when the kaon bare mass is used and the full line corresponds to the version of the calculation including in-medium modification of the kaon mass.

Since the ratio $\frac{\pi^+}{\pi^-}$ is not reproduced by the model, the number of protons is artificially scaled to conserve the charge. Furthermore, the coalescence of protons to d, t, He, α and heavier particles is not taken into account. As a consequence, the total number of protons found in the calculations is not equal to the initial number of protons in the collisions [Cas 00]. For this reason, the RBUU histograms are scaled in a way that the integral of the rapidity distribution corresponds to the number of protons identified in the experiment. In the case of kaons, the yields predicted by the model and presented in [Cas 99] have to be scaled by a factor 1.6. This allows to compensate for a wrong cross section involving Δ resonances in the calculation [Cas 00].

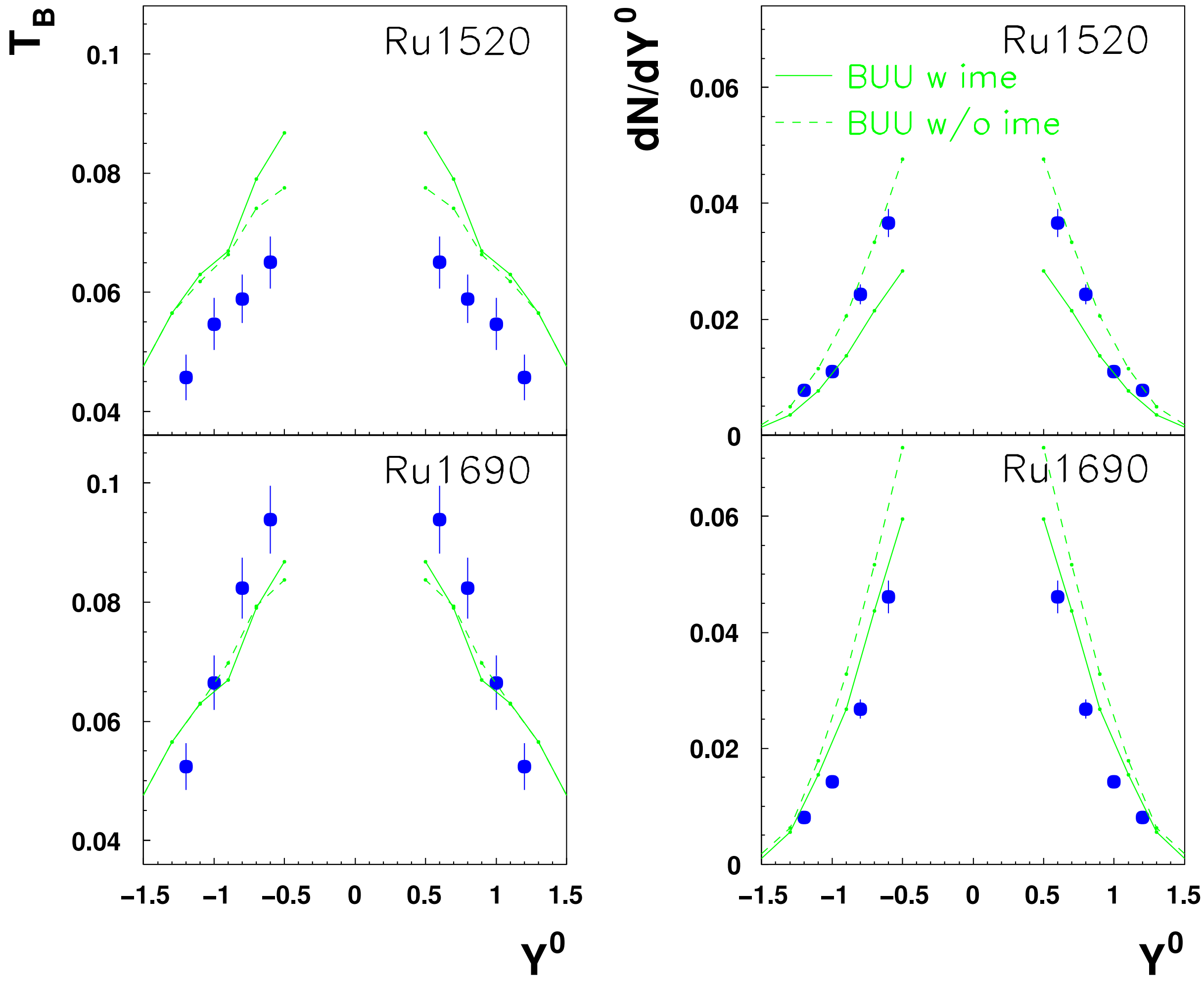

Figure 5.1: *Inverse slope parameter (left panel) and rapidity distributions (right panel) for K^+ in Ru+Ru at 1.52 and 1.69 AGeV. The measured data are represented by the full dots. The lines show the RBUU predictions. The version without (with) in-medium effects is represented by the dashed (full) line.*

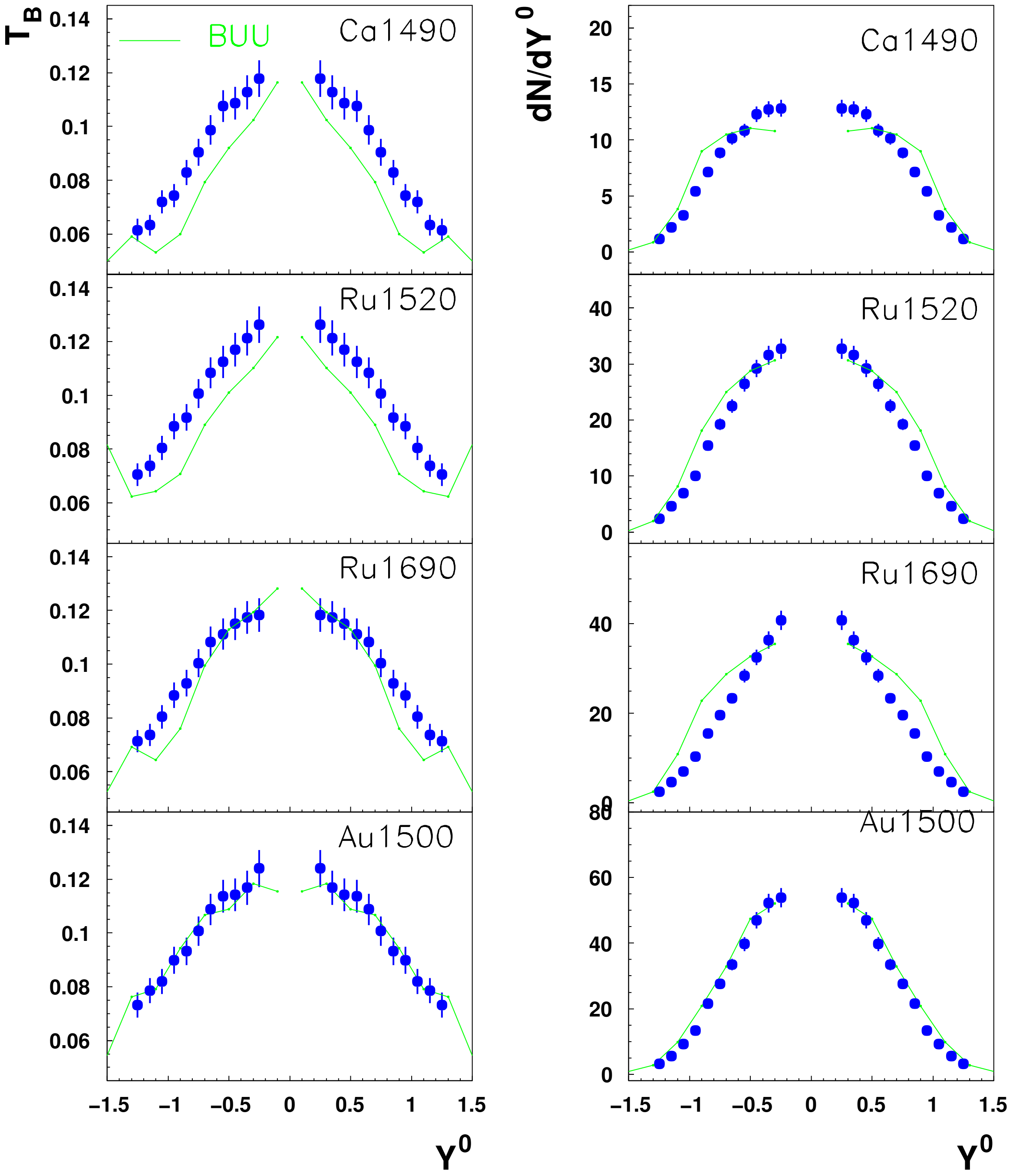

Figure 5.2: *Inverse slope parameter (left panel) and rapidity distributions (right panel) for protons in Ca+Ca, Ru+Ru and Au+Au at 1.5 AGeV and in Ru+Ru at 1.69 AGeV. The measured data are represented by the full dots. The lines show the RBUU predictions.*

The proton inverse slope parameters are quite well reproduced by the model for Ru+Ru collisions at 1.69 AGeV and Au+Au collisions at 1.5 AGeV but are underestimated for the two other systems, although the shape is well described. After normalization of the proton rapidity distributions as explained above, the model seems to reproduce the shape of the measured rapidity distributions in Au+Au collisions at 1.49 AGeV. The agreement with the two other systems is not as good. The theoretical rapidity distributions are slightly wider than the measured distributions. This can be due to a too small stopping in the model.

For kaons, it is difficult to draw any conclusion regarding the in-medium modification of the masses. The difference between both versions is rather small in the rapidity domain measured with the FOPI detector. The inverse slope parameter is well reproduced by the model for Ru+Ru collisions at 1.69 AGeV but is overestimated at the lower energy. The shape of the rapidity distributions as well as the magnitude seem to be in agreement with the data. The version without in-medium modifications of kaon mass seems to reproduce better the data at 1.52 AGeV whereas the data at 1.69 AGeV seem to favor the version with in-medium effects. At this point of the analysis, neither assumption can really be ruled out. This shows the importance of identifying K^+ at mid-rapidity, where the in-medium effects are much more pronounced.

As described in chapter 2, it is possible to identify K^+ in the region of mid-rapidity using the HELITRON. Although some difficulties remain, an attempt has been made to combine HELITRON and CDC data measured in Ru+Ru collisions at 1.69 AGeV. For that purpose, the K^+ kinetic energy has been measured in both sub-detectors. The result is presented in Figure 5.3. The open dots show the data measured in the HELITRON in the polar angular range between 80° and 100° in the center of mass frame, corresponding to mid-rapidity and the full dots correspond to the data measured in the CDC in the polar angular range between 154° and 156°. Due to the acceptance of the two sub-detectors, it was not possible to identify kaons in the same angular range. The data are corrected for efficiencies and background contribution. The shaded area for the HELITRON points corresponds to an estimate of the error due to the different features found in the HELITRON data and described in chapter 2.

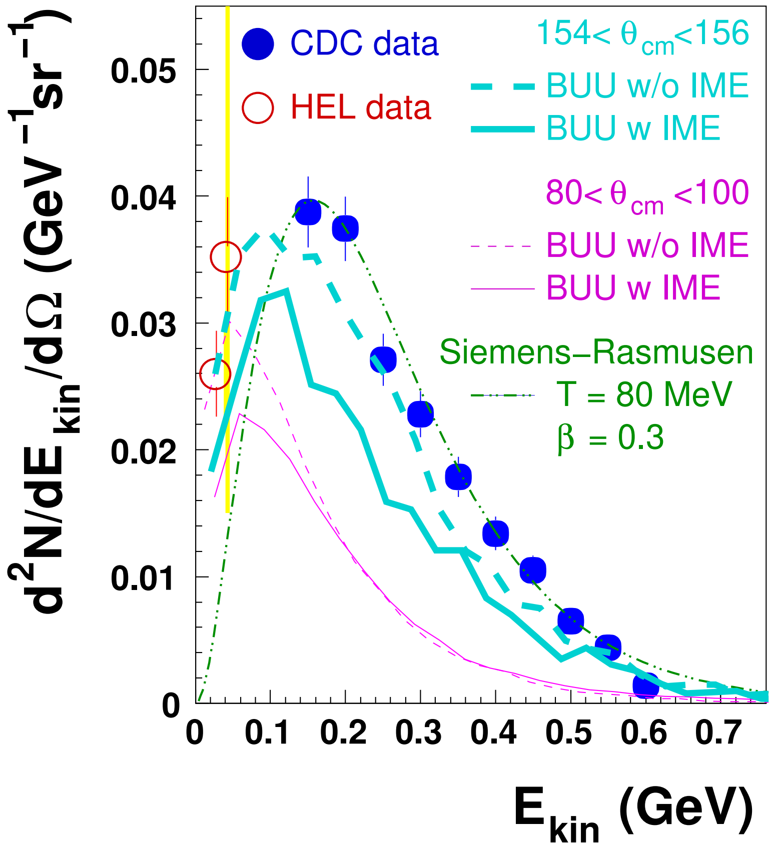

Figure 5.3: *Kinetic energy spectrum for K^+ in Ru+Ru collisions at 1.69 AGeV. The full dots show the CDC data measured in* $154^\circ < \theta_{cm} < 156^\circ$ *and the open dots show the HELITRON data measured in* $80^\circ < \theta_{cm} < 100^\circ$*. The dotted-dashed line corresponds to the expectation for an isotropically expanding source with a temperature T=80 MeV and a flow velocity β = 0.3. The other lines show the predictions of the RBUU-model. The full lines correspond to the version including in-medium modifications of hadron masses and the dashed lines to the version using the kaon bare mass. The thick lines are obtained for* $154^\circ < \theta_{cm} < 156^\circ$ *and the thin lines for* $80^\circ < \theta_{cm} < 100^\circ$*.*

The dotted-dashed line shows the expectation for an isotropically expanding source with a temperature of 80 MeV and a flow velocity of 0.3. This calculation seems to reproduce the CDC data but misses the points measured in the HELITRON. The other lines correspond to the predictions of the RBUU model. The dashed lines show the result of the calculation using the kaon bare mass and the full lines correspond to the calculation including in-medium modification of kaon mass. The CDC data have to be compared to the thick lines and the HELITRON data to the thin lines. The difference between the calculations in each angular range shows that the emission of K^+ is not isotropic. In both cases, the difference between the two model versions is the largest for low momenta, especially at mid-rapidity, which motivates the measurement of strangeness in this region. The actual HELITRON data are not precise enough to draw any conclusion for the moment. However, this first attempt to measure complete spectra with the FOPI detector is encouraging and with a careful investigation of HELITRON performances, this goal can be reached.

5.2.2 Number of K^+ as a function of A_{part}

The experimental dependence of the K^+ production on the system size presented in section 4.3.1 is compared to the predictions of the RBUU model. The results are presented in Figure 5.4.

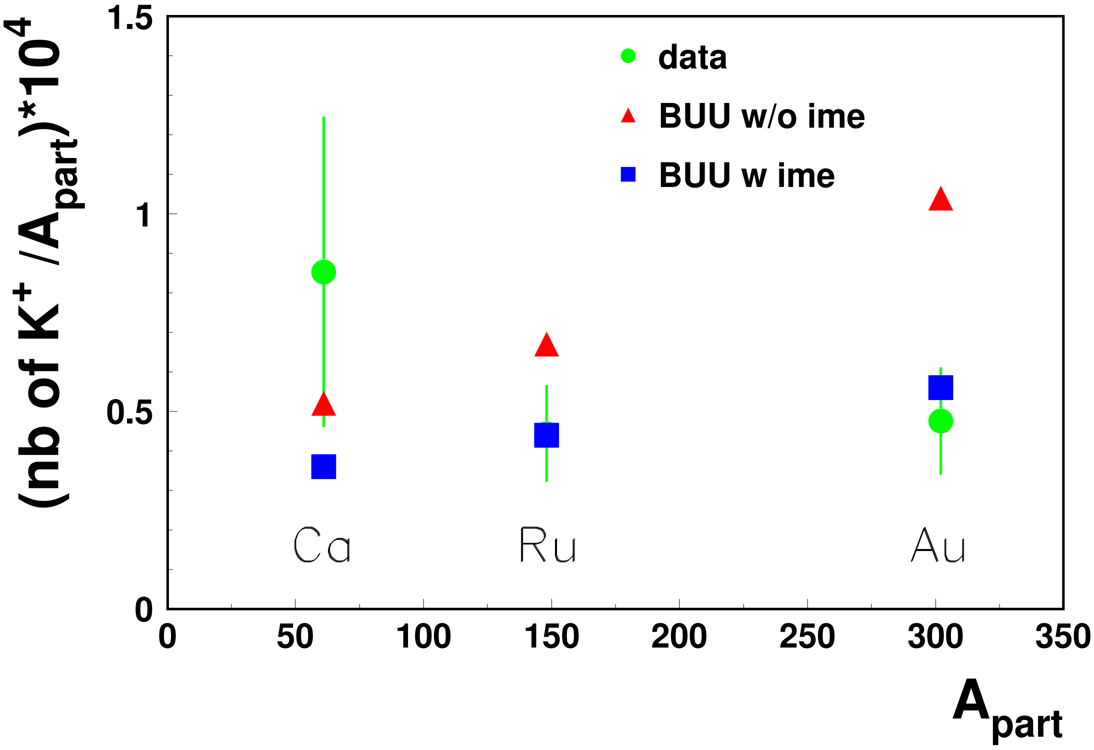

Figure 5.4: *Number of K^+ per participant as a function of the number of participants in Ca+Ca, Ru+Ru and Au+Au at 1.5 AGeV for central collisions. The experimental data, measured in the CDC/BARREL acceptance, are shown by the dots. The predictions of the RBUU model without (with) mass modification are shown by the triangles (squares).*

The experimental data are represented by the full dots. The RBUU predictions are plotted for the version of the calculation including the in-medium modification of kaon masses (squares) and for the version using the kaon bare mass (triangles). As expected, the K^+ production is lower when in-medium effects are including. Since the K^+ mass increases it becomes more difficult energetically to produce them. Although the Ca point is out of the systematic, the data favor the version of the calculation including in-medium effects.
It is interesting to note that the difference between the two versions of the calculation is the largest for the heaviest system. This emphasizes the idea that heavy systems are better suited to distinguish between the different assumptions.

5.3 Comparison of the data to the predictions of the IQMD model

The experimental data are also compared to the predictions of the IQMD model. Two different parameters can be varied in this type of model: the modification of hadron masses and the stiffness of the equation of sate. Both affect the yield of produced particles in a different way. For a soft equation of state, high densities can easily be reached because it is easier to compress the nuclear matter. In the case of a hard equation of state, it is more difficult to reach high densities. This implies that the number of kaons produced in heavy ion collisions should be higher if the equation of state of nuclear matter is soft [Aic 85]. However, for high density, the K^+ mass becomes larger than the bare mass which should lower the K^+ production. It is a delicate task to disentangle both effects.

The results of the comparison between experimental data and IQDM predictions are presented in Figure 5.5 which shows as before the number of K^+ per participant as a function of the number of participants. The full dots correspond to the experimental data. The triangles correspond to the results obtained when the kaon bare mass is used and the squares to the calculations including in-medium modifications of the kaon mass. The open (full) symbols show the predictions for a hard (soft) equation of state. In both cases, the momentum dependence is taken into account.

In all versions of the model, the trend is the same: the kaon production is increasing with the number of participants. The data seem to favor the version with in-medium effects. The accuracy of the data does not allow to draw definitive conclusions on the equation of state, although the hard equation version seems to be in better agreement with the data.

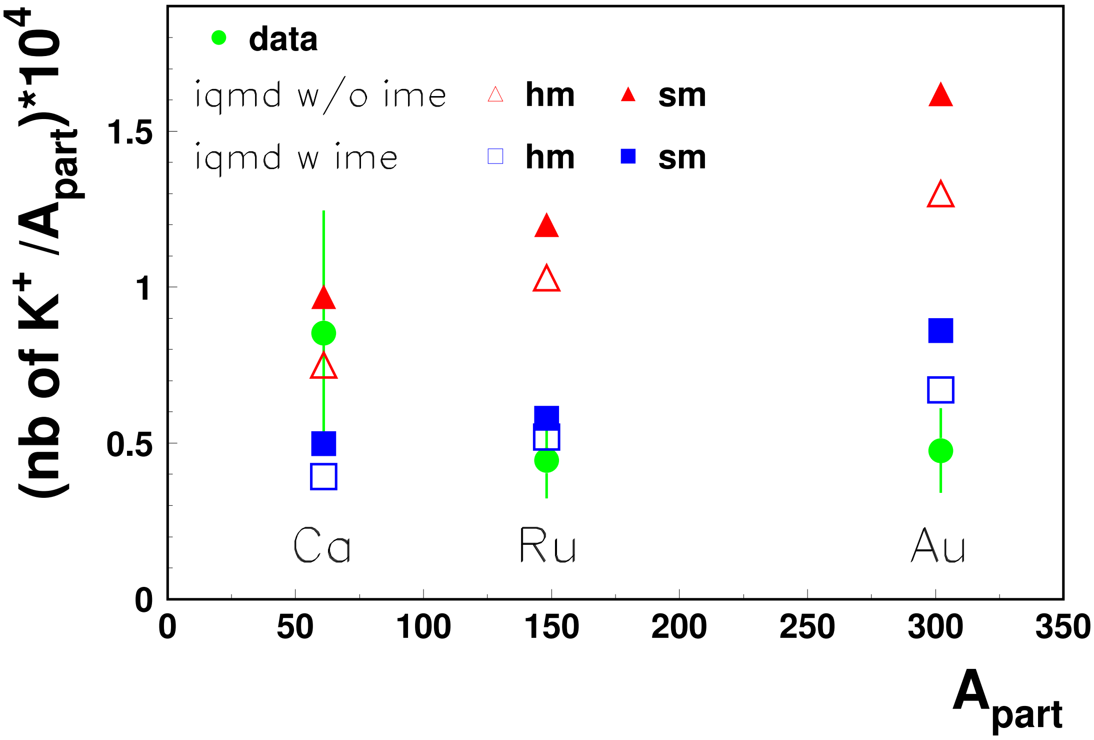

Figure 5.5: *Number of K^+ per participant as a function of the number of participants in Ca+Ca, Ru+Ru and Au+Au at 1.5 AGeV for central collisions. The experimental data, measured in the CDC/BARREL acceptance, are shown by the dots. The predictions of the IQMD model without (with) mass modification are shown by the triangles (squares). The open (full) symbols correspond to the hard (soft) equation of state.*

The KaoS collaboration has recently investigated the dependence of kaon production on beam energy for C+C and Au+Au collisions [Stu 00]. These data favor a soft equation of state which is in disagreement with the conclusion drawn above.

5.4 Predictions for K^-

As mentioned in the introduction, the magnitude of the in-medium K^- mass modification is larger than for K^+. Thus, it should be easier to discriminate experimentally between the two scenarios. The predictions of the RBUU model for the number of K^- per participant as a function of A_{part} for Ca+Ca, Ru+Ru and Au+Au at 1.5 AGeV are presented in Figure 5.6 in the full solid angle (left panel) and in the CDC/BARREL acceptance (right panel) defined as previously by $40° < \theta_{lab} < 130°$, $p_t > 0.1$ GeV/c and $p < 0.4$ GeV/c.

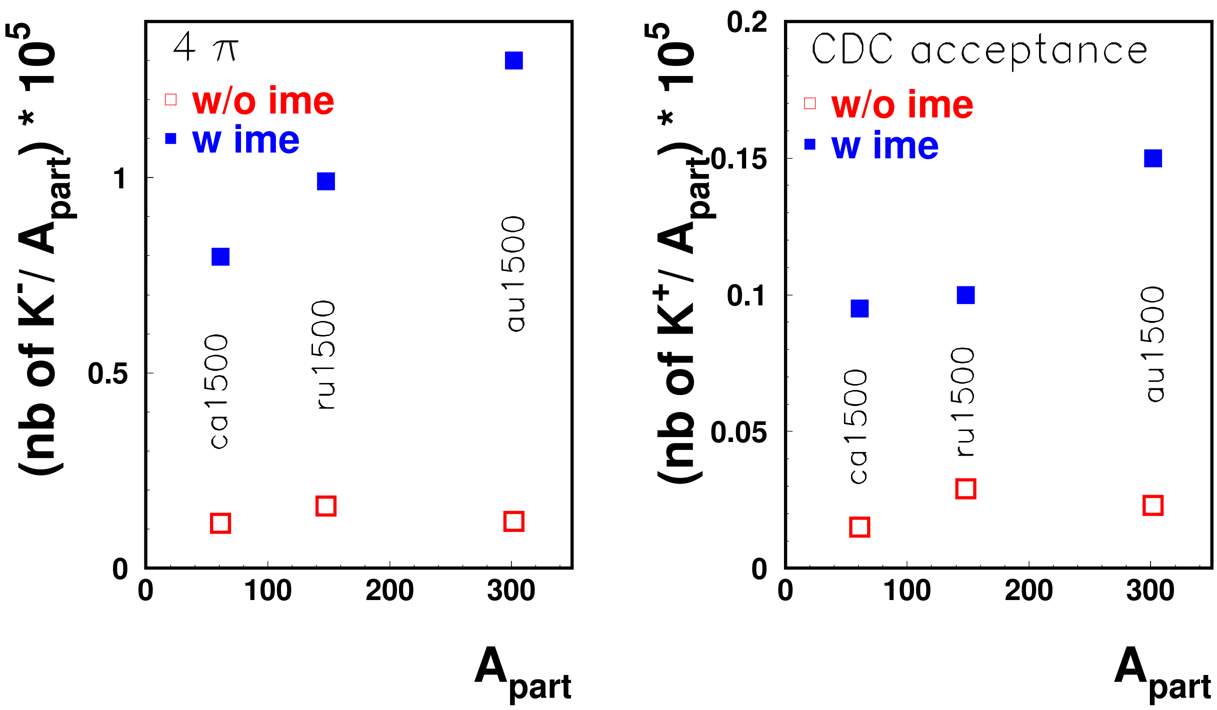

Figure 5.6: *Number of K^- per participant as a function of the number of participants in Ca+Ca, Ru+Ru and Au+Au at 1.5 AGeV for central collisions. The predictions of the RBUU model without (with) mass modification are shown by the open (full) squares.*

Contrary to the case of K^+, the trend for the version including in-medium effects and the version without is completely different. When the in-medium modification of K^- mass is taken into account, the number of K^- per participant increases with the system size whereas the trend is compatible with no dependence on the system size when the K^- mass is not modified in-medium. This feature is still visible when the filter for the CDC/BARREL barrel acceptance is applied. Measuring the production probability of

K^- as a function of the system size appears as an appealing experiment which could shed more light on the puzzling question whether or not the kaon mass is modified in hot and dense matter. However, the measurement of anti-kaons is challenging since their production probability is very low in the considered beam energy range.

5.5 Summary

The comparison of the measured number of K^+ per participant as a function of the system size at 1.5 AGeV to the theoretical predictions seem to favor the version of the calculations including in-medium modifications of hadron properties, both for the RBUU and IQMD models. However, the comparison of the rapidity distributions in Ru+Ru collisions to the predictions of the RBUU model does not allow to draw such a conclusion at this stage of the study. Further investigations are needed, especially for what concerns the Ru system at 1.52 AGeV. As mentioned in the previous chapter, the values obtained for the inverse slope parameter are not fully understood for the moment and may have an influence on the rapidity distributions.

It is clear that a measurement close to mid-rapidity would allow to discriminate more easily between both scenarios, since the in-medium effects are most pronounced in this region. The study of K^- also appears as a very appealing way to answer this question as is shown in section 5.4.

For those reasons the FOPI collaboration is performing an upgrade of its detector. The aim is to increase the acceptance of the central part and reach a better identification of strange particles. In parallel some efforts are made to better understand the performances of the HELITRON to make the combination of data measured in both drift chambers possible.

Chapter 6

PesToF counters

6.1 FOPI upgrade

As already mentioned in the introduction, a strong interest has been shown during the last decade for the measurement of kaons produced in heavy ion collisions in a broad range of energies (from SIS to SPS). Furthermore, the predictions of the RBUU model, presented in the previous chapter, show that the measurement of K^- could answer the question whether or not the kaon mass is modified in a hot and dense medium.

The FOPI phase II detector allowed to measure the kaon production and to investigate their properties in various systems mainly in terms of flow and yields. The interesting results already obtained are nevertheless limited by the acceptance of the detector in its actual configuration and by the performances of its time of flight system. The resolution of the plastic scintillators used in the barrel is around 300 ps which allows the separation of kaons from pions and protons only up to $P_{lab} = 0.5$ GeV/c. The geometrical acceptance covers the angular range between 40° and 130°. The granularity of 180 is far too small for the 50-70 charged particles produced in a Au+Au collisions.

The FOPI detector in its configuration is not able to measure K^- in a proper way in systems like Au+Au at the highest energy available at GSI. For these reasons the FOPI collaboration has decided in 1997 to upgrade the time of flight system. The aim of this upgrade is to:

- have a time resolution below 100 ps to make possible the kaon identification up to $P_{lab} = 1$ GeV/c

- increase the granularity by a factor of 5 to get a double hit probability below 6%
- extend the polar angular coverage to 35° to cover the mid-rapidity region

As the performances of the plastic scintillators seem to be sufficient for the backwards angles, it has been decided to shorten them and to use a new type of counters for the angular range between 35° and 65°.

6.2 History of the PesToF counters

First developed by Yu. Pestov in Novosibirsk in the 70's, the so called PesToF counters have triggered a lot of interest in the world of time of flight measurement [Par 71, Pes 99]. It was proposed as an "ideal" time of flight detector as it is well known that the spark counters with a localized discharge have the best time resolution of known detectors.
Several counters have been built in Russia and were first used in the experiment measuring the pion form-factor near the threshold at the e-p VEPP-2 collider in Novosibirsk (1978-1985). The R&D program was continued in Novosibirsk (1986-1990) in the framework of e^+e^- colliders. Foreseen as an attractive solution for the ALICE time of flight system [Ali 00] a "PesToF" group was started at GSI in the 90's to investigate and further develop this promising detector.
Several prototypes were tested "in situ" in the FOPI experiment (august 97) and in NA49 at CERN in 97-98-99. At the time the decision was made by the ALICE collaboration, many features of the PesToF counters were still not understood and some problems remained. However, this kind of counters appeared as an interesting solution for the upgrade of the FOPI detector since they have a good time resolution (below 100 ps), they can be operated in a magnetic field without problems and they offer a high granularity. A joined FOPI-Pestov R&D program was started based on cosmic and beam tests. The main results of these 2 years of investigation are presented in section 6.4.

6.3 Working principles

A PesToF spark counter, schematically shown in Figure 6.1, is a single gap gaseous parallel plate detector working in the streamer/spark mode. It is composed of a metallic cathode and of a resistive glass anode ($10^9 - 10^{10}\Omega$m). The two electrodes ($300 \times 40 \times 2\ mm^3$) are separated by ball spacers and form a gap of 100 μm. They are embedded in a plastic support structure and placed in an aluminum tube. On top of the anode is the readout board composed of 16 strips which transport the signal to the front end electronics.

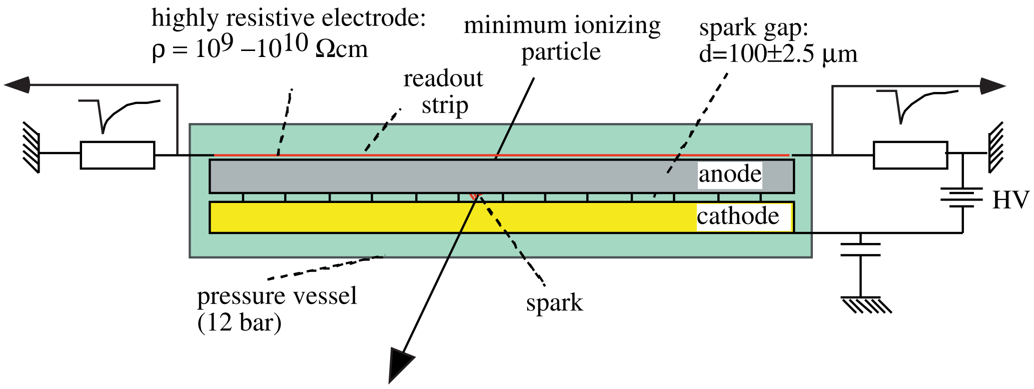

Figure 6.1: *Schematic layout of a PesToF counter.*

A high voltage (around 4.5 kV in the standard configuration) is applied to the electrode and the counter is operated at high pressure (12 bars in the standard configuration) with a gas mixture of the type 0.07(bars)$C_4H_6 + 0.3C_2H_4 + 2.4C_4H_{10} + 9$Ar.
The counter starts working when the voltage is higher than a given threshold which is around 3 kV within these conditions. This voltage corresponds to the electric field needed to reach the critical amount of electrons necessary to develop a spark.
A charged particle crossing the gap ionizes the gas and produces few primary clusters which may start a Townsend avalanche. When the number of electrons in the avalanche reaches a critical value (10^8e^- corresponding to the Rather's condition) the avalanche develops into a new regime called streamer. This last mechanism is very fast. The many electrons and ions produced during the avalanche development form a conducting plasma between the two electrodes which leads to a final spark. At the location of the spark a signal is induced by capacitance on few of the most closely located metallic strips. Each strip builds together with a grounded printed circuit board a 50 Ω transmission line. The sixteen timing signals are readout on both ends of the strips while the sixteen charge signals are readout on one end. After the spark occurs the electric field breaks down and

is only restored when all the ions have been eaten up.

To reduce the dead area on the electrodes and the recovering time, two parameters play an essential role. The thickness of the anode defines the surface of the inactive area after a spark and its resistivity must be high enough to let time to remove the ions from the gap. Furthermore the gas mixture must be rich enough in quenchers to exclude secondary sparks which may occur due to the photons emitted during the avalanche. In the present design of the PesToF counter, the recovering time is around 1 μs and the discharge is localized on 1 mm^2 while the rest of the counter remains sensitive.

Concerning the electronics, a new type of discriminator has been developed. Typical pulses have a rise time of around 200 ps and present some after-pulses. To deal with those different shapes two discriminators working at two different thresholds are used. The time t_0 is extrapolated as shown in the Figure 6.2.

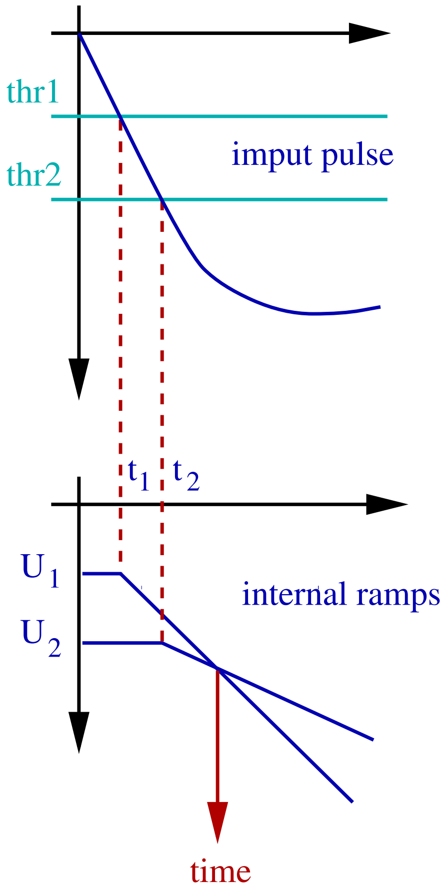

Figure 6.2: *Working principle of a double threshold discriminator.*

A time resolution of around 100 ps has been obtained with the standard design of the detector in various conditions. Despite this good resolution, the PesToF counters develop a tail beyond the expected gaussian-shaped time response, which corresponds to delayed signals. This not understood feature deteriorates the otherwise good performances of the counters. Different assumptions have been made, some models have been developed and many tests have been performed to understand the origin of the tail. One important R&D program has been started at GSI in 97 by the FOPI collaboration together with the Pestov group. A detailed description of the tests and the main results are presented in the following sections.

6.4 Results

Several beam tests were done in cave C and B at GSI to investigate the different parameters which could possibly have an influence on the resolution and on the tail. The general setup is described in the first part. The dependence on noble gas, organic gas component, pressure, energy loss and the efficiency are presented in the following sections.

6.4.1 Setup

Several test experiments have been performed at GSI with the counter described above using a heavy ion beam of ^{12}C or a ^{40}Ar at 1.5 AGeV delivered by the SIS accelerator. After a fragmentation target placed about 20 m upstream from the test setup, the transport line system has been set to select 1.5 GeV protons.

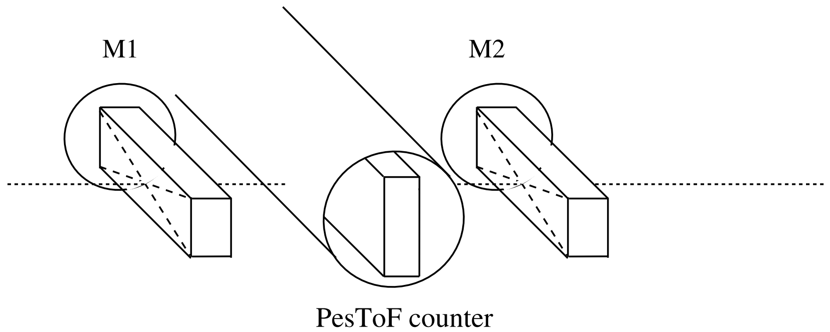

Figure 6.3: *Setup of the experiment: the PesToF counter is placed between two plastic scintillators used as time reference and trigger.*

The setup (Figure 6.3) is composed of a PesToF counter placed between two plastic scintillators referred to as M_1 and M_2. These counters deliver the reference time signal and are used as trigger.
The time difference between M_1 and M_2, $(t_1 - t_2)$ delivers a gaussian spectrum, with a resolution, $\sigma_{(t_1-t_2)}$ of about 50-60 ps and negligible tails. The time of the scintillators used as reference for the determination of the time response function of the spark counter is given by

$$T_S = \frac{1}{2}(t_1 + t_2) \tag{6.1}$$

where t_1 and t_2 are the times measured in the two scintillators. The resolution σ_{T_S} of the reference time T_S is:

$$\sigma_{T_S} = \frac{1}{2}\sigma_{(t_1-t_2)} \tag{6.2}$$

where $\sigma_{(t_1-t_2)}$ is the width of the time spectrum delivered by the two scintillators.
The two scintillators M_1 and M_2 are placed symmetrically, one before and one after the spark counter: in such an arrangement the time reference is independent on the beam particle velocity. The longitudinal direction of the scintillators is oriented parallel to the one of the gas counter and the two photo-multipliers are both mounted on the same left-hand side of the scintillators (with respect to the beam). In such a geometry, $(t_1 + t_2)$ is depending on the position while $(t_1 - t_2)$ is not and in order to take advantage of the intrinsic resolution of 40 ps for T_S, a correction for the light propagation velocity of 16 cm/ns in the scintillators needs to be taken into account. This is obtained using the position information along the strips of the spark counter. The measurement of the scintillation signal amplitude is used to select a pulse height corresponding to minimum ionizing particles in M_1 and M_2 and allows to obtain an improved clean spectrum without tails for the time reference.
The time measured in the spark counter is:

$$T_P = \frac{1}{2}(t_{left} + t_{right}) \tag{6.3}$$

where t_{left} and t_{right} are the times measured on both ends of the strip which has the largest amplitude. The measured time response spectra are given by $t = T_P - T_S$.
The resolution of this measured time in this setup is then:

$$\sigma_t = \sqrt{\sigma_{T_P}^2 + \sigma_{T_S}^2} \tag{6.4}$$

where σ_t is the resolution of the gaussian fitted to the measured spectra and σ_{T_S} is the resolution of the plastic scintillators (about 40 ps).
For a quantitative parameterization of the measured time response function, a gaussian function with an exponential tail is fitted to the data. The centroid t_0 and the resolution σ_t are obtained from the fitted gaussian. The relative amount of tail is defined as:

$$f^{rel}_{tail} = \frac{S_{tot} - S_{gaus}}{S_{tot}} \tag{6.5}$$

where S_{tot} and S_{gaus} are the integral of the whole distribution and the fraction of the fitted gaussian respectively. f^{rel}_{tail} depends rather sensitively on the width of the gaussian. An alternative method is to determine a so called absolute amount of tail f^{abs}_{tail} given by the ratio of the number of events delayed by more than 300 ps with respect to t_0, divided by the total amount of events. For $\sigma << 300$ps, f^{abs}_{tail} does not depend on the width σ.

Figure 6.4 shows a typical time spectrum measured in Argon at 4.6 kV. The line represents the fit described above.

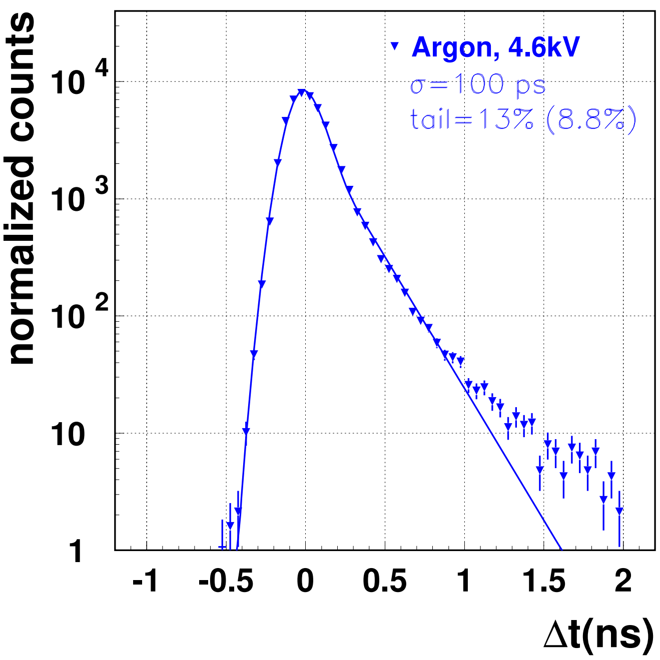

Figure 6.4: *Time spectrum measured in an Argon-based gas mixture. The data are represented by the triangles and the result of the fit by the solid line.*

6.4.2 Voltage

As already mentioned, the counter starts working at a threshold voltage which corresponds to the electric field necessary for the development of a spark. Increasing the voltage from this threshold to the nominal value improves the performances of the counter and allows for a better time resolution.

6.4.3 Noble gases

For a long time Argon was used as the main component of the gas mixture. If one considers that the tail may be the result of a delayed avalanche because the critical number of electrons necessary to get to the streamer mode was not reached in the primary avalanche, using a heavier noble gas should decrease the amount of tail. Indeed the energy loss would be higher and thus the probability that the initial avalanche leads to a final discharge would increase. To verify this assumption, some measurements were done with Krypton and Xenon. Surprisingly the counter behaved worse than with Argon. To get a systematic investigation of the noble gases, Helium and Neon were also tested and the best results both in terms of resolution and tail were obtained with Neon as shown on Figure 6.5 (upper left panel). This feature can be understood within a model based on the growth of the avalanche and presented in section 6.5. This model shows that the important parameters are the drift velocity and the Townsend coefficient of the gas and they are more favorable in the case of Neon. Therefore Argon was replaced by Neon.

6.4.4 Organic component

During the avalanche, some photons are emitted and may extract an electron from the cathode which could produce a secondary avalanche and thus a delayed signal. For this reason the optimization of the quencher content of the gas mixture to absorb the emitted X-rays is mandatory. The standard quenchers have a low absorption efficiency around the work function of aluminum which is the material used for the cathode [Pes 99]. During a process called conditioning where the counter is operated with a strong γ-source a thin polymeric layer is produced on the surface of the cathode which shifts the work function to higher energies corresponding to a more efficient absorption of photons with the standard quenchers.

Figure 6.5 (upper right panel) shows the time response measured with Neon and the standard organic mixture (triangles). Isobutane was then replaced by Ethane (squares) and DME (circles). The amount of quencher has also been investigated but no significant improvement in terms of resolution and amount of tail could be obtained.

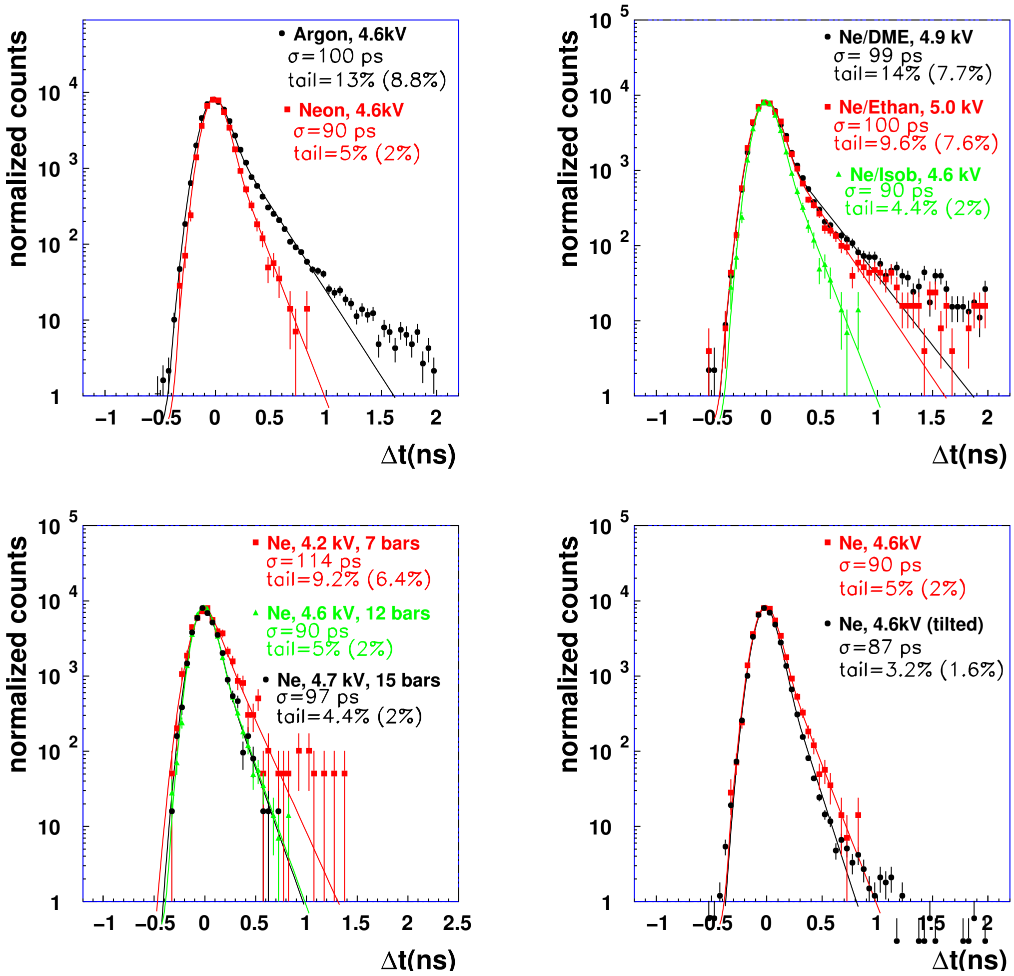

Figure 6.5: *Time spectra measured in Argon (circles) and Neon (squares) at 4.6 kV (upper left panel), time spectra measured in Neon with DME (circles), in Neon with Ethan (squares) and in Neon with Isobutane (triangles) (upper right panel), time spectra measured in Neon at 7 bars (squares), 12 bars (triangles) and 15 bars (circles) (lower left panel), time spectra measured in Neon in the straight configuration (squares) and in the tilted configuration (circles) (lower right panel).*

6.4.5 Dependence on pressure

The pressure of 12 bars is chosen to better localize the discharge in the counter and to provide a reasonable efficiency by increasing the energy loss of the particles and thus the probability to develop a spark. Some measurements were done at 7 bars and 15 bars. As shown in Figure 6.5 (lower left panel), reducing the pressure deteriorates the performances of the counter both in terms of resolution and tail. But increasing it does not really improve the time response.

6.4.6 Dependence on energy loss

Increasing the energy loss should increase the probability of having a primary cluster for a given length and reduce the probability of having a delayed signal.
The dependence of the time resolution and of the fraction of tail on the energy loss can be investigated in different ways.

- For example the fraction of tail can be studied as a function of the time of flight of the particles. If one knows the flight distance, the measurement of the time of flight is equivalent to the measurement of the velocity. The momentum can be deduced if the nature of the particle is known and define the time of flight of a MIP from the Bethe-Bloch formula. We determine with this method that a MIP has a time of flight of 1.7 ns in our experiment and a particle which is twice a MIP has a time of flight of 2.1 ns. It was shown that the fraction of tail decreases when the time of flight increases which is equivalent to an increase of the energy loss.

- Another way to investigate the dependence on energy loss is to compare particle with Z=1 and particle with Z=2. Some measurements were done for Neon at 4.6 kV. Going from Z=1 to Z=2, the resolution goes down from 70 ps to 56 ps and the amount of tail is decreased by a factor of 5. This is a clear evidence that the counter behaves better for high energy loss.

- A last test was performed to evidence this dependence. The usual way of operating the counter is to place the gap perpendicular to the particle trajectory. The particle crosses a 100 μm gap. Tilting the counter around its longitudinal axis increases the apparent size of the gap and then the total energy loss is increased as well. Results for the straight configuration and the tilted one are compared on Figure 6.5 (lower right panel) for Neon at 4.6 kV. Tilting the counter allows to reduce the amount of tail (the decrease of the amount of tail is even larger in Argon). The resolution remains unchanged.

All those measurements lead to the conclusion that the counter behaves much better for a high energy loss.

6.4.7 Efficiency

The last property to be reviewed is the efficiency of the counter. In the case of the FOPI experiment this is a crucial point as one wants to measure ϕ mesons decaying into K^+ K^- with a branching ratio of 50%. The production probability of such particles is in the order of 10^{-5}. A very high efficiency is thus required. The same is true for K^- which are produced at a rate of 1 each 10^4 events.

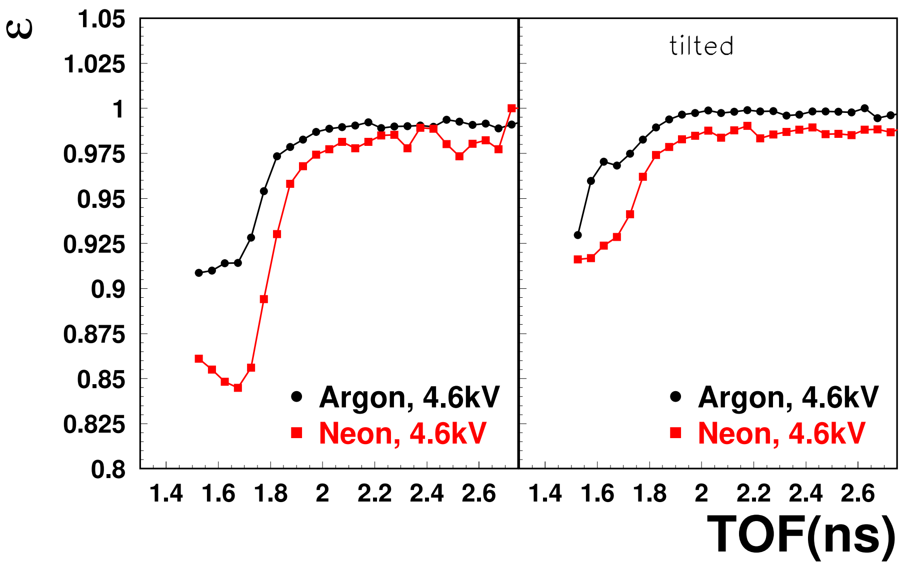

Figure 6.6: *Efficiency as a function of the time of flight for Argon (circles) and Neon (squares) at 4.6 kV in the straight configuration (left panel) and in the tilted configuration (right panel).*

As one would expect the efficiency is higher for Argon than for Neon, Argon being heavier. Figure 6.6 (left panel) shows the efficiency for Argon and Neon at 4.6 kV as a function of the time of flight (ie ionization). For MIP (tof = 1.7 ns) the efficiency is around 90 % for Argon and 85 % for Neon. It increases with the time of flight ie with the energy loss as it should. As explained in the previous section tilting the counter allows for a higher energy loss. As can be seen in Figure 6.6 (right panel), the efficiency for Argon and Neon at 4.6 kV in the tilted configuration is better than in the straight configuration. In the FOPI experiment the particles will cross the PesToF counters at an angle of around 40° which is roughly equivalent to the previously mentioned tilted configuration. The performances of the counter operated with a Neon based gas mixture would then satisfy the FOPI requirements in terms of efficiency.

6.5 Interpretation: fluctuations in the growth of the avalanche

A lot of work has been done by many people to try to understand the working principles of a spark counter. Some features can easily be explained but some others - the tail for instance - are still not understood.
In this section, the main ideas and results of the model developed by A.Mangiarotti and A.Gobbi [Man 00] are summarized.

The process of a spark formation can be subdivided into 4 steps:

- formation and growth of the avalanche
- transition into the streamer mode
- streamer propagation
- final discharge

The assumption of the model is that the main step is the growth of the avalanche and the fluctuation in its length.
One can draw an analogy to a proportional counter which properties have been investigated for many years. In a proportional counter the electric field varies as $\frac{1}{r}$ and the amplification region starts at a given distance L from the anode. The length of the avalanche is then fixed but the number of electrons reached in this avalanche can fluctuate.

One can calculate the probability to have a multiplication m at a fixed distance L. This is given by a Furry law for one primary electron.
In the case of a spark counter the parameter which is fixed is the number of electrons needed to get into the streamer regime. But the length of the avalanche when this happens can fluctuate. The probability to have a length l for a multiplicity M is given by the same law as in the case of a proportional counter. For the details of the calculation see [Man 00].
The probability is expressed as:

$$\rho_{\mathrm{L}}(\mathrm{l}) = \frac{\mathrm{m_t}}{\exp(\alpha \mathrm{l})} \mathrm{e}^{\frac{\mathrm{m_t}}{\exp(\alpha \mathrm{l})}} \tag{6.6}$$

where α is the Townsend coefficient, l is the size of the avalanche and $\mathrm{m_t} = 10^8$.
An absolute scale $\frac{1}{\alpha \mathrm{l}}$ appears in this expression. As the drift velocity is a constant this absolute scale can translate into $\frac{1}{\alpha \mathrm{v_D}}$.
The presence of this absolute scale explains the better results obtained with Neon, this gas having a more favorable $\frac{1}{\alpha \mathrm{v_D}}$ than Argon.
The model predicts the shape of the signal and the presence of the tail. It also describes quantitatively the scaling relation between the resolution, the fraction of tail and the position of the peak $\mathrm{t_0}$ as a function of the applied voltage [Man 00].
As a conclusion one can say that only considering the fluctuation in the length of the avalanche, the model is able to predict the shape and the scaling properties of the time response of the PesToF counter. However it is for the moment impossible to have quantitative agreement because the model suffers of some limitations as:

- the finite gap size is not taken into account
- lateral diffusion and space charge effects are neglected
- nothing is known on the fluctuation in the streamer formation and on its propagation
- the secondary avalanches are not taken into account

6.6 Adaptation to FOPI needs and status of the project

The PesToF barrel is foreseen to cover the polar angular range between 35° and 65°. For many reasons it appeared to be easier to install a 90 cm long detector than 3 short ones.

By doing so the number of electronics channel is diminished and less space is needed for the electronics blocks.

A long prototype was designed with a readout on both sides which is more convenient for the installation of the counters in the FOPI detector. It is basically the same as the short model except for what concerns the anode. It was indeed impossible to build a long anode. Therefore 3 short ones are used instead. The long prototype surprisingly behaved the same as the short one giving the same resolution and the same amount of tail.
The results presented here were obtained during a several experiments aimed at mapping the influence of different parameters on the performances of the counters rather than getting the best results. During the next tests, the parameters and the analysis strategy were optimized to get the best resolution and the minimum amount of tail. The typical resolution is around 60 ps with few percent of relative tail.

However, the construction of the counters is more complicated than foreseen. The main difficulty comes from the production of the anodes which requires a high quality glass, free of any cristalised parts. No company could produce this glass in a large quantity. Furthermore the precision of the gap size between both electrodes has to be around 3 μm to avoid any distortion of the electric field. This precision is obtained by polishing the anode surface, using a delicate technique. Few plates of satisfactory quality have been produced during the last years but the mass production could never be started because of the lack of good quality raw glass.

6.7 Background simulation

After one and a half year of R&D the current status of the PesToF counter performances is around 60 ps time resolution with 6 % tail. A simulation was performed to investigate the consequences of the time of flight resolution on the background for kaon signal.
In Figure 6.7, the black curve shows the momentum distribution of K^+ (right panel) and K^- (left panel) as predicted by a RBUU calculation in a Au+Au reaction at 1.5 AGeV. The other curves show the expected background for different time of flight resolution. The time response of a PesToF counter operated with a Neon-based and Argon-based gas

mixture has been parametrized It is compared to the background expected if the time response has a gaussian shape with different resolutions.

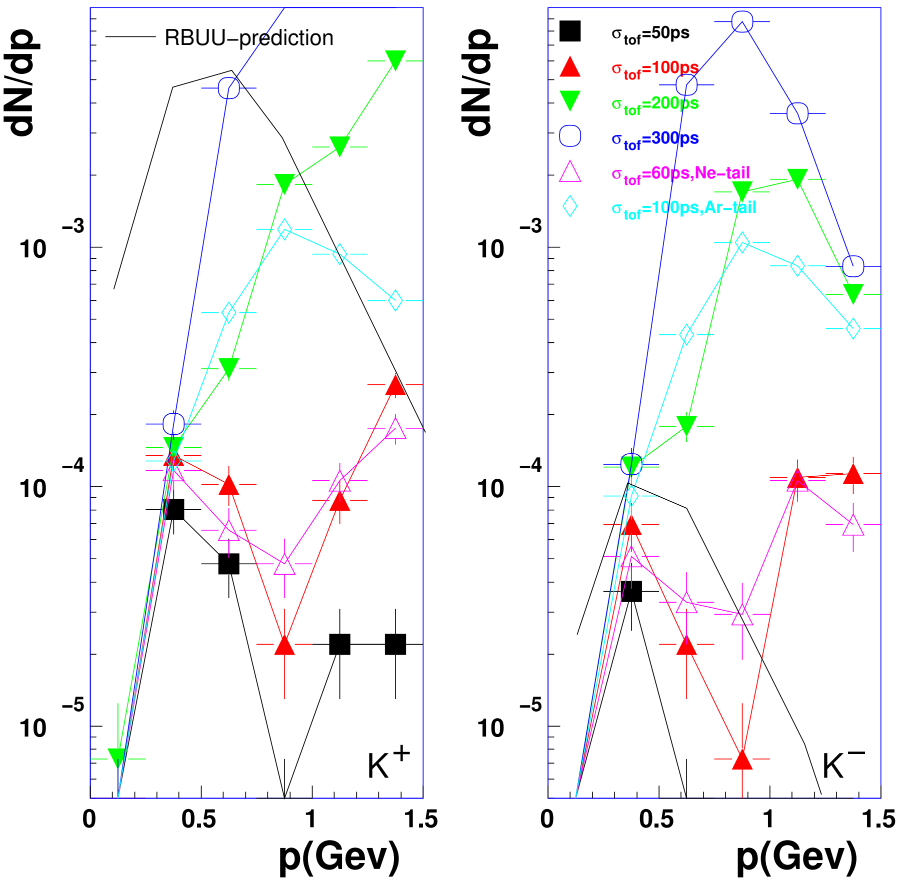

Figure 6.7: *K^+ and K^- production as a function of the momentum. The full line represents the signal as predicted by RBUU calculations. The open triangles (diamonds, resp.) correspond to the background expected for a time of flight with 60 (100, resp.) ps resolution and the proportion of tails measured with the Neon (Argon, resp.) based mixture. The expected background for gaussian time response with 50 (100, 200, 300, resp.) ps resolution is shown by the squares (up triangles, down triangles, open circles, resp.).*

A PesToF barrel operated with a Neon based gas mixture or a barrel of another type of detctors with an equivalent time response, would allow an identification of K^+ up to a momentum of 1.5 GeV/c and of 0.8 GeV/c for K^-. This would considerably improve the performances of the actual barrel which has a resolution of 300 ps. Within those conditions and with the larger angular coverage of the new time of flight system, kaon identification would become possible very close to mid-rapidity.

Chapter 7

Summary

The FOPI detector in its phase II has been used to investigate kaon properties in heavy ion collisions at the SIS facility at GSI (Darmstadt). The aim is to provide experimental data that are sensitive to the question whether hadron masses are modified in hot and dense nuclear matter. This could shed some light on the eventual restoration of chiral symmetry and on the kaon condensation. This last property would explain why neutron star masses do not exceed 1.5 solar masses. In view of the search for the quark-gluon plasma, it is also very important to understand strangeness production in a very broad range of energies since strangeness enhancement is proposed as a signature for the QGP.

Kaons can be identified in the central part of the FOPI detector. Encouraging results on K^+ flow [Cro 00] and on the K^- / K^+ ratio [Wis 00] have been obtained recently by the FOPI collaboration. When compared to theoretical predictions, the data seem to favor the assumption of in-medium modification of hadron masses. However, some uncertainties remain and a complete description of all observables is still missing.

Rapidity distributions of K^+ in Ru+Ru collisions at 1.69 AGeV have been compared to the results obtained in the same system at 1.52 AGeV. The motivation of such a study is to compare the K^+ production below and above the threshold energy for kaon production in a free NN-collision. The K^+ yield does not vary with the energy whereas the apparent temperature deduced from a Boltzmann fit to the transverse mass spectra is lower by 20 MeV at 1.52 AGeV beam energy than at 1.69 AGeV. This is somehow against expectations. The small energy difference should not affect the kinematics in a drastic way. But it is expected that yields should differ since the lowest energy corresponds to a subthreshold K^+ production whereas the highest energy corresponds to a production above threshold. At this point of the investigations, it can not be excluded that some systematic bias changes the trend of the data, although the protons look the same at both energies.

K^+ production has been investigated as a function of the number of participants and as a function of the system size. For that purpose, Ca+Ca, Ru+Ru and Au+Au collisions at 1.5 AGeV have been analysed. Unfortunately, the statistics available for the Ca system is very low. The quality of the measurement does not allow to include this point in the systematics in a reliable way. The K^+ multiplicity normalized to the number of participants is slightly larger in Au+Au collisions than in Ru+Ru collisions at an incident energy of 1.5 AGeV. The KaoS collaboration has measured an increase of kaon production with the system size [Stu 00]. However, the difference found between Ni+Ni collisions and Au+Au collisions is smaller than a factor of two. The slight increase observed by FOPI when going from Ru+Ru collisions to Au+Au collisions does not reproduce the KaoS results in a quantitative way.
An attempt has been made to compare more precisely the results measured by both collaborations. Several assumptions had to be made to overcome the different acceptances of the detectors and the different centrality selections. Within errors, the K^+ multiplicity measured in Au+Au collisions at 1.5 AGeV by the FOPI collaboration and presented in this work are not in contradiction with KaoS measurements.

The experimental data are compared to the predictions of RBUU and IQMD transport models. The calculations are available in two versions, one using the kaon bare mass and one including the modification of the kaon mass in the medium. The experimental data on kaon multiplicity as a function of the system size seems to favor the scenario which includes in-medium effects for both models. From the rapidity distributions, it is difficult to draw any conclusions. Indeed, the difference between the two versions of the calculations is very small in the rapidity region covered by the central part of the FOPI detector. The largest effects are observed at mid-rapidity.

The HELITRON acceptance covers the region of mid-rapidity. It has been shown that the K^+ can be identified in this drift chamber. Ru+Ru collisions at 1.69 AGeV have been used for this study. The goal was to measure complete spectra by combining CDC and HELITRON data and the first attempt looks promising. However, some features could not be understood during the time of this work and require a dedicated investigation.

At this stage of the analysis, it is not possible to draw any final conclusions on whether or not the kaon mass is modified in medium. Different factors limit the quality of the data and the messages conveyed by the measurements. The performances of the FOPI detector allow to identify the K^+ only in a limited part of the phase space. The statistics for Ca+Ca and Au+Au collisions is rather small. This makes a detailed investigation of kaon properties in these two systems out of reach.

It becomes clear that the measurement of kaon meson in a large phase space, especially in the region close to mid-rapidity is mandatory to distinguish the different assumptions underlying theoretical predictions. For that purpose, the FOPI collaboration has initiated an upgrade of its detector three years ago. A faster data acquisition will allow to increase the event rate and thus the statistics. The CDC has been completely rewired to improve its performances, especially its longitudinal position resolution and its operating stability. The HELITRON has also been improved hardware-wise which will hopefully remove the features observed in the old data and allow for an easier combination of HELITRON and CDC data.
The main part of the upgrade consists in the construction of a new time of flight system for the polar angular range between 36° and 65°. The concept developed during the last three years is based on the construction of PesToF spark counters. These counters have a very good intrinsic time resolution which is however diminished by the presence of tails in the time response, corresponding to a delayed signal. Investigations on the gas mixture have revealed that neon is better suited than argon which was used up to now. The results measured with a 90 cm long prototype give a time resolution of 60 ps with a few percent of tail, which would fulfill the FOPI requirements for K^+ and K^- identification. Unfortunately, these counters require the use of special glass plates which could not be produced in large quantity with the required quality. Another solution

is foreseen which consists in building Resistive Plate Counters which already revealed promising performances during the last months.

With the upgraded apparatus, the FOPI collaboration will be able to measure with accuracy kaon and ϕ production in a large phase space. Flow studies and measurement of production cross sections will most probably allow to answer the question whether or not the kaon mass is modified in hot and dense nuclear matter.

Bibliography

[Aic 85] J. Aichelin and C.M. Ko, Phys. Rev. Lett 55(1985) 2661

[Aic 91] J. Aichelin, Phys. Rep. 202 (1991) 233

[Aic 00] J. Aichelin, Private communication

[Ali 00] ALICE technical design report for the ToF system, CERN/LHCC 2000-12 (2000)

[Ant 99] F. Antinori *et al.*, Nucl. Phys. A661 (1999) 130c

[Bar 97] R. Barth *et al.*, Phys. rev. Lett. 78 (1997) 4007

[Ber 88] G.F. Bertsch and S. Das Gupta, Phys. Rep. 160 (1988) 189

[Bes 97] D. Best *et al.*, Nucl. Phys. A625 (1997) 307

[Bra 98] P. Braun-Munzinger and J. Stachel, Nucl. Phys. A638 (1998) 69

[Bra 00] E. Bratkovskaya Nucl.Phys. A675 (2000) 661

[Bro 88] G.E. Brown *et al.*, Phys. rev. D37 (1988) 2042

[Bro 91] G.E. Brown *et al.*, Phys. rev. C43 (1991) 1881

[Bro 94] G.E. Brown and H.A. Bethe, Asto. Jour. 423 (1994) 659

[Bru 78] R. Brun *et al.*, CERN/DD/78 (1978)

[Cas 90] W. Cassing and U. Mosel, Prog. Part. Nucl. Phys. 25 (1990) 235

[Cas 97] W. Cassing *et al.*, Nucl. Phys. A614 (1997) 415

[Cas 99] W. Cassing and E.L. Bratkovskaya, Phys. Rep. 308 (1999)

[Cas 00] W. Cassing, Private communication

[Cro 00] P.Crochet *et al.*, Phys. Lett. 486 (2000) 6

[Fri 98] B. Friman *et al.*, Eur. J. Phys. A3 (1998) 165

[Gle 92] N. Glendenning and F. Weber, Phys. rev. C45 (1992) 844

[Gob 93] A. Gobbi *et al.*, Nucl. Inst. Meth. A324 (1993) 156

[Gut 89] H.H. Gutbrod *et al.*, Rep. Prog. Phys. 52 (1989) 1267

[Har 92] C. Hartnack, Dissertation, University of Frankfurt, Germany (1992)

[Her 96] N. Herrmann, Nucl. Phys. A610 (1996) 49c

[Hei 99] H. Heiselberg and M. Hjorth-Jensen, nucl-th/9902933

[Kap 86] D.B. Kaplan and A.E. Nelson, Phys. Lett. B174 (1986) 57

[Kli 90] S. Klimt *et al.*, Phys. Lett. B249 (1990) 386

[Ko 96] C.M. Ko and G.Q. Li, J. Phys. G22 (1996) 1673

[Ko 97] C.M. Ko, V. Koch and G. Li, Annu. Rev. Nucl. Part. Sci. 47 (1997) 1

[Koc 97] V. Koch, LBNL-39463, UC-413

[Kut 00] R. Kutsche, Dissertation, University of Darmstadt, Germany (2000)

[Li 95] G.Q. Li and C.M. Ko, Nucl. Phys. A594 (1995) 460

[Li 97] G.Q. Li, C.H. Lee and G.E. Brown, Nucl. Phys. A625 (1997) 372

[Lut 92] M. Lutz, S. Klimt and W. Weise, Nucl. Phys. A542 (1992) 52

[Lut 00] M. Lutz, B. Friman and Ch. Appel, Phys. Lett. B474 (2000) 7.

[Man 97] M. Mang, Dissertation, University of Frankfurt, Germany (1997)

[Man 00] A. Mangiarroti and A. Gobbi, to be submitted to NIM

[Mao 99] G. Mao *et al.*, Phys. Rev. C59 (1999) 3381

[Met 93] V. Metag, Prog. Part. Nucl. Phys. 30 (1993) 75

[Ody 98] G.J. Odyniec, Nucl. Phys A638 (1998) 135c

[Par 71] V.V. Parkhonichuck *et al.*, Nucl. Inst. Meth. 93 (1971) 269

[Pei 89] G. Peilert *et al.*, Phys. Rev. C39 (1989) 1402

[Pes 99] Yu. N. Pestov, Proceedings of the V workishop on RPC and related detector, Bary, Italy (1999)

[Ple 99] Ch. Plettner, Dissertation, University of Dresden, Germany (1999)

[Raf 82] J. Rafelski and B. Müller, Phys. Rev. Lett. 48 (1982) 1066

[Raf 91] J. Rafelski, Phys. Lett. B262 (1991) 333

[Rap 00] R. Rapp and J. Wambach, Contribution to the 2nd KEK-Tanashi International Symposium on 'Nuclear and Hadronic Physics with Electromagnetic Probes', Tokyo (1999)

[Rei 97] W. Reisdorf and H.G. Ritter, Ann. Rev. Nucl. Part. Sci. 47 (1997)

[Rit1 95] J.L. Ritman and the FOPI collaboration, Z. Phys. A352 (1995) 355

[Rit2 95] J.L. Ritman *et al.*, Nucl. Phys. Proc. Supp. 44 (1995) 708

[Sch 94] J. Schaffner *et al.*, Phys. Lett. B324 (1994) 268

[Sch 97] J. Schaffner *et al.*, Nucl. Phys. A625 (1997) 325

[Sie 79] P.J. Siemens and J.O. Rasmussen, Phys. Rev. Lett. 42 (1979) 880

[Sto 86] R. Stock, Phys. Rep. 135 (1986) 261

[Stö 86] H. Stöcker and W. Greiner, Phys. Rep. 137 (1986) 277

[Stu 00] Ch. Sturm *et al.*, nucl-ex/0011001

[Waa 96] T. Waas *et al.*, Phys. Lett. B379 (1996) 34

[Wei 96] W. Weise, Nucl. Phys. A610 (1996) 35c

[Wis 00] K. Wiśniewski, PhD. Thesis, University of Warsau, Poland (2000)

Acknowledgments

At this place, I would like to thank those who supported me and helped me in so many different ways during those years.

First I want to thank Prof. Dr. P. Braun-Munzinger for giving me the chance to work in his group at GSI, for his support and for the fruitful discussions.
I also want to thank Prof. Dr. N. Herrmann for sharing his enthusiasm about research with me and for his continuous help and support.
I'm grateful to Philippe, Anton and Christian F. who always answered my questions with patience and humor and who helped me in so many ways.
I also want to thank all the FOPI members, especially Yvonne, Josef, Roland, Klaus, Willy, Piotr and Adriano for their help and also Ralf, Tarek, Olaf, Chechek and Marc.
I am thankful to Ch. Hartnack, J. Aichelin, E. Bratkowvskaya and W. Cassing for providing the theoretical results presented in this work and for the interesting discussions.

Thank you Christian M. for the chocolate-breaks, the opera, the Apfelstrudel and all the rest.... I don't forget the friendship of Joachim, Peter and Christian S.
Sharing an office and more with Ketel was very nice.
Warm thanks to Traudel and Isia who contributed to solve all the technical difficulties and for their moral support.
Severine, Myriam, Franck, Denise and Jean-Marc supported me continuously during my thesis (and before!), sharing my frustrations and the happy moments, although via email most of the time. Thank you, I owe you a lot!
Merci a maman, a Claire et a la famille Gaa. Vous avez toujours ete la pour moi et vous avez cru en moi, meme si vous ne comprennez pas vraiment ce que je fais et a quoi ca sert. Merci pour tout.

Ally (the cat) helped me writing this thesis, spending so much of her time on my laps, purring and playing with the keyboard. Thank you Ally.
Finally I want to thank Dan not only for his wonderful support during the last months but also for opening my eyes on what really matters in life....